INSTITUTE FOR
MICROELECTRONICS

DIPLOMARBEIT

Potential Energy Surface Approximations for Nonradiative Multiphonon Charge Transitions in Oxide Defects

ausgeführt zum Zwecke der Erlangung des akademischen Grades eines Diplom-Ingenieurs unter der Leitung von

Ao.Univ.Prof. Dipl.-Ing. Dr.techn. Tibor Grasser

E360 - Institut für Mikroelektronik

und der Assistenz von

Dipl.-Ing. Dr.techn. Yannick Wimmer

E360 - Institut für Mikroelektronik

eingereicht an der Technischen Universität Wien

Fakultät für Elektrotechnik und Informationstechnik

von

Dominic Waldhör BSc

01226100 / E 066 508

Wien, im Oktober 2018

Die approbierte gedruckte Originalversion dieser Diplomarbeit ist an der TU Wien Bibliothek verfügbar
The approved original version of this thesis is available in print at TU Wien Bibliothek.
TU WIEN Bibliothek Your knowledge hub

Die approbierte gedruckte Originalversion dieser Diplomarbeit ist an der TU Wien Bibliothek verfügbar
The approved original version of this thesis is available in print at TU Wien Bibliothek.
TU WIEN Bibliothek Your knowledge hub

Kurzfassung

Performance und Lebensdauer von MOSFETs werden durch Effekte, wie etwa Telegraph-Rauschen, 1/f-Rauschen oder Bias Temperature Instability (BTI), wesentlich beeinflusst. Diese Effekte werden durch Ladungseinfang durch Defekte in der Oxid-Schicht verursacht. Die Untersuchung von Defekten und ihrem dynamischen Verhalten erlangte daher in den letzten Jahrzehnten große Bedeutung für die Erstellung von Zuverlässigkeitsmodellen in der Mikroelektronik. Eine genaue Beschreibung des Defektverhaltens wird durch das sogenannten 4-State NMP-Modell ermöglicht. In diesem Modell werden zwei stabile und zwei metastabile Defekt-Zustände angenommen, der Ladungstransfer zwischen dem Oxid und dem Substrat des Transistors wird dabei durch eine Nonradiative Multiphonon (NMP) Theorie beschrieben. In diesem Modell werden Defekte für gewöhnlich als eindimensionale quantenmechanische harmonische Oszillatoren behandelt, die korrespondierenden Potentialflächen sind daher Parabeln. Diese Näherung ist allgemein als harmonische Näherung bekannt. Sie ist in der wissenschaftlichen Literatur weit verbreitet, ihre Gültigkeit zur Beschreibung von Oxid-Defekten wurde allerdings bisher nicht genauer untersucht. In dieser Arbeit werden mithilfe der Dichtefunktionaltheorie (DFT) die Übergangszustände und die zugehörigen minimalen Reaktionspfade zwischen Defekt-Zuständen mit unterschiedlichen Ladungen berechnet. Das NMP-Modell wird dann verwendet, um daraus Reaktionsraten für Ladungstransfers zu gewinnen. Die Ergebnisse dieser genauen aber sehr rechenintensiven Methode dienen als Referenz, um die Genauigkeit der harmonischen Näherung zu bestimmen. Dabei ist ein Vergleich auf statistischer Ebene erforderlich, da alle Simulationen in amorphen SiO_2 Strukturen durchgeführt werden. Es wird gezeigt, dass die harmonische Näherung im Allgemeinen gut mit den exakten DFT-Ergebnissen übereinstimmt.

TU WIEN Bibliothek Your knowledge hub
Die approbierte gedruckte Originalversion dieser Diplomarbeit ist an der TU Wien Bibliothek verfügbar
The approved original version of this thesis is available in print at TU Wien Bibliothek.

Die approbierte gedruckte Originalversion dieser Diplomarbeit ist an der TU Wien Bibliothek verfügbar
The approved original version of this thesis is available in print at TU Wien Bibliothek.
TU WIEN Bibliothek Your knowledge hub

Abstract

Detrimental effects on the performance and lifespan of metal-oxide-semiconductor field effect transistors like random telegraph noise, 1/f noise and bias temperature instability are suspected to be caused by charge trapping processes at point defects in the oxide layer. The study of oxide defects and their dynamical behavior in particular became a major topic in device reliability over the last decades. The behavior of oxide defects can be described accurately by the so called four-state NMP model. This model assumes two stable and two metastable defect states, and describes charge transfers between defects and the device substrate with a nonradiative multiphonon (NMP) theory. Within this model, defects are usually treated as one-dimensional quantum mechanical harmonic oscillators, the corresponding potential energy surfaces are therefore assumed to be parabolas. This approximation is commonly known as the harmonic approximation. Although widely used in the scientific literature, the validity of this approximation in the case of oxide defects has not been investigated in greater detail up to now. This thesis uses density functional theory (DFT) to calculate transition states and minimum energy paths between differently charged defect configurations. NMP theory is then used to extract charge transition rates from the obtained data sets. The results of this accurate, but computationally demanding approach are used as reference to evaluate the accuracy of the harmonic approximation. Since all simulations are carried out in amorphous SiO_2 structures, a statistical comparison of the results is necessary. It will be shown, that in general the harmonic approximation is in good agreement with the accurate DFT results.

Die approbierte gedruckte Originalversion dieser Diplomarbeit ist an der TU Wien Bibliothek verfügbar
The approved original version of this thesis is available in print at TU Wien Bibliothek.
TU WIEN Bibliothek Your knowledge hub

Die approbierte gedruckte Originalversion dieser Diplomarbeit ist an der TU Wien Bibliothek verfügbar
The approved original version of this thesis is available in print at TU Wien Bibliothek.
TU WIEN Bibliothek Your knowledge hub

Acknowledgements

At this point I would like to express my deep gratitude to all those who supported me throughout my studies and made this work possible.

First of all, I want to thank my supervisor Prof. Tibor Grasser for the opportunity to work and do research at the Institute for Microelectronics under his guidance. I truly admire his passion, knowledge and commitment towards science and education. He never gave up on me and always believed in my abilities, even at times when I did not believe in myself. For that I am deeply grateful.

I would like to give special thanks to Yannick Wimmer, who worked with me on the topic of this thesis the entire time and with whom I had countless invaluable discussions. I also thank him for proofreading my thesis and helping me to remove all those embarrassing mistakes. Without him, this work would not have been possible in its present form.

Next I also want to thank Markus Jech, Tassem El-Sayed and Theresia Knobloch for providing essential remarks and ideas on parts of this thesis. Furthermore I thank Gerhard Rzepa who provided me with an excellent LaTeX template.

The team behind the Vienna Science Cluster deserves credit for maintaining the high performance clusters on which the results in my thesis were obtained. Without their supply of seemingly limitless computational power, this work would probably need several decades to be completed.

Furthermore I want to thank Prof. Georg Reider, who will be a member of the examining committee. Although I have not chosen his fields of research, I am very thankful for his deep insights, which significantly shaped my understanding of physics.

I express my deepest gratitude to my family. Without the mental and financial support of my parents and grandparents throughout the years, I would have never been able to get this far. Finally I want to thank my beloved girlfriend Nastya for her incredible patience and her support over the last couple of months while I was writing my thesis.

Die approbierte gedruckte Originalversion dieser Diplomarbeit ist an der TU Wien Bibliothek verfügbar
The approved original version of this thesis is available in print at TU Wien Bibliothek.
TU WIEN Bibliothek Your knowledge hub

Die approbierte gedruckte Originalversion dieser Diplomarbeit ist an der TU Wien Bibliothek verfügbar
The approved original version of this thesis is available in print at TU Wien Bibliothek.
TU WIEN Bibliothek Your knowledge hub

Contents

Acknowledgements v

1 Introduction 1
- 1.1 Motivation . . . 1
- 1.2 Scope of This Work . . . 1
- 1.3 Structure of This Work . . . 2

2 Bias Temperature Instability 3
- 2.1 BTI Effects . . . 3
- 2.2 BTI Characterisation . . . 5
  - 2.2.1 Measurement-Stress-Measurement (MSM) . . . 5
  - 2.2.2 RTN Measurement . . . 6
  - 2.2.3 Time Dependent Defect Spectroscopy (TDDS) . . . 6
  - 2.2.4 Capture/Emission Time (CET)-Map . . . 7
- 2.3 Cornerstones of a Reliable BTI Model . . . 8

3 Four-State NMP Model 9
- 3.1 State Diagram . . . 9
- 3.2 Master Equations and Occupancy . . . 10
- 3.3 Capture and Emission Times . . . 11
  - 3.3.1 Two-State System . . . 11
  - 3.3.2 First Passage Time . . . 12
  - 3.3.3 Three-State System . . . 13
- 3.4 Energy Barriers . . . 15
- 3.5 Suspected BTI Causing Defects in SiO_2 . . . 16
  - 3.5.1 Oxygen Vacancy . . . 16
  - 3.5.2 Hydrogen Bridge . . . 16
  - 3.5.3 Hydroxyl-E' Center . . . 16

4 Density Functional Theory 19
- 4.1 Born-Oppenheimer Approximation . . . 19
- 4.2 Hohenberg-Kohn Theorems . . . 22

Die approbierte gedruckte Originalversion dieser Diplomarbeit ist an der TU Wien Bibliothek verfügbar
The approved original version of this thesis is available in print at TU Wien Bibliothek.
TU WIEN Bibliothek Your knowledge hub

4.3 Kohn-Sham Equations . . . 23
4.4 Exchange-Correlation Functionals . . . 24
4.4.1 Local Density Approximation . . . 24
4.4.2 Generalized Gradient Approximation . . . 25
4.4.3 Hybrid Functionals . . . 25
4.5 Basis Sets . . . 26
4.5.1 Plane Wave Basis Sets . . . 26
4.5.2 Gaussian Basis Sets . . . 27
4.6 CP2K Software Package . . . 28
4.6.1 Gaussian Plane Waves Method . . . 28
4.6.2 Auxiliary Density Matrix Method . . . 29
4.7 Simulation Settings . . . 30
4.7.1 Single-Point Calculations . . . 30
4.7.2 Geometry Optimization . . . 31
4.7.3 Amorphous SiO_2 Structures . . . 31

5 From Energies to Rates **33**
5.1 Thermal Transitions . . . 33
5.1.1 One-Dimensional Transition State Theory . . . 34
5.1.2 General Harmonic Transition State Theory . . . 35
5.2 Transition State Optimization . . . 36
5.2.1 Plain Elastic Band . . . 36
5.2.2 Nudged Elastic Band . . . 37
5.2.3 Climbing Image NEB . . . 37
5.3 Nonradiative Multiphonon Transitions . . . 39
5.3.1 Single State Transitions . . . 39
5.3.2 NMP Transitions in a Canonical Ensemble . . . 41
5.3.3 Classical Lineshape Function . . . 42
5.4 NMP Transitions in Oxide Defects . . . 42
5.4.1 Charge Exchange with the Substrate Reservoir . . . 44
5.4.2 Band Edge Approximation . . . 46
5.4.3 Interaction with the Oxide Field . . . 48
5.4.4 Electron-Phonon Coupling Regimes . . . 49
5.5 Energy Alignment . . . 50

6 PES Approximations **53**
6.1 Simple Approximation Schemes . . . 53
6.1.1 Harmonic Approximation (HA) . . . 54
6.1.2 Direct Path Sampling (DP) . . . 54
6.2 Minimum Energy Path . . . 55
6.2.1 MECP Optimization Problem . . . 56
6.2.2 MECP Search Implementation . . . 57

Die approbierte gedruckte Originalversion dieser Diplomarbeit ist an der TU Wien Bibliothek verfügbar
The approved original version of this thesis is available in print at TU Wien Bibliothek.
TU WIEN Bibliothek Your knowledge hub

7 Results **61**
7.1 Representative Case Study 61
7.2 Statistical Evaluation in Amorphous SiO_2 65
7.2.1 Transition Time Accuracy 65
7.2.2 Slope Accuracy 67
7.2.3 Activation Energies 67
7.2.4 Geometric Considerations 72
7.3 Conclusions 72

8 Summary and Outlook **75**

Bibliography **77**

Die approbierte gedruckte Originalversion dieser Diplomarbeit ist an der TU Wien Bibliothek verfügbar
The approved original version of this thesis is available in print at TU Wien Bibliothek.
TU WIEN Bibliothek Your knowledge hub

Die approbierte gedruckte Originalversion dieser Diplomarbeit ist an der TU Wien Bibliothek verfügbar
The approved original version of this thesis is available in print at TU Wien Bibliothek.
TU WIEN Bibliothek Your knowledge hub

CHAPTER 1 Introduction

1.1 Motivation

Since the early days of microelectronics, reliability issues have been subject to intensive study due to the limitations they impose on device performance and lifetime. Metal-oxide-semiconductor field effect transistors (MOSFETs) in particular are mostly affected by $1/f$ noise [1], random telegraph noise (RTN) [2], hot carrier degradation (HCD) [3] and bias temperature instability (BTI) [4]. It is widely accepted that all these detrimental effects are linked to charge trapping events at point defects either at the interface or in the oxide layer of the device. The need for continously higher computational power drives technologies towards higher device densities and therefore smaller structures. From a reliability point of view, this indicates that even single point defects have a large impact on the device performance [5]. Although significant progress was made using ab-initio simulations in recent years [6, 7, 8, 9], the microscopic nature of the effects listed above, is not fully understood yet and needs further research. Knowledge of the behaviour of oxide defects on an atomic level, especially the trapping and detrapping of electric charges, is essential for improving the predictive capabilities of existing reliability models.

1.2 Scope of This Work

BTI refers to a shift of the threshold gate voltage under stress conditions and is one of the most pronounced reliability issues impacting modern MOSFET technologies. Recently BTI and RTN were found to presumably have the same underlying cause [10] and therefore can be described in an unified framework, the four-state nonradiative multiphon (NMP) model [11]. Within this model, oxide defects are assumed to have two positively charged and two neutral states. Using the common Born-Oppenheimer approximation (BOA), the defect dynamics are interpreted as movements on potential energy surfaces (PES) in a high-dimensional configuration space. In this picture, defect states are given by local minima of the PES. Charge transfer between the device substrate and the oxide defect is treated as a transition from one energy surface to another. In the classical limit of quantum mechanical NMP theory, charge capture and emission events occur at the

Die approbierte gedruckte Originalversion dieser Diplomarbeit ist an der TU Wien Bibliothek verfügbar
The approved original version of this thesis is available in print at TU Wien Bibliothek.
TU WIEN Bibliothek Your knowledge hub

minimum energy crossing point (MECP) of the two PES. Usually, the problem of finding the MECP in the high-dimensional configuration space is avoided, by treating the defect states as one-dimensional harmonic oscillators. The MECP is then assumed to be the intersection point of the resulting parabolic energy profiles. This approach is commonly referred to as harmonic approximation (HA). Although the HA is very convenient and is widely used [12, 13, 14], its applicability to oxide defects has not been rigorously investigated so far. In this work an efficient optimization algorithm coupled with density functional theory (DFT) is used to locate the MECP within the configuration space. With this crossing point one can then calculate minimal energy paths between different PESs, which allows to make more accurate estimations for charge capture and emission rates for certain defect types. In particular the oxygen vacancy [15, 16, 17], the hydrogen bridge [18, 19] and the hydroxyl-E′ center [20, 21, 22] are investigated in amorphous SiO_2 structures. With this method, it is possible to analyze the accuracy of the harmonic approximation. Furthermore, it is also applicable to other defect types, which might be investigated in the future to get a better understanding of BTI and HCD.

1.3 Structure of This Work

Chapter 2 starts with a phenomenological description of BTI degradation and discusses measurement techniques to characterise this effect. This is followed by an introduction to Markov chains and the 4-state NMP model as well as the studied defects in Chapter 3. The foundations of density functional theory, the basis for all ab-initio calculations in this work, will be outlined in Chapter 4. In Chapter 5 transition state theory (TST) and NMP theory are discussed to link rates of the four-state model to energy barriers obtained by DFT calculations. The implemented MECP search algorithm as well as the commonly used PES approximation schemes like the HA are described in Chapter 6. Finally, in Chapter 7 a statistical evaluation of the HA accuracy with respect to the MECP approach is presented.

Die approbierte gedruckte Originalversion dieser Diplomarbeit ist an der TU Wien Bibliothek verfügbar
The approved original version of this thesis is available in print at TU Wien Bibliothek.
TU WIEN Bibliothek Your knowledge hub

CHAPTER 2

Bias Temperature Instability

Die approbierte gedruckte Originalversion dieser Diplomarbeit ist an der TU Wien Bibliothek verfügbar
The approved original version of this thesis is available in print at TU Wien Bibliothek.
TU WIEN Bibliothek Your knowledge hub

BTI in essence refers to a shift of the threshold voltage, denoted as ΔV_{th}, due to induced stress on the device by applying high gate voltages at elevated temperatures. Over time this shift can lead to a violation of device specifications and eventually to failure of the electronic circuit. This phenomenon was first described in 1966 [23] but was not considered to be of concern in the early days of microelectronics. In the last decades the progressive downscaling of devices has lead to higher electric fields in oxide layer, now reaching values of several MV/cm [24]. Furthermore, SiON dielectrics are increasingly used to reduce leakage currents in the device [25]. Due to these developments, BTI nowadays has become a major reliability issue [4].

2.1 BTI Effects

Microscopically, BTI is caused by charge traps in the SiO_2 oxide layer or at the Si/SiO_2 interface. During stress, i.e. when applying a high gate voltage (V_{G}) at elevated temperatures, charges can be trapped in the oxide layer and therefore alter the electrostatics of the device, resulting in a shift ΔV_{th} of the threshold voltage [26]. BTI occurs in pMOS as well as nMOS devices. When occuring at negative V_{G} it is termed negative BTI (NBTI), conversely positive BTI (PBTI) describes the degradation mechanism at positve gate voltages. Since pMOS devices are commonly operating at negative V_{G}, they are mostly affected by NBTI. Usually the effect of NBTI is much more pronounced compared to PBTI, however, the introduction of high-k dielectrics [27] also led to considerable PBTI in nMOS devices [4]. It was demonstrated [28, 29], that BTI degradation due to stress is to some extend reversable. Typical measurements of $\Delta V_{\mathrm{th}}(t)$ are presented in Fig. 2.1. As can be seen, the degradation is worst directly after stress and then decreases because some traps emit their charge over time. This reversable part of BTI is referred to as the recoverable (R) component. The permanent (P) component remains as a constant offset to pre-stress values. Recently a recovery of the P component at high temperatures was reported [30, 31], indicating that R and P might be the same effect but on different time-scales. The R component is assumed to be caused by fast oxide traps, whereas

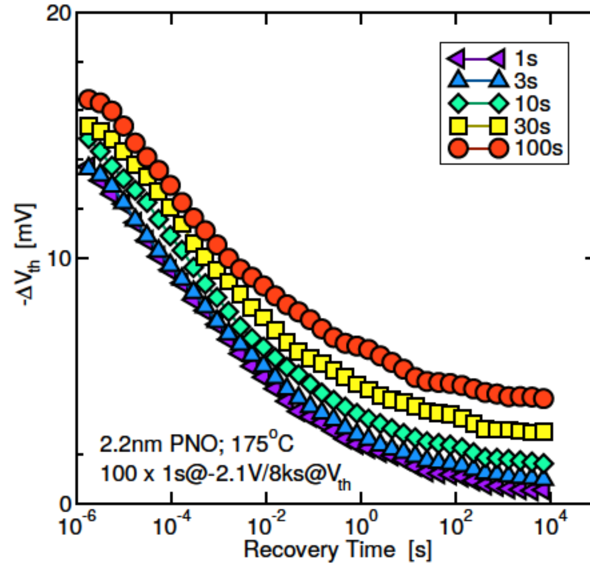

Figure 2.1: NBTI recovery curves for stress times ranging from t_s = 1s to 100s for a large-area 2.2nm pMOS device. After stress ,the degradation is partly reversed over time (R-component). The permanent component (P) remains as a constant offset relative to pre-stress values ($\Delta V_{\mathrm{th}} = 0.0\mathrm{mV}$) and increases with larger stress times. [32]

the P component is associated with slow oxide traps as well as traps at the interface [32].

Smooth degradation curves, as shown in Fig. 2.1, are caused by an ensemble of charge traps in large-area devices. In such devices, the impact of an individual trap on ΔV_{th} is typically not resolvable. In small-area devices, however, single traps have a significant influence. In those devices, as demonstrated in [10], traps responsible for the R-component of BTI produce discrete steps in the $\Delta V_{\mathrm{th}}(t)$ signal, known as random telegraph noise (RTN) [1]. Two typical RTN signals are depicted in Fig. 2.2. In the left figure, a single trap switches continously between the charged and uncharged state. This clearly demonstrates the stochastic nature of charge capture and emission events. Charge capture and emission occur with characteristic time constants τ_{c} and τ_{e} respectively. Note that the depicted RTN signal is only observed when $\tau_{\mathrm{c}} \approx \tau_{\mathrm{e}}$. In Fig. 2.2 (right) a fundamentally different type of charge trap is shown, which produces a temporary RTN signal. Here, the trap switches between two states for some time after stress but eventually stops. This indicates the existence of additional trap states with much larger emission time constants [11].

From averaging over repeated measurements, the values for τ_{c} and τ_{e} can be obtained. As depicted in Fig. 2.3, the time constants τ_{c} and τ_{e} depend strongly on the temperature, suggesting a thermally activated charge transfer, which will be discussed in Ch. 5. Furthermore this figure reveals an exponential dependence on the applied bias voltage V_{G}, resulting in a range of several orders of magnitude for possible capture and emis-

Die approbierte gedruckte Originalversion dieser Diplomarbeit ist an der TU Wien Bibliothek verfügbar
The approved original version of this thesis is available in print at TU Wien Bibliothek.
TU Bibliothek WIEN Your knowledge hub

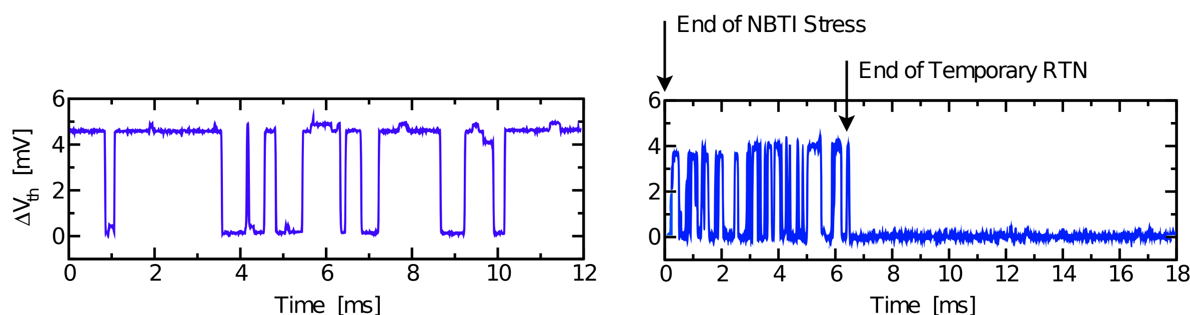

Figure 2.2: Different RTN signals measured on a small-area 2.2nm pMOS. **Left:** A two-state trap produces a continous RTN signal with characteristic capture and emission times. **Right:** After BTI stress, a temporary RTN signal can be observed frequently. In this case, the RTN disappears after some time and is assumed to be caused by a three-state trap. [11]

sion times. Fig. 2.3 (left) also demonstrates the existence of traps with a nearly bias independent emission time constant τ_e, which can only be explained by a model with one additional metastable defect state [11]. In recent years this led to the development of the widely successful nonradiative multiphonon (NMP) 4-state model, which will be described in Ch. 3.

2.2 BTI Characterisation

An in-depth understanding of BTI relies on experimental methods to verify the results of atomistic trap models. Several measurement techniques have been developed over the years, the most commonly used methods will be described briefly in the following.

2.2.1 Measurement-Stress-Measurement (MSM)

This commonly used technique characterises BTI by applying repeated stress/recovery cycles on the test device. At first, the transfer function $I_D(V_G)$ of the device is recorded in order to obtain the initial threshold voltage $V_{th,0}$. Within one measurement cycle a high stress voltage V_G^H is applied at the gate for a certain stress time t_s. Afterwards a lower voltage V_G^L is applied and the temporal progress of the drain current $I_D(t)$ is recorded. Using the previously measured transfer function, variations in I_D are mapped back to variations in the threshold voltage ΔV_{th} [35]. Alternatively, after the stress phase a constant drain current is enforced into the device, providing a direct measurement of ΔV_{th} [36].

Due to a necessary delay time t_d between stress and recovery phase, fast recovery processes are missed when using MSM. To overcome this issue, schemes were developed to measure the device degradation directly in the stress regime, these are commonly known as on-the-fly (OTF) measurements [37, 38].

Die approbierte gedruckte Originalversion dieser Diplomarbeit ist an der TU Wien Bibliothek verfügbar
The approved original version of this thesis is available in print at TU Wien Bibliothek.
TU WIEN Bibliothek Your knowledge hub

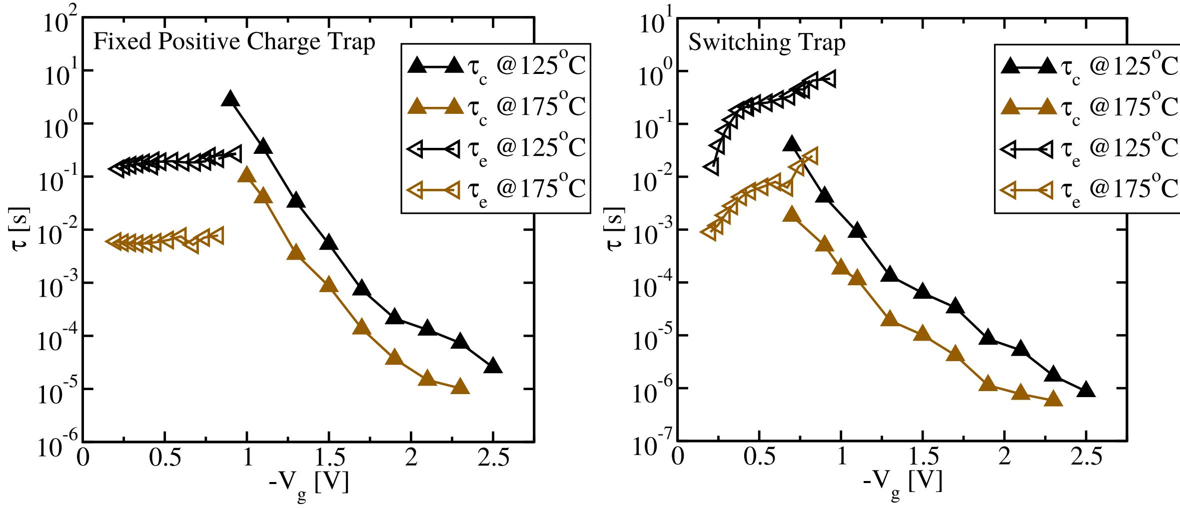

Figure 2.3: Experimental τ_c and τ_e values of two different defects for the temperatures T = 125°C and T = 175°C. The time constants spread over several orders of magnitude during the measurement. [33, 34]

2.2.2 RTN Measurement

Analyzing RTN signals similar to Fig. 2.2 can be used to measure the characteristics of single defects in small-area devices. For RTN measurements the device is operating at a constant bias V_G while $\Delta V_{th}(t)$ is recorded over a long periode of time [39]. After filtering, the Baum-Welch algorithm [40] can be used to fit a hidden-markov-model to the signal [41]. This technique is not restricted to a simple 2 state defect but can also be applied to characterize multi-state defects with considerably complexer dynamic behavior.

2.2.3 Time Dependent Defect Spectroscopy (TDDS)

Similar to RTN measurements, time dependent defect spectroscopy (TDDS) [42] is a method to experimentally extract parameters from single defects. Since RTN measurements apply a constant V_G, the defects are in a quasi-thermal equilibrium which limits the measurable range of time constants to $\tau_c \approx \tau_e$. In contrary, TDDS forces the device to switch between two phases continuously. Analog to MSM, during the stress phase a high voltage is applied to the MOSFET gate, forcing the device into the strong inversion regime and thus shifting the defect equilibrium to the charged state. In the following recovery phase in weak inversion, defects discharge with a characteristic time τ_e resulting in a shift ΔV_{th}. This shift depends on the position of the defect inside the oxide [43], therefore the step height can be used to distinguish different defects. This experiment is repeated many times and the measured step heights together with the corresponding emission times are collected in a so called spectral map (see Fig. 2.4). The capture times τ_c can be extracted by varying the stress time t_s. If $t_s \ll \tau_c$ the defect has not enough time to be charged during the stress phase, thus the corresponding cluster in the spec-

Die approbierte gedruckte Originalversion dieser Diplomarbeit ist an der TU Wien Bibliothek verfügbar
The approved original version of this thesis is available in print at TU Wien Bibliothek.
TU Bibliothek WIEN Your knowledge hub

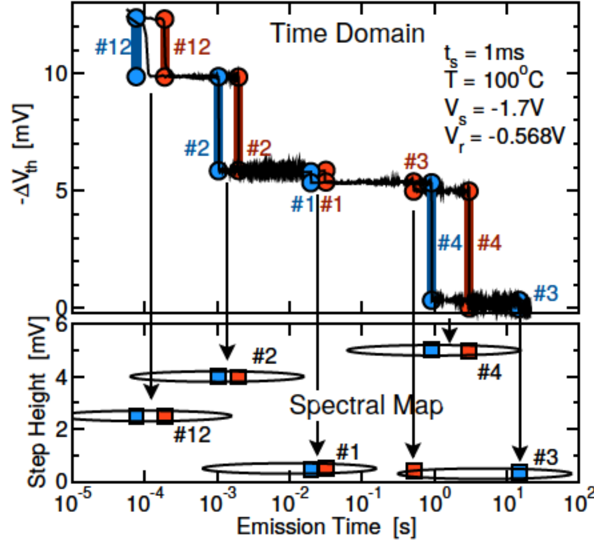

Figure 2.4: Typical results of TDDS measurements. Several emission traces are recorded **(top)** and the resulting step heights and emission times are drawn in a spectral map **(bottom)**, leading to distinct clusters for each defect. [42]

tral map only appears for sufficiently large stress times. TDDS allows to characterize defect dynamics over a much larger time scale than RTN measurements. Furthermore the resulting spectral maps can characterize several defects at once, whereas analyzing RTN signals becomes increasingly difficult with multiple defects involved.

2.2.4 Capture/Emission Time (CET)-Map

RTN and TDDS measurements are designed to characterize only a few defects at once in small devices. Larger MOSFETs naturally contain considerably more defects due to their larger oxide volume. In such devices the impact of a single defect is not resolvable, instead the effects of a whole defect ensemble on the device degradation are observed. Repeating multiple MSM cycles with different stress times t_s and recovery times t_r provides the shift of the threshold voltage as a function $\Delta V_{th}(t_s, t_r)$. Assuming that during the stress phase only defects with $\tau_c < t_s$ are charged and during the recovery all defects with $\tau_e > t_r$ remain charged, ΔV_{th} can be expressed as [11, 44]

$$\Delta V_{th}(t_s, t_r) = \int_0^{t_s} \int_{t_r}^{\infty} g(\tau_c, \tau_e)\, d\tau_e d\tau_c \qquad (2.1)$$

with the CET-map $g(\tau_c, \tau_e)$ (see Fig. 2.5). This map shows the statistical distribution of τ_c and τ_e for the traps of a single device and can be extracted from experimental data by

$$g(\tau_c, \tau_e) = -\frac{\partial^2 \Delta V_{th}(\tau_c, \tau_e)}{\partial \tau_c \partial \tau_e}\,. \qquad (2.2)$$

Die approbierte gedruckte Originalversion dieser Diplomarbeit ist an der TU Wien Bibliothek verfügbar
The approved original version of this thesis is available in print at TU Wien Bibliothek.
TU Bibliothek WIEN Your knowledge hub

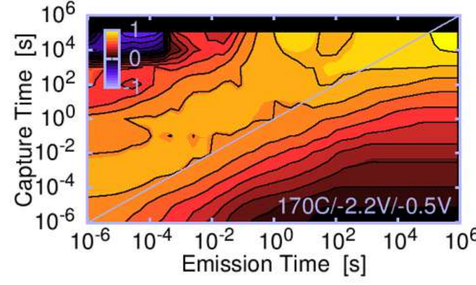

Figure 2.5: CET-map within experimentally accessable time scales. As indicated in this map, the capture and emission times are only loosely correlated to each other. [44]

2.3 Cornerstones of a Reliable BTI Model

The modelling of BTI is increasingly important for the industry to predict the device lifespan as accurately as possible. A good BTI model should therefore be able to explain the following experimental findings [4]:

i) As shown in Fig. 2.3, τ_c is exponentially dependent on the applied gate voltage. Empirically this can be modelled by

$$\tau_c = \tau_0 \exp\left(-c_1 F_{ox} + c_2 F_{ox}^2\right) \tag{2.3}$$

where F_{ox} denotes the electric field in the oxide, whereas c_1, c_2 and τ_0 are fitting parameters.

ii) Traps can have either a field dependent (switching traps) or a nearly field independent (fixed traps) τ_e. In the case of switching traps, τ_e can be modelled similarly to Eq. 2.3.

iii) Both capture and emission events are temperature activated with measured activation energies $E_{A,c} \approx 0.6\text{eV}$ and $E_{A,e} = 0.6 - 1.4\text{eV}$.

iv) τ_c and τ_e are only weakly correlated (see Fig. 2.5).

In order to reproduce the properties ii) and iv), a model with several stable and metastable trap states is required. The following chapter will discuss the four-state model, which can be fitted to explain the key experimental findings accurately [34].

Die approbierte gedruckte Originalversion dieser Diplomarbeit ist an der TU Wien Bibliothek verfügbar
The approved original version of this thesis is available in print at TU Wien Bibliothek.
TU Bibliothek WIEN Your knowledge hub

CHAPTER 3 Four-State NMP Model

Since its discovery in 1966, many different models for BTI have been proposed. The earliest models were all based on variations of a classical reaction-diffusion (RD) model [45, 46]. This approach was widely used in reseach and industry, until it became evident over the last decade, that this model is not able to account for the experimental findings [4]. Furthermore, new measurement techniques like TDDS revealed an underlying charge trapping mechanism in the oxide as the source of BTI. First attempts to explain BTI through charged traps relied on the idea of elastic tunneling of holes between the channel and the oxide [47, 48, 49, 50]. These models fell short to account for the experimentally confirmed exponential temperature dependence of τ_c and τ_e. To overcome this discrepancy, a mechanicsm based on the well known Shockley-Read-Hall (SRH) recombination [51, 52] with an extension to factor in the tunneling between oxide and channel [53], as well as the thermal activation [43] was proposed. Although this model was not able to explain the experimental findings all at once, it played an important role as an originator for a recently suggested model, the four-state nonradiative multiphonon (NMP) model [54, 11], which is capable of capturing the most important features of BTI. Contrary to the previous approaches listed above, the NMP model is entirely physics based and its predictions for the capture and emission times can be derived rigorously from first principles. In this chapter, the treatment of defects as Markov chains within the four-state model is discussed. The derivation of capture and emission times from first principles using NMP theory will be adressed in Ch. 5.

3.1 State Diagram

At its core, the 4-State model consists of a point defect inside the oxide, which can switch between two stable states (1, 2) and two metastable states ($1'$, $2'$) according to Fig. 3.1. Here $1, 1'$ denote the neutral states, whereas $2, 2'$ represent the positively charged states. Within this model, a shift ΔV_th occurs only, when the defect captures or emits a charge, i.e. at the transitions $1 \Leftrightarrow 2'$ and $2 \Leftrightarrow 1'$. These transitions are in principle detectable in experiment. In contrary, the transitions $1 \Leftrightarrow 1'$ and $2 \Leftrightarrow 2'$ are related to structural relaxations of the defect without any charge transfer. Although these relaxations are not directly accessable to measurements, their existence is necessary to explain the observed

Die approbierte gedruckte Originalversion dieser Diplomarbeit ist an der TU Wien Bibliothek verfügbar
The approved original version of this thesis is available in print at TU Wien Bibliothek.
TU WIEN Bibliothek Your knowledge hub

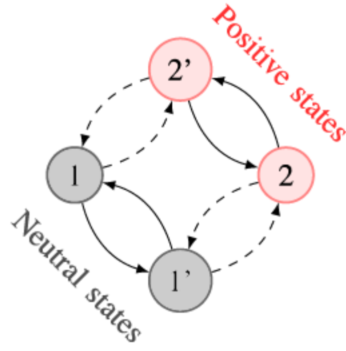

Figure 3.1: State-diagram of the 4-State defect for BTI. Dashed lines indicate charge transitions, whereas solid lines denote purely thermic transitions without any charge transfer. [21]

decoupling of emission and capture time constants, as well as the occurance of fixed positive traps [6, 55].

3.2 Master Equations and Occupancy

Within the 4-State model, the defect is assumed to be memory-less, implying that the transition rates from state i to state j, denoted by k_{ij}, only depend on the current state i but not on the history of the defect. This very important assumption is justified due to the extremly fast relaxation (several ps) [7] into the final state's equilibrium after an transition event regardless of the previous state. Mathematically this property is best described by a time-continous state-discrete Markov-chain [56]. Such a chain is given by a time-dependent random variable X_t over a discrete state space $\mathcal{S}$. The probability for a transition event from state i to state j during a small time interval $\Delta t > 0$ is then given by

$$\Pr\left\{\mathrm{X}_{t+\Delta t} = j | \mathrm{X}_t = i\right\} = k_{ij}\Delta t + o\left(\Delta t\right) \qquad \text{for } i \neq j. \tag{3.1}$$

It is not meaningful to introduce a rate k_{jj}, therefore the special case $j = i$ is treated by

$$\Pr\left\{\mathrm{X}_{t+\Delta t} = i | \mathrm{X}_t = i\right\} = 1 - \Pr\left\{\mathrm{X}_{t+\Delta t} \neq i | \mathrm{X}_t = i\right\} = 1 - \sum_{i \in \mathcal{S} \setminus \{j\}} k_{ij}\Delta t + o\left(\Delta t\right). \tag{3.2}$$

Since at any given time the system must be in exactly one state, the events $\mathrm{X}_t = i$ form a pairwise disjoint partition of the state space $\mathcal{S}$. For any such partition $\{B_i\}$, the law of total probability states that the total probability of an event A can be expressed through its conditional probabilities [57]:

$$\Pr\left\{A\right\} = \sum_{i \in \mathcal{S}} \Pr\left\{A | B_i\right\} \Pr\left\{B_i\right\}. \tag{3.3}$$

Die approbierte gedruckte Originalversion dieser Diplomarbeit ist an der TU Wien Bibliothek verfügbar
The approved original version of this thesis is available in print at TU Wien Bibliothek.
TU WIEN Bibliothek Your knowledge hub

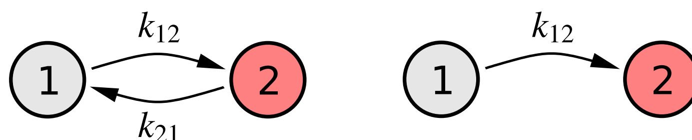

Figure 3.2: **Left:** Simple model of a 2-state defect. The defect can switch between a neutral (1) and a positive (2) state with transition rates k_{12} and k_{21}. **Right:** Model to calculate the first passage time for a hole capture event. [11]

The total probability of being in a state j at the time t is denoted by $P_j(t)$. In the limit $\Delta t \to 0$, Eq. 3.1 to 3.3 then yield [58, 56]

$$\dot{P}_j(t) = \lim_{\Delta t \to 0} \frac{P_j(t+\Delta t) - P_j(t)}{\Delta t} = \sum_{i \in \mathcal{S} \setminus \{j\}} k_{ij} P_i(t) - k_{ji} P_j(t) \ . \tag{3.4}$$

This so called Master equation governs the temporal evolution of the probability of being in state j. The Master equations for all possible states form a system of coupled linear differential equations, which can be expressed in matrix notation as

$$\dot{\boldsymbol{P}} = \underline{\boldsymbol{K}} \cdot \boldsymbol{P} \tag{3.5}$$

where $\underline{\boldsymbol{K}}$ is the transition matrix with coefficients

$$K_{ij} = \begin{cases} k_{ji} & \text{if } i \neq j\,, \\ -\sum_{l \in \mathcal{S} \setminus \{i\}} k_{il} & \text{otherwise} \end{cases} \ . \tag{3.6}$$

Using the matrix exponential, if the system's initial state is given by $\boldsymbol{P}(0)$, the future occupation probabilities are uniquelly determined by [59]

$$\boldsymbol{P}(t) = \exp\left(\underline{\boldsymbol{K}} t\right) \boldsymbol{P}(0) \ . \tag{3.7}$$

3.3 Capture and Emission Times

In principle, Eq. 3.7 describes an arbitrary complex Markov-chain completely, for application purposes however, some special cases should be considered individually. Up to now it was not described, how to compare experimental capture and emission times to theoretical rates in the four-state model. This will be adressed in the following section, which is based on the explanations given in [11].

3.3.1 Two-State System

First we will discuss the simple case of a 2-state defect as depicted in Fig. 3.2 (left). For this system, the Master equations are given by

$$\dot{P}_1(t) = -k_{12} P_1(t) + k_{21} P_2(t) \tag{3.8a}$$

$$\dot{P}_2(t) = -k_{21} P_2(t) + k_{12} P_1(t) \quad . \tag{3.8b}$$

Die approbierte gedruckte Originalversion dieser Diplomarbeit ist an der TU Wien Bibliothek verfügbar
The approved original version of this thesis is available in print at TU Wien Bibliothek.
TU WIEN Bibliothek Your knowledge hub

Using the relation $P_1(t) + P_2(t) = 1$ leads to

$$\dot{P}_1(t) = -(k_{12} + k_{21}) P_1(t) + k_{21} . \tag{3.9}$$

With the definitions

$$P_1(\infty) \triangleq \frac{k_{21}}{k_{12} + k_{21}} \quad \text{and} \quad \tau \triangleq \frac{1}{k_{12} + k_{21}} \tag{3.10}$$

the solution of Eq. 3.9 takes the form

$$P_1(t) = P_1(\infty) + [P_1(0) - P_1(\infty)] \exp(-t/\tau) . \tag{3.11}$$

It turns out, that regardless of the initial conditions, the system always reaches the same equilibrium occupation probabilities with the time constant τ. The equilibirum between hole capture and emission is solely determined by the capture and emission rates. Experimentally the equilibrium occupation can be extracted from the average duty cycle of the measured RTN signal.

3.3.2 First Passage Time

In order to extract informations about the distribution of capture and emission times from the two-state model, a simplified 'one-way' model is used. Fig. 3.2 (right) shows the state-diagram to extract the statistics of the hole capture time τ_c. It is assumed, that the defect is initially neutral, thus $P_1(0) = 1$. The time to reach state 2 for the first time is called the first passage time τ_{12} from state 1 to state 2. τ_{12} is therefore only dependent on k_{12}, the rate k_{21} for the backward transition can be set to zero. The 2-state Master equations then yield the solution

$$P_1(t) = \exp(-k_{12} t) \tag{3.12a}$$

$$P_2(t) = 1 - \exp(-k_{12} t) . \tag{3.12b}$$

Since the system reaches state 2 only after the first passage time has passed, $P_2(t)$ can be interpreted as the probability that $\tau_{12} < t$ and is therefore identical to the cumulative distribution function (CDF) of τ_{12}:

$$F_{\tau_{12}}(t) \triangleq \Pr\{\tau_{12} < t\} = P_2(t) \tag{3.13}$$

Thus the probability density function (PDF) of τ_{12} is given by

$$f_{\tau_{12}}(t) \triangleq \frac{\mathrm{d}F_{\tau_{12}}}{\mathrm{d}t} = \dot{P}_2(t) = k_{12} \exp(-k_{12} t) . \tag{3.14}$$

This calculation reveals that τ_{12}, and therefore τ_c, is an exponentially distributed random variable. The expectation value $\overline{\tau_c}$ then follows by

$$\overline{\tau_c} = \mathbb{E}[\tau_{12}] \triangleq \int_0^\infty t \cdot f_{\tau_{12}}(t) \mathrm{d}t = \frac{1}{k_{12}} . \tag{3.15}$$

A similar procedere for the first passage time τ_{21} yields

$$\overline{\tau_e} = \mathbb{E}[\tau_{21}] = \frac{1}{k_{21}} . \tag{3.16}$$

Die approbierte gedruckte Originalversion dieser Diplomarbeit ist an der TU Wien Bibliothek verfügbar
The approved original version of this thesis is available in print at TU Wien Bibliothek.
TU WIEN Bibliothek Your knowledge hub

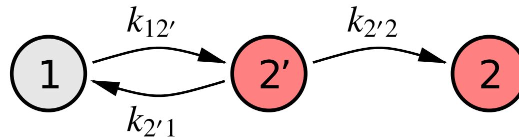

Figure 3.3: State diagram to determine the first passage time for a transition from state 1 to 2 over the intermediate state 2′. [11]

3.3.3 Three-State System

Transitions between state 1 and 2 do not occur directly in the four-state model, instead the transition occurs across the metastable state 2′ as depicted in Fig. 3.3. To obtain the first passage time τ_{12} and thus $\overline{\tau_{\mathrm{c}}}$, the Master equations

$$\dot{P}_1(t) = -k_{12'}P_1(t) + k_{2'1}P_{2'}(t) \tag{3.17a}$$
$$\dot{P}_{2'}(t) = k_{12'}P_1(t) - (k_{2'1} + k_{2'2})\,P_{2'}(t) \tag{3.17b}$$
$$\dot{P}_2(t) = k_{2'2}P_{2'}(t) \tag{3.17c}$$

with the inital conditions $P_1(0) = 1$ and $P_{2'}(0) = P_2(0) = 0$ have to be solved. Introducing the abbrevations

$$s \triangleq k_{12'} + k_{2'1} + k_{2'2} \qquad \tau_1^{-1} \triangleq \frac{1}{2}\left(s + \sqrt{s^2 - 4k_{2'1}k_{2'2}}\right)$$
$$\tau_2^{-1} \triangleq \frac{1}{2}\left(s - \sqrt{s^2 - 4k_{2'1}k_{2'2}}\right)$$

the resulting probability density function of τ_{12} can be expressed as

$$f_{\tau_{12}}(t) = \frac{\exp(-t/\tau_2) - \exp(-t/\tau_1)}{\tau_2 - \tau_1}\,. \tag{3.18}$$

The average capture time $\overline{\tau_{\mathrm{c}}}$ is then given by

$$\overline{\tau_{\mathrm{c}}} = \mathbb{E}[\tau_{12}] = \tau_1 + \tau_2\,. \tag{3.19}$$

Although in a three-state system τ_{12} does not follow an exponential distribution exactly, the experimentally important case of $\tau_1 \ll \tau_2$, can be reasonably approximated by an effective 2-state system as shown in Fig. 3.4. This approximation yields good results for $t \geq \tau_1$, but overestimates the probability of capture times smaller than τ_1, since the intermediate transition $1 \Leftrightarrow 2'$ sets a lower limit for the overall first passage time.

With the state diagram Fig. 3.3 the temporary RTN phenomenon depicted in Fig. 2.2 can be explained easily. In this case, the defect switches between the states $1 \Leftrightarrow 2'$ and generates a normal RTN signal until it reaches the stable state 2 and stays there.

Die approbierte gedruckte Originalversion dieser Diplomarbeit ist an der TU Wien Bibliothek verfügbar
The approved original version of this thesis is available in print at TU Wien Bibliothek.
TU WIEN Bibliothek Your knowledge hub

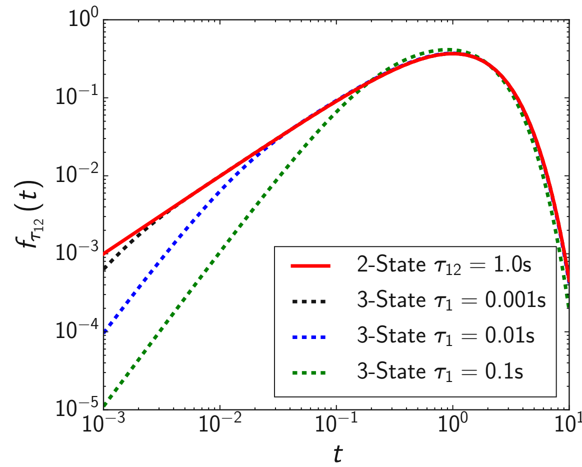

Figure 3.4: Comparison of τ_{12} distributions for a 2-state system and several 3-state systems with the same mean time $\overline{\tau}_{12} = \tau_1 + \tau_2$ but different values for τ_1. Reprinted from [11]

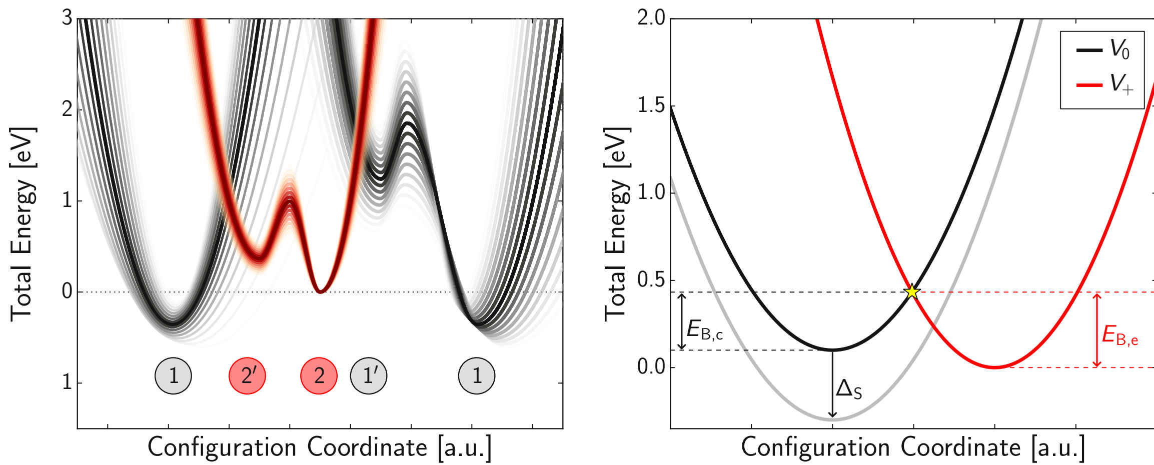

Figure 3.5: **Left:** Schematic energy profiles between the different states of the four-state model obtained from TDDS measurements. The ensemble of energy curves depict the experimental spread of defect parameters.[20] **Right:** Schematic energy profiles for the transitions $1 \Leftrightarrow 2'$. In a classical approach, the transition is assumed to occur at the intersection point of the two energy curves. Applying an electric field F_{ox} shifts the energies of the differently charged states relative to each other by Δ_S. [8]

Die approbierte gedruckte Originalversion dieser Diplomarbeit ist an der TU Wien Bibliothek verfügbar
The approved original version of this thesis is available in print at TU Wien Bibliothek.
TU WIEN Bibliothek Your knowledge hub

3.4 Energy Barriers

As shown in the last section, the transition rates k_{ij} in the four-state model solely determine the resulting capture and emission times. Therefore, the experimentally observed dependence of τ_c and τ_e on the temperature and the applied bias, as discussed in Sec. 2.3, must also be represented by these rates. In a physical picture, the transition rate k_{ij} for a certain reaction $i \Rightarrow j$ depends on the energy barrier E_{ij}, which has to be overcome for this reaction. Assuming first order reaction dynamics, the empirical Arrhenius law [60] yields a relation between transition rate and energy barrier of the form

$$k_{ij} \propto \exp\left(-\beta E_{ij}\right) , \qquad \beta \triangleq \frac{1}{k_\mathrm{B} T} \tag{3.20}$$

where k_B denotes the Boltzmann constant. Plotting the potential energy surface (see Sec. 4.1 for further details) of the system along the reaction path leads to energy profiles as shown in Fig. 3.5. In these plots, the different states of the system are given by the local minima of the energy profiles. In the case of purely thermic transitions, i.e. $1 \Leftrightarrow 1'$ and $2 \Leftrightarrow 2'$, the energy barrier is determined by the highest energy along the reaction path, the corresponding configuration is called transition state. For the charge transitions $1 \Leftrightarrow 2'$ and $2 \Leftrightarrow 1'$ however, a change in the electronic state of the system occurs. This means, that during the transition the system switches from one energy surface to the other. In the classical limit of NMP theory, such a transition occurs at the intersection point of the two involved energy surfaces, as depicted in Fig. 3.5 (right). The exact relations, derived by ab initio principles, between transition rates and energy barriers will be described in greater detail in Ch. 5.

The influence of an electric field in the oxide is introduced by a shift of Δ_S between the neutral and positive charged energy surface. Assuming, the oxid field does not deform the energy surfaces, the shift Δ_S is given by [7]

$$\Delta_\mathrm{S} \cong Q x_\mathrm{t} F_\mathrm{ox} , \tag{3.21}$$

where Q is the charge of the defect and x_t denotes the distance of the defect from the oxide/channel interface. The shift Δ_S obviously changes the intersection point and thus changes the barriers for charge capture and emission. See Sec. 5.4.3 for more details.

Fig. 3.5 (left) shows the experimental distribution of energy levels obtained by TDDS measurements in a 2.2nm SiON device [22]. The wide distribution of barrier heights is a consequence of the typically amorphous oxide layer, which results in slightly different environments for each defect. This leads to a spreading of resulting capture and emission times over several orders of magnitude. In the full four-state model, the transition from state 1 to 2 is possible via two different paths, namely $1 \Leftrightarrow 2' \Rightarrow 2$ and $1 \Leftrightarrow 1' \Rightarrow 2$, see Fig. 3.1. Given the right energy levels, these two competing paths can give rise to a bias independent emission time τ_e as encountered in the case of an fixed positive trap (see Fig. 2.3 (right)). If one of the paths is blocked due to a high energy barrier, the corresponding defect will function as an fixed trap. [8]

Die approbierte gedruckte Originalversion dieser Diplomarbeit ist an der TU Wien Bibliothek verfügbar
The approved original version of this thesis is available in print at TU Wien Bibliothek.
TU WIEN Bibliothek Your knowledge hub

3.5 Suspected BTI Causing Defects in SiO_2

Over the last decades BTI measurements have revealed the macroscopic behavior of oxide defects and helped to accurately model the device degradation caused by BTI. The detailed underlying physical mechanisms, however, remain uncertain. Although some models suggested oxygen vacancies (OV) as the cause of BTI [61], it was recently demonstrated with ab-initio calculations that the energy levels of an OV defect rule out an electrically active charge trapping site [20]. Other authors found a direct link between BTI degradation and the presence of hydrogen [62, 63, 64, 65], suggesting hydrogen based defects such as the hydrogen bridge (HB) or the hydroxyl-E′ center (HE′) as likely defect candidates for BTI. These three defect types together with their different configurations within the four-state model will be discussed in the following.

3.5.1 Oxygen Vacancy

The oxygen vacancy (OV) probably is the most studied defect in SiO_2 [15, 16, 17]. This defect forms, if an oxygen atom is missing in the SiO_2 structure, leaving behind a Si–Si dimer as shown in Fig. 3.6 (OV, 1). When the OV traps a hole from the substrate, the missing electron causes the Si–Si bond to break, resulting in a paramagnetic E′ center (OV, 2′). These two states correspond to the stable neutral state 1 and the metastable positive state 2′. A structural change without charge transition can occur in both charge states, when one of the Si atoms moves through the plane spanned by its three oxygen neighbours (OV 1′ and 2). These states are often referred to as "puckered" configurations and require a nearby 4th oxygen atom to stabilize the Si in its new position. [8]

3.5.2 Hydrogen Bridge

Although the oxygen vacancy appears to be electrically inactive, it is the precursor of another related defect, the hydrogen bridge (HB), which was shown to support a four-state model for BTI [20]. A hydrogen bridge forms, when a hydrogen atom is incorporated into an OV. This can also be considered as the replacement of an O atom with a H atom in the defect-free structure. The stable neutral state of this defect is depicted in Fig. 3.6 (HB 1). As shown, the H atom is bound to only one of the two involved Si atoms, whereas the other Si has an unpaired electron. When charged positively, the unpaired electron is removed, resulting in the H atom being bound to both Si atoms (HB 2′). Similar to the OV, a puckering transition can occur in both charge states, where the Si atom without hydrogen moves through the plane of its neighbouring O atoms. [66]

3.5.3 Hydroxyl-E′ Center

Recently another promising hydrogen induced defect was discovered in amorphous SiO_2. The so called Hydroxyl-E′ center (H-E′) forms, when a hydrogen atom binds to an oxygen and thereby breaks one of the two Si–O bonds, resulting in a threefold-coordinated

Die approbierte gedruckte Originalversion dieser Diplomarbeit ist an der TU Wien Bibliothek verfügbar
The approved original version of this thesis is available in print at TU Wien Bibliothek.
TU Bibliothek WIEN Your knowledge hub

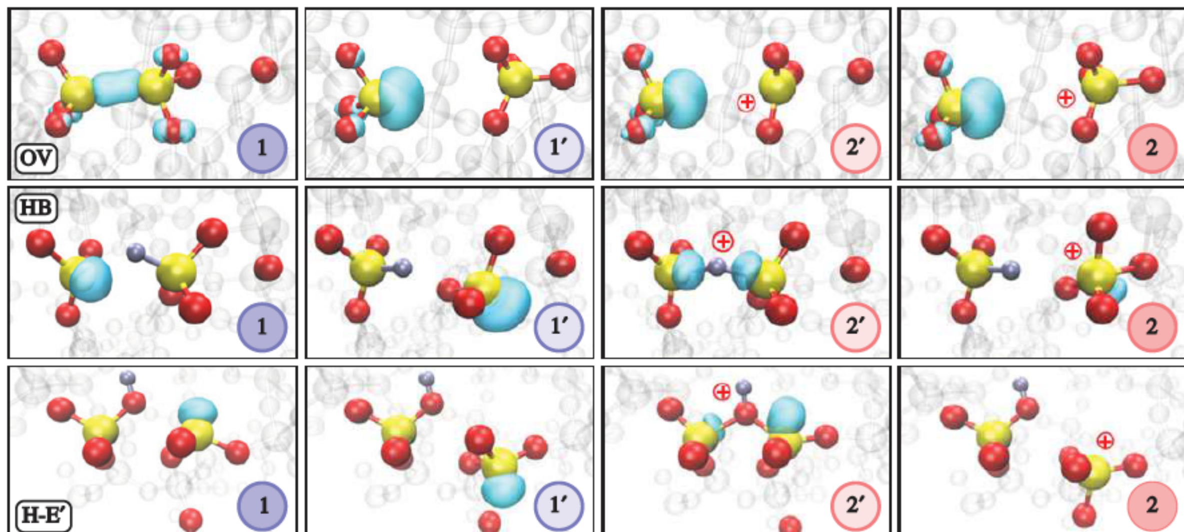

Figure 3.6: Possible defect candidates for BTI with different configurations corresponding to the states of the four-state model in amorphous SiO_2. Si atoms are colored yellow, O atoms red and H atoms silver. The turquoise "bubbles" represent the highest occupied molecular orbital (HOMO) in the case of neutral states and the lowest unoccupied molecular orbital (LUMO) for positive states. All three defect types can undergo what is called a "puckering" transition, where one Si atom moves through the plane spanned by its 3 oxygen neighbors ($1 \Leftrightarrow 1'$ and $2 \Leftrightarrow 2'$). [20].

Si atom with an unpaired electron (see Fig. 3.6 H-E′ 1). It is reported, that this H induced bond-breaking can only occur at strained Si–O bonds with bond lengths larger than 1.65Å, therefore in contrary to the defects discussed above, the H-E′ can only exist in amorphous SiO_2 but not in crystalline structures like α-quartz [9]. When a hole is captured, the broken Si–O bond is restored and the positively charged H ion is still attracted to the bound O atom, leading to a nearly symmetric configuration (H-E′ 2′). Similar the other two discussed defects, the H-E′ supports a puckering transition leading to the states 1′ and 2. [20]

Die approbierte gedruckte Originalversion dieser Diplomarbeit ist an der TU Wien Bibliothek verfügbar
The approved original version of this thesis is available in print at TU Wien Bibliothek.
TU Bibliothek WIEN Your knowledge hub

Die approbierte gedruckte Originalversion dieser Diplomarbeit ist an der TU Wien Bibliothek verfügbar
The approved original version of this thesis is available in print at TU Wien Bibliothek.
TU WIEN Bibliothek Your knowledge hub

CHAPTER 4 Density Functional Theory

Ab-initio simulation of defect behaviors requires to solve the Schroedinger equation of the considered many-body problem. This is computationally highly demanding and thus requires certain concepts and approximations in practice. One of the most popular ab-initio approaches used in computational chemistry is density functional theory (DFT). For the scope of this work, DFT is a crucial part to obtain defect parameters in amorphous SiO_2. This chapter is dedicated to explain the theoretical foundations of DFT as well as the computational techniques and settings used to perform calculations in this work.

4.1 Born-Oppenheimer Approximation

Within the first quantization approach, the properties of an arbitrary system consisting of N_{nuc} nuclei and N_{el} electrons can be determined by solving the time-independent Schroedinger equation

$$\hat{H}\,|\Phi\,(\boldsymbol{r},\boldsymbol{R})\rangle = E\,|\Phi\,(\boldsymbol{r},\boldsymbol{R})\rangle \tag{4.1}$$

where $|\Phi\,(\boldsymbol{r},\boldsymbol{R})\rangle$ denotes the system's wave function and

$$\boldsymbol{r} \triangleq [\boldsymbol{r}_1,\ldots,\boldsymbol{r}_{N_{\mathrm{el}}}] \in \mathbb{R}^{3N_{\mathrm{el}}}\,, \qquad \boldsymbol{R} \triangleq [\boldsymbol{R}_1,\ldots,\boldsymbol{R}_{N_{\mathrm{nuc}}}] \in \mathbb{R}^{3N_{\mathrm{nuc}}} \tag{4.2}$$

are vectors, collecting all electron and nuclei positions respectively. The general many-body hamiltonian is given by [67]

$$\hat{H} \triangleq \hat{T}_{\mathrm{el}} + \hat{T}_{\mathrm{nuc}} + v_{\mathrm{el-el}} + v_{\mathrm{nuc-nuc}} + v_{\mathrm{el-nuc}}\,. \tag{4.3}$$

Using atomic units [68], the different terms are given as follows:

i) The kinetic energy of the electrons yields

$$\hat{T}_{\mathrm{el}} \triangleq = -\frac{1}{2}\sum_{i=1}^{N_{\mathrm{el}}} \nabla^2_{\boldsymbol{r}_i} \tag{4.4a}$$

with the Laplace operator $\nabla^2_{\boldsymbol{r}_i} = \left(\partial^2/\partial r_{ix}^2 + \partial^2/\partial r_{iy}^2 + \partial^2/\partial r_{iz}^2\right)$.

Die approbierte gedruckte Originalversion dieser Diplomarbeit ist an der TU Wien Bibliothek verfügbar
The approved original version of this thesis is available in print at TU Wien Bibliothek.
TU WIEN Bibliothek Your knowledge hub

ii) Similarly the nuclei kinetic energy is given by

$$\hat{T}_{\text{nuc}} \triangleq = -\frac{1}{2}\sum_{i=1}^{N_{\text{nuc}}} \frac{1}{M_i}\nabla^2_{\boldsymbol{R}_i} , \tag{4.4b}$$

where M_i denotes the mass of the i-th nucleus as a multiple of the electron mass.

iii) The coloumb interaction between electrons

$$v_{\text{el-el}}(\boldsymbol{r}) \triangleq \frac{1}{2}\sum_{i,j=1}^{N_{\text{el}}} \frac{1}{|\boldsymbol{r}_i - \boldsymbol{r}_j|} \tag{4.4c}$$

iv) The coloumb interaction between the nuclei

$$v_{\text{nuc-nuc}}(\boldsymbol{R}) \triangleq \frac{1}{2}\sum_{i,j=1}^{N_{\text{nuc}}} \frac{Z_i Z_j}{|\boldsymbol{R}_i - \boldsymbol{R}_j|} , \tag{4.4d}$$

where Z_i denotes the atomic number of the corresponding nucleus.

v) The coloumb interaction between electrons and nuclei

$$v_{\text{el-nuc}}(\boldsymbol{r}, \boldsymbol{R}) \triangleq -\sum_{i=1}^{N_{\text{el}}}\sum_{j=1}^{N_{\text{nuc}}} \frac{Z_j}{|\boldsymbol{r}_i - \boldsymbol{R}_j|} \tag{4.4e}$$

Although Eq. 4.1 describes the whole system in theory, it can only be solved for the most simple diatomic molecules. To overcome this, Born and Oppenheimer proposed a separation of the electron and nuclei dynamics, known as the Born-Oppenheimer approximation (BOA) [69, 70]. This approach is justified, because electrons have much less mass than nuclei and therefore can adjust to changes in nuclei positions almost instantly. Mathematically, the BOA seperates Eq. 4.1 in an electronic and a vibronic Schroedinger equation.

The electronic part describes the electrons in a potential defined by the coloumb interactions among themselves and with the fixed nuclei at the positions $\boldsymbol{R}$. The electronic Schroedinger equation is given by

$$\left(\hat{T}_{\text{el}} + v_{\text{ext}}(\boldsymbol{r}) + v_{\text{el-el}}(\boldsymbol{r})\right)|\Psi_k(\boldsymbol{r};\boldsymbol{R})\rangle = V_k(\boldsymbol{R})\,|\Psi_k(\boldsymbol{r};\boldsymbol{R})\rangle , \tag{4.5}$$

where $|\Psi_k(\boldsymbol{r};\boldsymbol{R})\rangle$ is an electronic eigenstate of the system to the eigenvalue $V_k(\boldsymbol{R})$. The external potential $v_{\text{ext}}(\boldsymbol{r})$ contains all potentials felt by the electrons beside their interaction with themselves. Other influences like an external electric field can also be incorporated in $v_{\text{ext}}(\boldsymbol{r})$. Note that $\boldsymbol{R}$ acts only as a parameter and Eq. 4.5 therefore defines a map

$$V_k : \mathbb{R}^{3N_{\text{nuc}}} \to \mathbb{R},\ \boldsymbol{R} \mapsto V_k(\boldsymbol{R}) , \tag{4.6}$$

Die approbierte gedruckte Originalversion dieser Diplomarbeit ist an der TU Wien Bibliothek verfügbar
The approved original version of this thesis is available in print at TU Wien Bibliothek.
TU WIEN Bibliothek Your knowledge hub

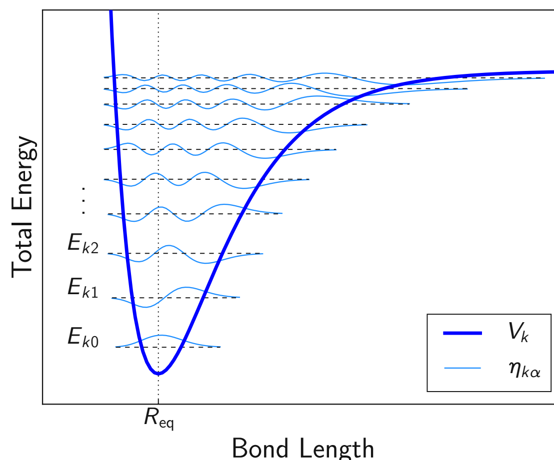

Figure 4.1: Vibrational eigenstates in a one-dimensional Morse potential. The vibronic wave functions are offset by the eigenenergy $E_{k\alpha}$ of the corresponding state for illustration purposes.

which assignes an effective potential energy to every set of nuclei positions $\boldsymbol{R}$. This map is commonly known as the potential energy surface (PES) of the electronic state $|\Psi_k(\boldsymbol{r};\boldsymbol{R})\rangle$. If a certain reaction path $\boldsymbol{R}(q)$ is chosen, the potential energy along the reaction coordinate q yields a potential energy profile

$$V_k(q) \triangleq V_k(\boldsymbol{R}(q)) \tag{4.7}$$

which was already implicitly used in Fig. 3.5. As will be discussed in Ch. 6, the reduction of the PES to a one-dimensional energy curve is necessary to perform the calculations for the scope of this work.

The vibronic part of Eq. 4.1 describes the movement of nuclei on the potential energy surface and is given by

$$\left(\hat{T}_{\text{nuc}} + V_k(\boldsymbol{R})\right)|\eta_{k\alpha}(\boldsymbol{R})\rangle = E_{k\alpha}|\eta_{k\alpha}(\boldsymbol{R})\rangle \ , \tag{4.8}$$

where $|\eta_{k\alpha}(\boldsymbol{R})\rangle$ is a vibronic eigenstate of the electronic eigenstate $|\Psi_k(\boldsymbol{r};\boldsymbol{R})\rangle$. The solutions of Eq. 4.8 are sketched in Fig. 4.1 for the simple case of a one-dimensional Morse potential [71], which is often used to model the dissociation of a diatomic molecule. As can be seen, there are multiple vibrational modes for one electronic state. The wave functions $|\eta_{k\alpha}(\boldsymbol{R})\rangle$ indicate, that the diatomic molecule vibrates around its equilibrium position, which is given by the minimum of the potential energy surface. In general, local minima of the PES always indicate a stable or metastable configuration. Furthermore the concept of potential energy surfaces and their vibrational modes is crucial to extract transition rates from ab-initio calculations by using NMP and transition state theory (TST) in Ch. 5. The remainder of this chapter deals with solving the electronic part Eq. 4.5 using DFT.

Die approbierte gedruckte Originalversion dieser Diplomarbeit ist an der TU Wien Bibliothek verfügbar
The approved original version of this thesis is available in print at TU Wien Bibliothek.
TU WIEN Bibliothek Your knowledge hub

4.2 Hohenberg-Kohn Theorems

For many practical purposes, including the scope of this work, only the electronic ground state $|\Psi_0(\boldsymbol{r};\boldsymbol{R})\rangle$ is of interest. Using density functional theory the ground state can be calculated even for very large systems with several thousands of atoms [72]. Density functional theory is based on two fundamental properties of the ground state, which were first proven by Hohenberg and Kohn in 1964 [73]. The Hohenberg-Kohn theorems can be stated as [74]:

i) All electronic ground state properties, including the ground state energy E_0, are uniquely determined by the electron density ρ. As a consequence there exists an energy functional in the form $E[\rho]$.

ii) The energy functional $E[\rho]$ is minimal for the true ground state density ρ_0 and yields the ground state energy $E_0 = E[\rho_0]$

It is trivial that the electron density can be uniquely determined by the electron wave function:

$$\rho_0(\boldsymbol{r}) = \langle\Psi_0|\sum_{i=1}^{N_{\text{el}}}\delta(\boldsymbol{r}-\boldsymbol{r}_i)|\Psi_0\rangle \tag{4.9}$$

The first theorem states, that the reverse also holds true. Hence, the system energy E is a functional of the electron density:

$$E[\rho(\boldsymbol{r})] = \langle\Psi|\hat{H}_{\text{el}}|\Psi\rangle \tag{4.10}$$

According to the second theorem, the ground state density ρ_0 is the solution of the variational problem

$$\delta E[\rho(\boldsymbol{r})] = 0 \quad \text{with the constraint} \quad \int \rho(\boldsymbol{r})\,\mathrm{d}^3\boldsymbol{r} = N_{\text{el}}\,. \tag{4.11}$$

So far, the variational problem Eq. 4.11 is equivalent to the electronic Schroedinger Eq. 4.5, but the dimension of the problem is significantly reduced from $3N_{\text{el}}$ for the electronic wave function $|\Psi_0\rangle$ to only 3 for the electron density ρ. The density functional 4.10 can be split in several parts:

$$E[\rho] = T[\rho] + V_{\text{ext}}[\rho] + U[\rho] \tag{4.12}$$

The contribution of the external potential to the total energy is given by

$$V_{\text{ext}}[\rho] \triangleq \int v_{\text{ext}}(\boldsymbol{r})\,\rho(\boldsymbol{r})\,\mathrm{d}^3\boldsymbol{r}\,, \tag{4.13}$$

whereas the functional for the kinetic energy $T[\rho]$ and the electron-electron interaction $U[\rho]$ are unknown. In order to solve Eq. 4.11, these functionals must be approximated.

Die approbierte gedruckte Originalversion dieser Diplomarbeit ist an der TU Wien Bibliothek verfügbar
The approved original version of this thesis is available in print at TU Wien Bibliothek.
TU WIEN Bibliothek Your knowledge hub

4.3 Kohn-Sham Equations

Although the kinetic energy functional is not known for a system of interacting electrons, the kinetic energy T_s of a fictional non-interacting system of single electrons with the wave functions $\psi_i(\boldsymbol{r})$ is simply given by

$$T_s = -\frac{1}{2}\sum_{i=1}^{N_{\mathrm{el}}} \int \psi_i^*(\boldsymbol{r}) \nabla^2 \psi_i(\boldsymbol{r}) \, \mathrm{d}^3\boldsymbol{r} \,. \tag{4.14}$$

Since all ground state properties can be determined from the electron density ρ, Kohn and Sham proposed to use non-interacting orbitals [75], the so-called Kohn-Sham orbitals which resemble the same electron density as the original system:

$$\rho_0(r) = \sum_{i=1}^{N_{\mathrm{el}}} |\psi_i(\boldsymbol{r})|^2 \,. \tag{4.15}$$

The real kinetic energy functional T then can be expressed as the sum of T_s and an exchange functional accounting for the electron exchange effects:

$$T[\rho] = T_s[\rho] + E_{\mathrm{X}}[\rho] \tag{4.16}$$

Similarly to T, the full interaction functional U remains unknown. However, its classical part is just the electrostatic energy associated with the charge distribution, the so-called Hartree energy :

$$U_H[\rho] = \frac{1}{2}\iint \frac{\rho(\boldsymbol{r})\,\rho(\boldsymbol{r}')}{|\boldsymbol{r}-\boldsymbol{r}'|} \mathrm{d}^3\boldsymbol{r}\,\mathrm{d}^3\boldsymbol{r}' \,. \tag{4.17}$$

When outsourcing all many-body quantum effects in a correlation energy $E_{\mathrm{C}}[\rho]$, the interaction functional can be written as

$$U[\rho] = U_{\mathrm{H}}[\rho] + E_{\mathrm{C}}[\rho] \,. \tag{4.18}$$

With this notations, the energy functional Eq. 4.12 becomes

$$E[\rho] = T_s[\rho] + V_{\mathrm{ext}}[\rho] + U_H[\rho] + E_{\mathrm{XC}}[\rho] \quad \text{with} \quad E_{\mathrm{XC}}[\rho] = E_{\mathrm{X}}[\rho] + E_{\mathrm{C}}[\rho] \,. \tag{4.19}$$

Applying the Euler-Lagrange equations [76] to solve the variational problem Eq. 4.11 then yields a system of one-particle Schroedinger equations for the wavefunctions ψ_i, known as the Kohn-Sham equations:

$$\left(-\frac{1}{2}\nabla^2 + v_{\mathrm{eff}}(\boldsymbol{r})\right)\psi_i(\boldsymbol{r}) = \epsilon_i \psi_i(\boldsymbol{r}) \tag{4.20}$$

The Kohn-Sham equations describe N_{el} non-interacting electrons in an effective potential v_{eff} which is given by [77]

$$v_{\mathrm{eff}}(\boldsymbol{r}) = v_{\mathrm{ext}}(\boldsymbol{r}) + v_{\mathrm{H}}(\boldsymbol{r}) + v_{\mathrm{XC}}(\boldsymbol{r}) \tag{4.21}$$

TU WIEN Bibliothek Your knowledge hub
Die approbierte gedruckte Originalversion dieser Diplomarbeit ist an der TU Wien Bibliothek verfügbar
The approved original version of this thesis is available in print at TU Wien Bibliothek.

with the Hartree potential

$$v_{\mathrm{H}}(\boldsymbol{r}) \triangleq \left.\frac{\delta U_{\mathrm{H}}[\rho]}{\delta \rho}\right|_{\rho=\rho_0} = \int \frac{\rho_0(\boldsymbol{r}')}{|\boldsymbol{r}-\boldsymbol{r}'|} \mathrm{d}^3\boldsymbol{r}' \tag{4.22}$$

and the exchange-correlation potential

$$v_{\mathrm{XC}}(\boldsymbol{r}) \triangleq \left.\frac{\delta E_{\mathrm{XC}}[\rho]}{\delta \rho}\right|_{\rho=\rho_0} . \tag{4.23}$$

Here $\delta/\delta\rho$ denotes the functional derivative [78] with respect to ρ. The Kohn-Sham equations are a system of nonlinear eigenvalue problems, which have to be solved self consistently. To achieve this, an initial density ρ_{init} is assumed and the Kohn-Sham equations are solved to obtain a set of Kohn-Sham orbitals. These orbitals then yield a new density via Eq. 4.15 and the Kohn-Sham equations are solved again with this new density. This iterative cycle continues until ψ_i^k and ψ_i^{k+1} are equal within a set tolerance. The total ground energy E_0 then can be calculated from the Kohn-Sham energies ϵ_i by

$$E_0 = \sum_{i=1}^{N_{\mathrm{el}}} \epsilon_i - U_H[\rho_0] + E_{\mathrm{XC}}[\rho_0] - \int v_{\mathrm{XC}}(\boldsymbol{r})\, \rho_0(\boldsymbol{r})\, \mathrm{d}^3\boldsymbol{r} \,. \tag{4.24}$$

4.4 Exchange-Correlation Functionals

It should be noted, that the obtained E_0 is not exact since all many-body quantum effects are collected in the exchange-correlation functional $E_{\mathrm{XC}}[\rho]$, which is unknown. The results from DFT calculations therefore heavily depend on the used approximation for E_{XC}. In the following, the most common functionals used in practical DFT calculations are discussed.

4.4.1 Local Density Approximation

The local density approximation (LDA) functional was first introduced in the original work of Kohn and Sham [75]. It assumes a slowly varying electron density and treats the system as a locally homogenous electron gas (HEG). Consequently this functional is solely dependent on the local density:

$$E_{\mathrm{XC}}^{\mathrm{LDA}}[\rho] = \int \varepsilon_{\mathrm{XC}}(\rho)\, \rho(\boldsymbol{r})\, \mathrm{d}^3\boldsymbol{r} \,. \tag{4.25}$$

Under the assumation of a HEG, the exchange functional ϵ_{X} can be derived as [79]

$$\varepsilon_{\mathrm{X}}(\rho) = -\frac{3}{4}\left(\frac{3\rho}{\pi}\right)^{1/3} . \tag{4.26}$$

The correlation functional ε_{C} on the other hand was accurately determined by quantum mechanical Monte Carlo calculations [80]. Although LDA was the first proposed and most simple functional for DFT, it yields quite accurate results for solids, but in general tends to overestimate binding energies [81].

Die approbierte gedruckte Originalversion dieser Diplomarbeit ist an der TU Wien Bibliothek verfügbar
The approved original version of this thesis is available in print at TU Wien Bibliothek.
TU WIEN Bibliothek Your knowledge hub

4.4.2 Generalized Gradient Approximation

Due to its derivation from the HEG, the LDA falls short for rapidly changing charge densities. Since this work attends to study defects in SiO_2 with localized charges, the LDA is not suitable for this purpose [82]. The LDA can be improved by introducing a dependence on the spatial change of the electron density. This leads to the generalized gradient approximation (GGA)

$$E_{\mathrm{XC}}^{\mathrm{GGA}}[\rho] = \int \varepsilon_{\mathrm{XC}}(\rho, \nabla\rho)\, \rho(\boldsymbol{r})\, \mathrm{d}^3\boldsymbol{r}\,. \tag{4.27}$$

The use of GGA over LDA can significantly improve the accuracy of DFT calculations [83, 84]. Contrary to LDA, several different proposals for the form of $E_{\mathrm{XC}}^{\mathrm{GGA}}$ exist. Among the most popular are models like PBE (Perdew-Burke-Ernzerhof) [85] and PW91 (Perdew-Wang) [86]. Even more sophisticated functionals, known as meta-GGA, assume an exchange-correlation function $\varepsilon_{\mathrm{XC}}(\rho, \nabla\rho, t_s)$, where the second spatial derivative of ρ is implicitly introduced by a dependence on the kinetic energy density t_s [87]

$$t_s(\boldsymbol{r}) = -\frac{1}{2}\sum_{i=1}^{N_{\mathrm{el}}} \psi_i^*(\boldsymbol{r})\, \nabla^2\psi_i(\boldsymbol{r})\ . \tag{4.28}$$

4.4.3 Hybrid Functionals

Both LDA and GGA are known to grossly underestimate the electronic bandgap [88]. To circumvent this disadvantage, so-called hybrid functionals were developed. These functionals employ the exact nonlocal Hartree-Fock exchange (HFX) functional [89]

$$E_{\mathrm{X}}^{\mathrm{HF}}[\rho] = -\frac{1}{2}\sum_{i,j=1}^{N_{\mathrm{el}}} \iint \psi_i^*(\boldsymbol{r})\, \psi_j^*(\boldsymbol{r}')\, g(|\boldsymbol{r}-\boldsymbol{r}'|)\, \psi_i(\boldsymbol{r}')\, \psi_j(\boldsymbol{r})\mathrm{d}^3\boldsymbol{r}\mathrm{d}^3\boldsymbol{r}'\,, \tag{4.29}$$

where g denotes the ordinary Coulomb operator

$$g(\boldsymbol{r}) \triangleq \frac{1}{|\boldsymbol{r}|}\,. \tag{4.30}$$

In order to compute the HFX functional efficiently, often a truncated Coulomb operator g_{TC} is used [90]:

$$g_{\mathrm{TC}} \triangleq \begin{cases} g(\boldsymbol{r}) & \text{if} \quad |\boldsymbol{r}| \leq r_{\mathrm{TC}} \\ 0 & \text{otherwise} \end{cases} \tag{4.31}$$

A hybrid functional usually is a linear combination of $E_{\mathrm{X}}^{\mathrm{HF}}$ and some other GGA functional. For example, the popular PBE0 hybrid functional [91] is given by

$$E_{\mathrm{XC}}^{\mathrm{PBE0}}[\rho] = \frac{1}{4}E_{\mathrm{X}}^{\mathrm{HF}}[\rho] + \frac{3}{4}E_{\mathrm{X}}^{\mathrm{PBE}}[\rho] + E_{\mathrm{C}}^{\mathrm{PBE}}[\rho]\ . \tag{4.32}$$

Die approbierte gedruckte Originalversion dieser Diplomarbeit ist an der TU Wien Bibliothek verfügbar
The approved original version of this thesis is available in print at TU Wien Bibliothek.
TU Bibliothek Your knowledge hub WIEN

PBE0 and other hybrid functionals like HSE (Heyd-Scuseria-Ernzerhof) [92] or B3LYP (Becke, three-parameter, Lee-Yang-Parr) [93] have been demonstrated to predict the electronic structure of various semiconductors and insulators accurately (within 10% of the experimental value) [94]. Since this is very important for the study in this work, all DFT calculations have been carried out with a variant of the PBE0 functional.

4.5 Basis Sets

Solving the Kohn-Sham equations 4.20 numerically requires an expansion of the electron density ρ and the KS orbitals ψ_i into a set of basis functions. The basis set must be small enough, to allow efficient calculations. On the other hand, the chosen basis functions must be able to approximate the true electron density and the KS orbitals close enough in order to provide accurate results. DFT calculations are usually performed with either a plane wave or a gaussian basis set.

4.5.1 Plane Wave Basis Sets

DFT calculations in bulk materials require to impose periodic boundary conditions (PBC) on a simulation cell with a reasonable chosen volume Ω. According to Bloch's theorem [95] every electronic wavefunction $\psi_{i,\boldsymbol{k}}$ in a periodic lattice is the product of a periodic Bloch function $u(\boldsymbol{r})$ and a plain wave with wave vector $\boldsymbol{k}$:

$$\psi(\boldsymbol{r},\boldsymbol{k}) = u(\boldsymbol{r}) \exp(i\boldsymbol{k}\cdot\boldsymbol{r}) \tag{4.33}$$

In this study, we will restrict ourselfs to an analysis in the Γ point ($\boldsymbol{k}=0$), therefore every KS orbital can be expanded in the form

$$\psi_j(\boldsymbol{r}) = \frac{1}{\sqrt{\Omega}} \sum_{\boldsymbol{G}} \widetilde{\psi}_j(\boldsymbol{G}) \exp(i\boldsymbol{G}\cdot\boldsymbol{r}), \qquad \widetilde{\psi}_j(\boldsymbol{G}) = \frac{1}{\sqrt{\Omega}} \int_\Omega \psi_i(\boldsymbol{r}) \exp(-i\boldsymbol{G}\cdot\boldsymbol{r})\, \mathrm{d}^3\boldsymbol{r} \tag{4.34}$$

where $\boldsymbol{G}$ is an arbitrary reciprocal lattice vector and $\widetilde{\psi}_j(\boldsymbol{G})$ denotes the Fourier coefficients of ψ_j. Applying this expansion to the Kohn-Sham equation 4.20 and integration over the simulation cell yields [81]

$$\frac{1}{2}|\boldsymbol{G}|^2 \widetilde{\psi}_j(\boldsymbol{G}) + \sum_{\boldsymbol{G}'} \widetilde{v}_{\text{eff}}(\boldsymbol{G}') \widetilde{\psi}_j(\boldsymbol{G}-\boldsymbol{G}') = \epsilon_j \widetilde{\psi}_j(\boldsymbol{G}) . \tag{4.35}$$

Here the orthogonality of the basis set $\{\exp(i\boldsymbol{G}\cdot\boldsymbol{r})\}$ was used. Eq. 4.35 is an infinite system of linear equations for the unknown Fourier coefficients $\widetilde{\psi}_j(\boldsymbol{G})$. To make this problem solvable, the number of $\boldsymbol{G}$ points obviously must be constraint. In practice, only points where the kinetic energy of the associated plane wave is below a certain cutoff energy E_{cutoff} are considered:

$$\frac{1}{2}|\boldsymbol{G}|^2 \leq E_{\text{cutoff}} . \tag{4.36}$$

Die approbierte gedruckte Originalversion dieser Diplomarbeit ist an der TU Wien Bibliothek verfügbar
The approved original version of this thesis is available in print at TU Wien Bibliothek.
TU Bibliothek WIEN Your knowledge hub

Physically, this restriction limits the resolvable spatial frequency. Since the wave functions of the inner electrons vary rapidly over space, a large E_{cutoff}, and hence a huge number of basis functions, would be needed in order to capture their behavior. Usually, the inner shell electrons are not treated within DFT, because they do not engage in chemical bonding. However, their influence on the nuclei Coulomb potential cannot be ignored and is taken into account by pseudopotentials [96]. The usage of a plane wave basis set offers some significant advantages [97]:

i) Plane waves already satisfy the periodic boundary conditions, which are necessary to describe bulk material.

ii) As already mentioned, the plane waves $\{\exp(i\boldsymbol{G}\cdot\boldsymbol{r})\}$ build an orthogonal basis set due to their construction, this allows a fast calculation of overlap integrals.

iii) The use of plane waves allows very efficient computations for the Hartree energy $U_H[\rho]$ based on fast Fourier transformation (FFT) algorithms.

iv) Since plane waves are completely delocalized, the basis set is independent of the nuclei positions.

v) The size of the basis set is determined by the single parameter E_{cutoff}

On the other hand, a large number of basis functions is needed, in order to accurately reassemble the electron density. Furthermore plane waves necessarily require the use of a pseudopotential to be computationally feasible.

4.5.2 Gaussian Basis Sets

The main idea behind gaussian basis sets or gaussian type orbitals (GTO) is to use a basis set, which is centered at the nucleus and mimics atomic orbitals. A predecessor of GTOs were so-called Slater Type Orbitals (STO), which are defined as [98]

$$S_{klm}(r,\theta,\phi) = A_k r^{k-1}\exp(-\alpha_k r)\, Y_{lm}(\theta,\phi)\ , \tag{4.37}$$

where A_n is a normalization factor and $Y_{lm}(\theta,\phi)$ are the normalized spherical harmonics. Although a basis of STOs can reproduce molecular orbitals quite well, it is expensive to calculate matrix elements in this basis. It is computationally more feasible, to approximate Eq. 4.37 by the basis functions [99]

$$\varphi_{klm}(r,\theta,\phi) = r^{k-1}R_k(r)\, Y_{lm}(\theta,\phi) \tag{4.38}$$

where the radial term $R_k(r)$ is a linear combination of gaussian functions

$$R_k(r) = \sum_i c_{ki}\exp\left(-\alpha_{ki}r^2\right) \tag{4.39}$$

with the fitting parameters α_{ki} and c_{ki}. The set $\{\varphi_{klm}\}$ is called a contracted gaussian basis. The parameters of these sets are fitted to match experimental data for each

Die approbierte gedruckte Originalversion dieser Diplomarbeit ist an der TU Wien Bibliothek verfügbar
The approved original version of this thesis is available in print at TU Wien Bibliothek.
TU WIEN Bibliothek Your knowledge hub

chemical element individually. Carefully designed gaussian basis sets allow an accurate representation of the electron density and the KS orbitals, even with a small number of basis functions. Contrary to plane wave sets, a gaussian set can allow the calculation of all electrons in the system without the use of a pseudopotential. Nethertheless, gaussian basis set also have some downsides:

i) Gaussian sets are non-orthogonal and might not even be a basis set in a mathematical sense, leading to linear dependencies or overcompleteness.

ii) They depend on the atomic positions and have the wrong asymptotic behavior compared to STOs.

iii) Gaussian sets are not natively periodic.

4.6 CP2K Software Package

Since this work aims to evaluate the accuracy of the harmonic approximation of potential energy surfaces on a statistical level, many DFT calculations have to be performed. It is thus necessary to use a highly efficient DFT program. In this work the package CP2K [100] was used for DFT calculations, since it provides some significant advantages for the purpose of this work:

i) CP2K implements a hybrid basis set of plane waves and gaussian functions, known as the gaussian plane wave (GPW) method [97, 101]. This approach combines the advantages of both basis sets and allow the accurate describtion of large systems, like the amorphous SiO_2 structures used as a model for oxide layers in this work.

ii) In order to accurately predict defect energy levels, a hybrid functional as described in Sec. 4.4.3 must be used. Computing the Hartree-Fock exchange $E_{\mathrm{X}}^{\mathrm{HF}}[\rho]$ is of complexity $O(N^4)$ and thus quickly becomes the limiting factor in DFT calculations for large systems. CP2K offers an approximation technique, the auxiliary density matrix method (ADMM), which significantly reduces the costs to calculate the HF exchange [102].

In the following these two key methods are briefly discussed.

4.6.1 Gaussian Plane Waves Method

Plane wave and gaussian basis sets both have their own disadvantages, which limit their use to accurately describe systems with a large number of atoms. In [97] a method is demonstrated, to use both basis sets simultaneously and to overcome their downsides when used seperately. Similar strategies were also proposed in [103, 104].

The main idea is to expand the electron density in terms of a gaussian basis set

$$\rho(\boldsymbol{r}) = \sum_{\mu,\nu} P_{\mu\nu} \varphi_{\mu}(\boldsymbol{r}) \varphi_{\nu}(\boldsymbol{r}) \tag{4.40}$$

Die approbierte gedruckte Originalversion dieser Diplomarbeit ist an der TU Wien Bibliothek verfügbar
The approved original version of this thesis is available in print at TU Wien Bibliothek.
TU WIEN Bibliothek Your knowledge hub

where $P_{\mu\nu}$ denotes an element of the density matrix $\underline{\boldsymbol{P}}$. This representation is used to calculate the functionals of the kinetic energy $T[\rho]$ and the potential energy $V[\rho]$. Using FFT, the gaussian representation of the electron density can be mapped to an expansion in an auxiliary plane wave basis

$$\rho(\boldsymbol{r}) = \frac{1}{\Omega}\sum_{\boldsymbol{G}} \widetilde{\rho}(\boldsymbol{G}) \exp(i\boldsymbol{G}\cdot\boldsymbol{r}) \ . \tag{4.41}$$

This representation is useful to efficiently calculate the Hartree functional $U_H[\rho]$ and the exchange-correlation functional $E_{\mathrm{XC}}[\rho]$ in the frequency domain. In particular the terms of the variational problem 4.11 then yield

$$T[\rho] = \sum_{\mu,\nu} P_{\mu\nu} \int \varphi_\mu(\boldsymbol{r}) \left(-\frac{1}{2}\nabla^2\right) \varphi_\nu(\boldsymbol{r}) \, \mathrm{d}^3\boldsymbol{r} \tag{4.42a}$$

$$V_{\mathrm{ext}}[\rho] = \sum_{\mu,\nu} P_{\mu\nu} \int \varphi_\mu(\boldsymbol{r}) \, v_{\mathrm{ext}}(\boldsymbol{r}) \, \varphi_\nu(\boldsymbol{r}) \, \mathrm{d}^3\boldsymbol{r} \tag{4.42b}$$

$$U_H[\rho] = 2\pi\Omega \sum_{\boldsymbol{G}} \frac{|\widetilde{\rho}(\boldsymbol{G})|^2}{|\boldsymbol{G}|^2} \ . \tag{4.42c}$$

This method is especially efficient, if the integrals in the above equations are analytic and therefore do not have to be evaluated numerically. This is intrinsically the case for Eq. 4.42a due to the use of gaussian functions. To speed up the calculation of Eq. 4.42b the pseudopotential used to describe $v_{\mathrm{ext}}(\boldsymbol{r})$ should also be expandable in a gaussian basis. [97, 101]

4.6.2 Auxiliary Density Matrix Method

Using a gaussian basis, the Hartree-Fock exchange functional can be expressed as

$$E_{\mathrm{X}}^{\mathrm{HF}}[\rho] = -\frac{1}{2} \sum_{\lambda,\sigma,\mu,\nu} P_{\mu\sigma} P_{\nu\lambda} (\mu\nu|\lambda\sigma) \tag{4.43}$$

where the abbrevation $(\mu\nu|\lambda\sigma)$ stands for

$$(\mu\nu|\lambda\sigma) \triangleq \iint \varphi_\mu(\boldsymbol{r}) \, \varphi_\nu(\boldsymbol{r}) \, g(|\boldsymbol{r}-\boldsymbol{r}'|) \, \varphi_\lambda(\boldsymbol{r}) \, \varphi_\sigma(\boldsymbol{r}) \, \mathrm{d}^3\boldsymbol{r}\mathrm{d}^3\boldsymbol{r}' \ . \tag{4.44}$$

The number of necessary computations strongly depends on the size and sparsity of the density matrix $\underline{\boldsymbol{P}}$. ADMM aims to introduce a less dense or smaller auxiliary density matrix $\underline{\hat{\boldsymbol{P}}}$, which yields approximately the same result as the original matrix $\underline{\boldsymbol{P}}$ but with much less effort. In order to construct $\underline{\hat{\boldsymbol{P}}}$, the KS orbitals are approximately expanded in an smaller auxiliary basis set

$$\hat{\psi}_i(\boldsymbol{r}) = \sum_{\mu} \hat{C}_{\mu i} \hat{\varphi}_\mu(\boldsymbol{r}) \ . \tag{4.45}$$

Die approbierte gedruckte Originalversion dieser Diplomarbeit ist an der TU Wien Bibliothek verfügbar
The approved original version of this thesis is available in print at TU Wien Bibliothek.
TU WIEN Bibliothek Your knowledge hub

The coefficients $\hat{C}_{\mu i}$ are determined by minimizing the approximation error of the KS orbitals:

$$\min_{\hat{C}_{\mu i}} \left\{ \sum_i \int \left| \psi_i(\boldsymbol{r}) - \hat{\psi}_i(\boldsymbol{r}) \right|^2 \mathrm{d}^3\boldsymbol{r} \right\} \tag{4.46}$$

The auxiliary density matrix can then be constructed with the optimized coefficients by

$$\hat{P}_{\mu\nu} \triangleq \sum_i \hat{C}_{\mu i} \hat{C}_{\nu i}\,. \tag{4.47}$$

For calculating E_X^HF with the auxiliary matrix, it is assumed, that the introduced error by this approximation is the same for the HF functional and an GGA functional:

$$E_\mathrm{X}^\mathrm{HF}[\underline{\boldsymbol{P}}] - E_\mathrm{X}^\mathrm{HF}[\underline{\hat{\boldsymbol{P}}}] \approx E_\mathrm{X}^\mathrm{GGA}[\underline{\boldsymbol{P}}] - E_\mathrm{X}^\mathrm{GGA}[\underline{\hat{\boldsymbol{P}}}]\,. \tag{4.48}$$

The approximate HF exhange is then given by

$$E_\mathrm{X}^\mathrm{HF}[\underline{\boldsymbol{P}}] \approx E_\mathrm{X}^\mathrm{HF}[\underline{\hat{\boldsymbol{P}}}] + E_\mathrm{X}^\mathrm{GGA}[\underline{\boldsymbol{P}}] - E_\mathrm{X}^\mathrm{GGA}[\underline{\hat{\boldsymbol{P}}}]\,. \tag{4.49}$$

Here the HF exhange is only calculated with the more efficient auxiliary matrix and is corrected with an GGA term, which can be computated quickly in both bases. It was demonstrated, that this approximation can outperform the standard HF exchange calculation by a factor of 20 for large systems [102].

4.7 Simulation Settings

4.7.1 Single-Point Calculations

All DFT calculations in this work were performed with the CP2K [100] software package. The evaluation of the energy $E(\boldsymbol{R})$ and the atomic forces $\boldsymbol{F} = -\nabla E$ for a given single set of nuclei positions $\boldsymbol{R}$ is the fundamental building block for all ab-initio calculations in this thesis. These so-called single-point calculations were performed with the Quickstep routine [105], which self-consistently solves the KS equations with the GPW basis set described in Sec. 4.6.1. The following settings were used throughout this work to perform single-point calculations:

i) A contracted gaussian basis set (DZVP-MOLOPT-GTH in [106]) with 2 basis functions per atomic orbital was used as the primary basis for the GPW method.

ii) The GTH-PBE pseudopotential developed by Goedecker, Teter and Hutter (GTH) [107] was used, since the primary basis is optimized to this specific potential.

iii) The used auxiliary basis for ADMM is the gaussian basis set pFIT3 in [102].

iv) The HF exchange functional PBE0 TC LRC [90] was used with a cutoff radius of $r_\mathrm{TC} = 2$Å for the truncated Coulomb operator.

These settings were already successfully used in previous works dealing with defects in amorphous SiO_2 [108, 20, 8].

Die approbierte gedruckte Originalversion dieser Diplomarbeit ist an der TU Wien Bibliothek verfügbar
The approved original version of this thesis is available in print at TU Wien Bibliothek.
TU WIEN Bibliothek Your knowledge hub

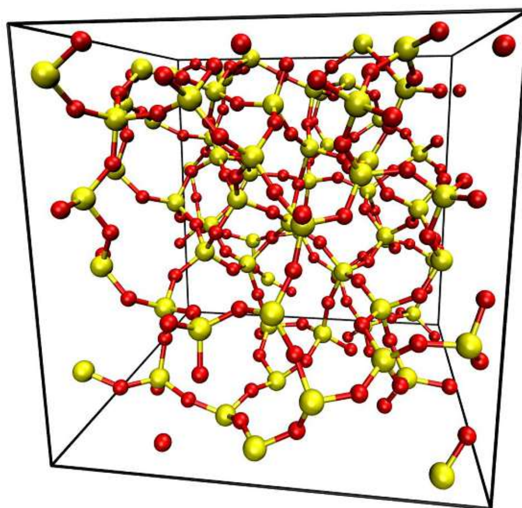

Figure 4.2: Amorphous SiO_2 structure consisting of 216 atoms within its cubic periodic simulation box with a side length of 15.095 Å.

4.7.2 Geometry Optimization

Finding stable or metastable configurations requires to find a local minimum of the potential energy surface. Starting with a reasonable initial structure $\boldsymbol{R}_0$, a gradient-based optimization algorithm is used to minimize the energy in successive single-point calculations. The Broyden-Fletcher-Goldfarb-Shanno (BFGS) [109, 110, 111, 112] algorithm was used for all geometry optimizations in this work. The optimization was stopped, when all atomic forces were smaller than 2.3meV/Å. Note that depending on the initial guess $\boldsymbol{R}_0$ different local minima can be found. For example, the states 1 and $1'$ in the 4-state model are 2 different local minima on the same potential energy surface (see Fig. 3.5).

4.7.3 Amorphous SiO_2 Structures

Ab-initio studies on the dynamics of oxide defects requires an adequate model for the oxide layer. In previous works [113] a series of amorphous SiO_2 structures were created by molecular dynamics simulations, mimicking the melting and subsequent rapid cooling of a β-cristobalite SiO_2 crystal. The calculations used the ReaxFF potential [114] and were carried out with an initial temperature of 5000 K and a cooling rate of 6 $\mathrm{K\,ps^{-1}}$. The resulting amorphous structures were than relaxed with DFT. Physical properties, e.g. density and bond lengths/angles, of the final structures were found to be in very good agreement with experimental data of actual device oxide layers. For the aim of this work, the defect types discussed in Sec. 3.5 were incorporated in these host materials. All studied structures consist of 216 atoms and are embedded in a cubic simulation box with periodic boundary conditions. One single-point DFT calculation in these structures with the settings listed above requires about $3-5$ core hours on the used VSC [115] clusters. One of the used structures is depicted in Fig. 4.2.

Die approbierte gedruckte Originalversion dieser Diplomarbeit ist an der TU Wien Bibliothek verfügbar
The approved original version of this thesis is available in print at TU Wien Bibliothek.
TU WIEN Bibliothek Your knowledge hub

Die approbierte gedruckte Originalversion dieser Diplomarbeit ist an der TU Wien Bibliothek verfügbar
The approved original version of this thesis is available in print at TU Wien Bibliothek.

CHAPTER 5 From Energies to Rates

Using the concepts of density functional theory discussed in the previous chapter, the potential energy surfaces of differently charged defect configurations can be explored pointwise. Knowledge about the system's PESs reveals the energy barriers between different states and thus determines the transition rates k_{ij} in the four-state model. This chapter discusses the link between PESs obtained by DFT and the resulting transition rates for the purely thermic transitions $1 \Leftrightarrow 1'$ and $2 \Leftrightarrow 2'$ as well as the charge transfer transitions $1 \Leftrightarrow 2'$ and $2 \Leftrightarrow 1'$. Thermic transitions are treated within classical transition state theory (TST), whereas charge transitions will be handled in the framework of nonradiative multiphonon theory (NMP). Furthermore the interplay of the defect and the valence and conduction band of the device will be described at the end of this chapter.

5.1 Thermal Transitions

When a system moves from one local minimum to another on the same PES, it has to overcome a certain thermal energy barrier. Such transitions are therefore called purely thermal. As an example, Fig. 5.1 shows the transitions $1 \Leftrightarrow 1'$ in the case of the hydroxyl-E$'$ center. The transition rates for such reactions can be calculated with classical transition state theory (TST), which was first developed by Eyring, Evans and Polanyi [116, 117] in 1935. The classical TST is built upon the following assumptions:

i) The nuclei can be described by classical mechanics, i.e. they are treated as classical particles which move on the potential energy surface.

ii) The initial state is in a thermal equilibrium, which is not disturbed by the transition event.

iii) Once the barrier is transcended, the system does not return to the initial state. Therefore trajectories which cross the barrier more than once are ruled out.

Especially the first assumption should be treated with caution when describing hydrogen related defects, since protons can have a significant tunneling probability, effectively lowering the transition barrier [118]. Although this is neglected for the scope of this

Die approbierte gedruckte Originalversion dieser Diplomarbeit ist an der TU Wien Bibliothek verfügbar
The approved original version of this thesis is available in print at TU Wien Bibliothek.
TU Wien Bibliothek Your knowledge hub

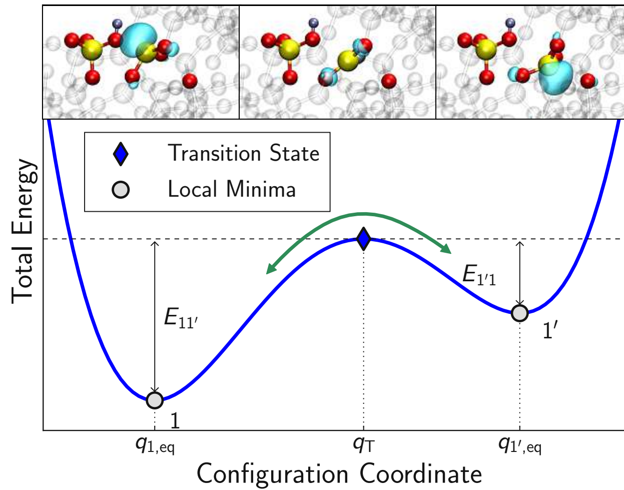

Figure 5.1: Schematic energy profile between the states $1 \Leftrightarrow 1'$ in the case of the H-E′ center. The energy barriers ($E_{11'}$ and $E_{1'1}$) of these thermal transitions are solely determined by the energy difference between the initial state and the transition state. The corresponding atomic arrangements of the defect along the configuration coordinate are depicted in the upper row. [8]

work, the impact of proton tunneling on defect dynamics should be investigated in future studies.

5.1.1 One-Dimensional Transition State Theory

For the sake of simplicity, a certain reaction path $\boldsymbol{R}(q)$ with a single reaction coordinate q is fixed. The involved PES is therefore reduced to an one-dimensional energy profile $V(q)$ as depicted in Fig. 5.1. The configuration with the highest energy along the reaction trajectory is called the transition state T. Following the derivations in [13], the transition rate from state i to j is given by the mean forward flux through the transition state T:

$$k_{ij} = \mathbb{E}[v_f]\, P(q_\mathsf{T}) \tag{5.1}$$

Here, $\mathbb{E}[v_f]$ is the mean velocity in the direction of the final state j. Under the assumption of thermal equilibrium, v_f obeys the Boltzmann-Maxwell distribution and its expectation value therefore yields[1]

$$\mathbb{E}[v_f] = \sqrt{\frac{k_\mathrm{B}T}{2\pi}}\,. \tag{5.2}$$

$P(q_\mathsf{T})\,\mathrm{d}q$ denotes the probability of the system being in the interval $[q_\mathsf{T}, q_\mathsf{T} + \mathrm{d}q]$ and is given by the Boltzmann distribution:

$$P(q_\mathrm{T}) = \frac{1}{\mathcal{Z}}\exp(-\beta E_{ij}) \quad \text{with} \quad \mathcal{Z} = \int_{-\infty}^{q_\mathsf{T}} \exp(-\beta V(q) - V(q_{i,\mathrm{eq}}))\,\mathrm{d}q \tag{5.3}$$

[1] Using mass weighted coordinates, the mass m does not appear in Eq. 5.2

Die approbierte gedruckte Originalversion dieser Diplomarbeit ist an der TU Wien Bibliothek verfügbar
The approved original version of this thesis is available in print at TU Wien Bibliothek.
TU WIEN Bibliothek Your knowledge hub

E_{ij} denotes the energy barrier, which has to be overcome to reach the final state j:

$$E_{ij} \triangleq V(q_\mathsf{T}) - V(q_{i,\mathrm{eq}}) \tag{5.4}$$

The main contribution to the partition function $\mathcal{Z}$ stems from the neighborhood of the initial local minimum $q_{i,\mathrm{eq}}$, where the energy profile can be approximated by a parabola.

$$V(q) \approx V(q_{i,\mathrm{eq}}) + \frac{1}{2}\omega_0^2 (q - q_{i,\mathrm{eq}})^2 \tag{5.5}$$

Using this approximation, $\mathcal{Z}$ can be expressed as

$$\mathcal{Z} \approx \int_{-\infty}^{q_\mathsf{T}} \exp\left(-\frac{\beta}{2}\omega_0^2 (q - q_{i,\mathrm{eq}})^2\right) \mathrm{d}q \approx \int_{-\infty}^{\infty} \exp\left(-\frac{\beta}{2}\omega_0^2 q^2\right) \mathrm{d}q = \frac{1}{\omega_0}\sqrt{2\pi k_\mathrm{B} T}\,. \tag{5.6}$$

Putting everything together, Eq. 5.1 finally yields the transition rate

$$k_{ij} \approx \nu_0 \exp(-\beta E_{ij}) \quad \text{with} \quad \nu_0 \triangleq \frac{\omega_0}{2\pi}\,. \tag{5.7}$$

The prefactor ν_0 is usually referred to as attempt frequency. Physically, this factor can be interpreted as the number of attempts per unit time to overcome the thermal barrier. As can be seen in Eq. 5.7, the derived transition rate is determined by the thermal barrier E_{ij} and obeys the empirical Arrhenius law Eq. 3.20.

5.1.2 General Harmonic Transition State Theory

Eq. 5.7 describes the transition rate in the case of a fixed reaction path. In reality, however, the system can potentially take any path from the initial state to the final state. Due to the exponential dependence on the barrier height E_{ij}, the path with the lowest possible barrier between the two states, the so-called minimum energy path (MEP), determines the overall transition rate. The transition state along the MEP is always a first-order saddle point of the PES with a single negative curvature in the direction of the MEP [116]. In the vicinity of the transition state the PES can therefore be approximated by

$$V(\boldsymbol{q}) = V(\boldsymbol{q}_\mathsf{T}) - \frac{1}{2}\omega_{\mathsf{T}0}^2 (q_1 - q_{\mathsf{T}1})^2 + \frac{1}{2}\sum_{k=2}^{3N} \omega_{\mathsf{T}k}^2 (q_k - q_{\mathsf{T}k})^2\,. \tag{5.8}$$

Here q_1 denotes the configuration coordinate along the MEP. Similarly the PES near the initial local minimum $\boldsymbol{q}_\mathsf{M}$ can be approximated by a paraboloid

$$V(\boldsymbol{q}) = V(\boldsymbol{q}_\mathsf{M}) + \frac{1}{2}\sum_{k=1}^{3N} \omega_{\mathsf{M}k}^2 (q_k - q_{\mathsf{M}k})^2\,. \tag{5.9}$$

Die approbierte gedruckte Originalversion dieser Diplomarbeit ist an der TU Wien Bibliothek verfügbar
The approved original version of this thesis is available in print at TU Wien Bibliothek.
TU WIEN Bibliothek Your knowledge hub

With these approximations, the general multi-dimensional TST then yields the transition rate [119, 13]

$$k_{ij} = \nu \exp\left(-\beta E_{ij}\right) \quad \text{with} \quad \nu \triangleq \frac{1}{2\pi} \frac{\prod_{k=1}^{3N} \omega_{\mathsf{M}k}}{\prod_{k=2}^{3N} \omega_{\mathsf{T}k}} \,. \tag{5.10}$$

The attempt frequency in the multidimensional TST is often assumpted to be in the order of $\nu \approx 10^{13}$ Hz [4, 120, 121].

Although the calculation of transition rates within TST is trivial once the MEP is known, finding the MEP between two local minima of a PES is computationally very expensive and requires special methods. One of the most popular methods to determine MEPs, the nudged elastic band algorithm, will be discussed in the following section.

5.2 Transition State Optimization

Since the MEP, per definition, leads across a saddle point of the PES, it seems natural to first search for such a saddle point. Several schemes have been developed to perform this task [122, 123]. Usually these algorithms start in one of the local minima and follow a path of slowest ascent. However, this search strategy does not necessarily lead to the desired transition state. Other algorithms [124] perform a normal mode analysis to determine a search direction for the transition state. Those methods require the calculation of the Hessian matrix, which is very expensive and thus impractical for larger systems. Due to these downsides, searching for the MEP is commonly done with so-called chain-of-state (COS) approaches.

5.2.1 Plain Elastic Band

The basic idea of COS methods is to create a chain of equidistant intermediate configurations (referred to as images or replica) between the initial and final state. The total energy of this chain of states is then minimized with local optimization algorithms. The simplest COS method, known as plain elastic band (PEB) [125], connects neighboring images with virtual springs to maintain the initial equidistant separation of the images. This results in an objective function

$$S^{\mathrm{PEB}}\left(\boldsymbol{R}_1, \boldsymbol{R}_2, \ldots, \boldsymbol{R}_{N-1}\right) \triangleq \sum_{i=1}^{N-1} V\left(\boldsymbol{R}_i\right) + \frac{1}{2} \sum_{i=1}^{N-1} k\left(\boldsymbol{R}_i - \boldsymbol{R}_{i-1}\right)^2 \,, \tag{5.11}$$

which is then optimized for the images with coordinates $\boldsymbol{R}_1, \ldots, \boldsymbol{R}_{N-1}$. The force acting on each image is then given by

$$\boldsymbol{F}_i^{\mathrm{PEB}} = -\nabla_i S^{\mathrm{PEB}} = \boldsymbol{F}_i^e + \boldsymbol{F}_i^s \,, \tag{5.12}$$

where $\boldsymbol{F}_i^e$ is the physical force induced by the potential energy gradient

$$\boldsymbol{F}_i^e \triangleq -\nabla V \,|_{\boldsymbol{R}_i} \tag{5.13}$$

Die approbierte gedruckte Originalversion dieser Diplomarbeit ist an der TU Wien Bibliothek verfügbar
The approved original version of this thesis is available in print at TU Wien Bibliothek.
TU WIEN Bibliothek Your knowledge hub

and $\boldsymbol{F}_i^s$ denotes the virtual spring force acting on image i

$$\boldsymbol{F}_i^s \triangleq k\left(\boldsymbol{R}_{i+1} - \boldsymbol{R}_i\right) - k\left(\boldsymbol{R}_i - \boldsymbol{R}_{i-1}\right) . \tag{5.14}$$

The endpoints of the chain , denoted by $\boldsymbol{R}_0$ and $\boldsymbol{R}_N$, are not impacted by the virtual spring forces and are either fixed or are driven towards the local minimum positions. The PEB method is simple and straightforward, however, it often fails to converge to the MEP. This is due to the reason that the chain-of-states behaves like a rubber band and tries to minimize its length, leading to shortcuts and therefore missing of the saddle point. Furthermore, the PEB images tend to slide down the PES and thus avoid the transition state region.

5.2.2 Nudged Elastic Band

The drawbacks of the PEB method can be overcome with a slight modification, known as nudged elastic band [126]. The forces $\boldsymbol{F}_i$ on the images of the PEB method can be seperated in components parallel and perpendicular to the reaction path:

$$\boldsymbol{F}_i^{\parallel} = \left(\boldsymbol{F}_i \cdot \hat{\tau}_i\right)\hat{\tau}_i \qquad \boldsymbol{F}_i^{\perp} = \boldsymbol{F}_i - \boldsymbol{F}_i^{\parallel} \tag{5.15}$$

Here $\hat{\tau}_i$ is the unity tangent vector to the reaction path at the image i. The tendency of the PEB method to take shortcuts is caused by $\boldsymbol{F}_i^{s\perp}$, whereas $\boldsymbol{F}_i^{e\parallel}$ is responsible for the sliding down of images. Therefore the NEB method removes these two components, resulting in the image force

$$\boldsymbol{F}_i^{\mathrm{NEB}} \triangleq \boldsymbol{F}_i^{e\perp} + \boldsymbol{F}_i^{s\parallel} . \tag{5.16}$$

If a sufficient number of intermediate images are used, this modification allows the chain to converge towards the true MEP as depicted in Fig. 5.2. Furthermore, since the spring forces act only along the reaction path, the exact value for the spring constant k is not critical. The MEP is not known in advance, therefore the tangent unit vector $\hat{\tau}_i$ needs to be approximated. In the original NEB implementation [126] the approximation

$$\hat{\tau}_i = \frac{\boldsymbol{R}_{i+1} - \boldsymbol{R}_{i-1}}{\left|\boldsymbol{R}_{i+1} - \boldsymbol{R}_{i-1}\right|} \tag{5.17}$$

is used. This scheme sometimes introduces convergence instabilities, which can be resolved by the improved tangent nudged elastic band (IT-NEB) [127].

Although this work does not directly deal with purely thermal transitions, the NEB method will be used to construct MEPs between 2 different PESs to describe charge transitions in Ch. 6.

5.2.3 Climbing Image NEB

As demonstrated in Fig. 5.2, the equidistant spacing of the NEB images generally results in an underestimation of the transition barrier, since no image lies exactly at

Die approbierte gedruckte Originalversion dieser Diplomarbeit ist an der TU Wien Bibliothek verfügbar
The approved original version of this thesis is available in print at TU Wien Bibliothek.
TU WIEN Bibliothek Your knowledge hub

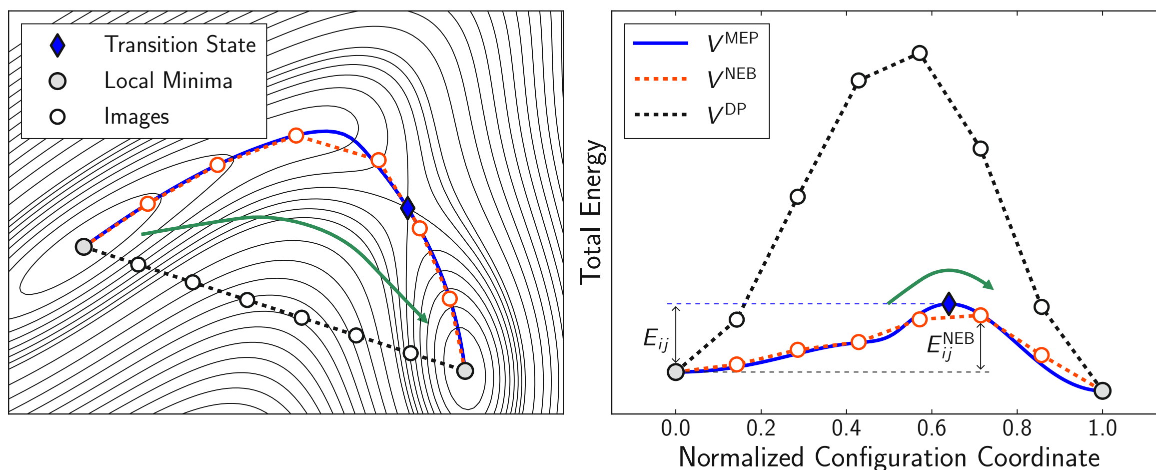

Figure 5.2: **Left:** Results of a NEB calculation on a two-dimensional analytic PES. Initially the images are placed along the direct path (black) between the two minima. The chain-of-states converges to to the true analytic MEP (red). **Right:** Comparison of resulting energy profiles along the initial direct path, the converged NEB path and the true MEP. In general, the direct path always overestimates the thermal barrier. Due to the equidistant spacing of the images, the true saddle point is missed by the NEB path, leading to an underestimation of the barrier in general. This disadvanting is removed by using the Climbing-Image NEB.

Die approbierte gedruckte Originalversion dieser Diplomarbeit ist an der TU Wien Bibliothek verfügbar
The approved original version of this thesis is available in print at TU Wien Bibliothek.
TU WIEN Bibliothek Your knowledge hub

the transition state. The climbing image (CI) NEB [128] allows the image $i_{\max}$ with the highest energy to converge ("climb") towards the saddle point. To achieve this, the force acting on this so-called climbing image is replaced with

$$\boldsymbol{F}_{i_{\max}} = \boldsymbol{F}^{e}_{i_{\max}} - 2\hat{\tau}_{i_{\max}} \left(\hat{\tau}_{i_{\max}} \cdot \boldsymbol{F}^{e}_{i_{\max}} \right) . \tag{5.18}$$

The climbing image is not subject to the forces of the virtual springs. Instead, the force on the CI is determined solely by the gradient of the PES, but the force component parallel to the reaction path is reversed in order to drive this image upwards to the saddle point. Thus the CI-NEB method allows a accurate calculation of the MEP.

5.3 Nonradiative Multiphonon Transitions

Contrary to purely thermal transitions, the charge transitions $1 \Leftrightarrow 2'$ and $2 \Leftrightarrow 1'$ involve a change of the electronic state and therefore the initial and final states lie on different PESs. As depicted in Fig. 5.3, one can distinguish between radiative transitions and non-radiative transitions [129]. Radiative transitions require the absorbtion or emission of photons. During a radiative transition, the geometry of the system is initially conserved and subsequently relaxes to a minimum of the new PES. On the other hand, nonradiative transitions are phonon-assisted and are associated with a geometry change during the transition. These transitions preferentially occur near the intersection point of the involved PESs. This work focuses entirely on nonradiative multiphonon (NMP) transitions, since in this case, significantly lower barriers have to be overcome. Furthermore at typical BTI conditions with elevated temperatures, nonradiative transitions are the primary cause of charge capture and emission events.

5.3.1 Single State Transitions

NMP transitions involve an ensemble of vibrational modes both in the initial state and the final state. For simplicity, we first consider a simple transition from a specific initial state $|\Psi_i \otimes \eta_{i\alpha}\rangle$ to a final state $|\Psi_j \otimes \eta_{j\beta}\rangle$. Within a first-order perturbation approach the transition rate $k_{i\alpha j\beta}$ is then given by Fermi's Golden Rule [130, 131]:

$$k_{i\alpha j\beta} = \frac{2\pi}{\hbar} \left| M_{i\alpha j\beta} \right|^2 \delta \left(E_{j\beta} - E_{i\alpha} \right) \tag{5.19}$$

Here, the matrix element $M_{i\alpha j\beta}$ is given by

$$M_{i\alpha j\beta} \triangleq \langle \Psi_i \otimes \eta_{i\alpha} | \hat{H}' | \Psi_j \otimes \eta_{j\beta} \rangle \ , \tag{5.20}$$

with the perturbation operator $\hat{H}'$. According to Eq. 5.19, a transition $i\alpha \Rightarrow j\beta$ can only occur, when the energy levels of the initial and final state coincide, thus the total energy is conserved during the transition. Within the Born-Oppenheimer approximation, the perturbation operator can be split in an electronic and a vibronic component:

$$\hat{H}' = \hat{H}'_{\text{el}} + \hat{H}'_{\text{vib}} \tag{5.21}$$

TU Bibliothek WIEN Your knowledge hub
Die approbierte gedruckte Originalversion dieser Diplomarbeit ist an der TU Wien Bibliothek verfügbar
The approved original version of this thesis is available in print at TU Wien Bibliothek.

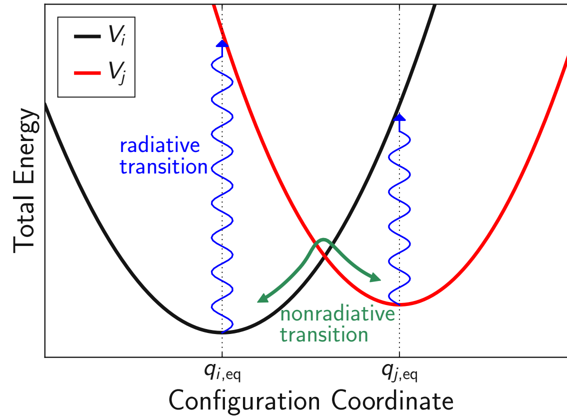

Figure 5.3: Schematic charge transition between the neutral (V_0) and the positive (V_+) charge state. Absorbtion or emission of photons lead to a radiative (optical) transition where the geometry is conserved during transition. Nonradiative transitions are phonon-assisted and are assumed to occur near the crossing point of the PESs. Nonradiative transitions therefore have lower barriers compared to radiative transitions and are the dominant cause of charge transitions associated with the BTI phenomenon. [8]

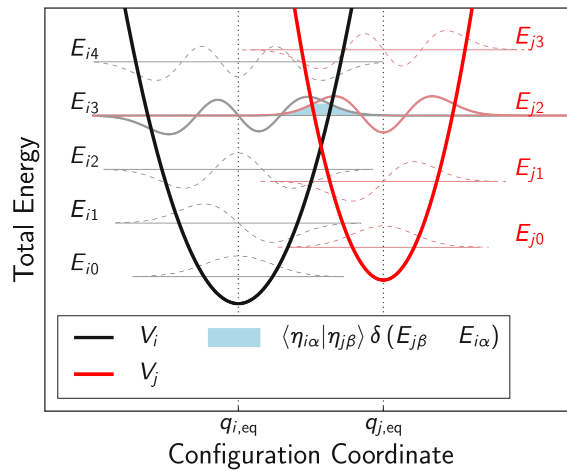

Figure 5.4: Potential energy profiles of two differently charged defect states. The corresponding vibronic modes are represented by the dashed lines. According to the Franck-Condon principle, the rate for a transition $i\alpha \Rightarrow j\beta$ is proportional to the overlap integral of the corresponding wavefunctions $|\eta_{i\alpha}\rangle$ and $|\eta_{j\beta}\rangle$. Furthermore, Fermi's golden rule demands the conservation of energy during charge transitions. Therefore only vibronic modes with coinciding eigenenergies $E_{i\alpha} = E_{j\beta}$ can contribute to a charge transition. This is the case for the thick drawn modes, for which the overlap is depicted as the blue area. [4]

Die approbierte gedruckte Originalversion dieser Diplomarbeit ist an der TU Wien Bibliothek verfügbar
The approved original version of this thesis is available in print at TU Wien Bibliothek.
TU WIEN Bibliothek Your knowledge hub

Then the matrix element $M_{i\alpha j\beta}$ can be expressed as

$$\begin{aligned} M_{i\alpha j\beta} &= \langle \Psi_i \otimes \eta_{i\alpha} | \hat{H}'_{\text{el}} + \hat{H}'_{\text{vib}} | \Psi_j \otimes \eta_{j\beta} \rangle = \\ &= \langle \eta_{i\alpha} | \eta_{j\beta} \rangle \langle \Psi_i | \hat{H}'_{\text{el}} | \Psi_j \rangle + \underbrace{\langle \Psi_i | \Psi_j \rangle}_{=0} \langle \eta_{i\alpha} | \hat{H}'_{\text{vib}} | \eta_{j\beta} \rangle = \\ &= \langle \eta_{i\alpha} | \eta_{j\beta} \rangle \langle \Psi_i | \hat{H}'_{\text{el}} | \Psi_j \rangle \ . \end{aligned} \tag{5.22}$$

The second term vanishes due to the orthogonality of different electronic states. The matrix element therefore is a product of an electronic matrix element and the overlap integral (see Fig. 5.4) of the initial and final vibronic wavefunctions. This simplification is commonly known as Franck-Condon principle [132, 133, 129, 134].

5.3.2 NMP Transitions in a Canonical Ensemble

Under typical operating temperatures, many different vibrational modes are excited for one electronic state. All these modes therefore can contribute to the overall charge transition rate. Assuming the initial state is in thermal equilibrium, the total transition rate k_{ij} is determined by the thermal average of all partial rates $k_{i\alpha j\beta}$ across the canonical ensemble of the initial state [12, 135, 54]. With the abbrevations

$$\underset{\alpha}{\text{ave}}\left(x_\alpha\right) \triangleq \frac{1}{\mathcal{Z}} \sum_\alpha x_\alpha \exp\left(-\beta E_{i\alpha}\right), \quad \mathcal{Z} = \sum_\alpha \exp\left(-\beta E_{i\alpha}\right) \tag{5.23}$$

the total transition rate is given by

$$k_{ij} = \underset{\alpha}{\text{ave}}\Big(\sum_\beta k_{i\alpha j\beta}\Big) \ . \tag{5.24}$$

Usually, the rate k_{ij} is expressed as the product of an electronic matrix element A_{ij} and a so-called lineshape function f_{ij}, describing the vibronic interactions:

$$k_{ij} = A_{ij} f_{ij} \tag{5.25}$$

$$A_{ij} \triangleq \frac{2\pi}{\hbar} \left| \langle \Psi_i | \hat{H}'_{\text{el}} | \Psi_j \rangle \right|^2 \tag{5.26}$$

$$f_{ij} \triangleq \underset{\alpha}{\text{ave}}\Big(\sum_\beta \left|\langle \eta_{i\alpha} | \eta_{j\beta} \rangle\right|^2 \delta\left(E_{j\beta} - E_{i\alpha}\right)\Big) \tag{5.27}$$

In the case of charge transitions between the defect and the oxide, the matrix elements A_{ij} describe the interaction between the electronic wavefunctions of the defect and the channel of a MOSFET, for example. It is possible to simulate a whole Si/SiO_2 interface structure within DFT in order to get both of these wavefunctions directly. However, such calculations require a large simulation cell and are computationally demanding [136]. Since in this work, we analyze many defects in different amorphous structures, such an approach would not be feasible. Instead, the defects are simulated in a bulk oxide, therefore the channel wavefunctions are not accessable and the matrix elements A_{ij} must be approximated. Since the defect wavefunctions are strongly localized, it is reasonable to approximate A_{ij} by a simple tunneling factor [54], see Sec. 5.4.2 for more details.

Die approbierte gedruckte Originalversion dieser Diplomarbeit ist an der TU Wien Bibliothek verfügbar
The approved original version of this thesis is available in print at TU Wien Bibliothek.
TU WIEN Bibliothek Your knowledge hub

5.3.3 Classical Lineshape Function

In a solid material like SiO_2 the energy difference $\Delta E_{i\alpha}$ between consecutive vibrational modes is usually smaller than $k_B T$ at room temperature and the eigenenergies $E_{i\alpha}$ can be assumed to form a continuum. Therefore, in the case of oxide defects, the lineshape function can be represented by an integral over the energy continuum of the initial state:

$$f_{ij} = \frac{1}{\mathcal{Z}} \int_q g\left(V_i\left(q'\right)\right) \exp\left(-\beta V_i\left(q'\right)\right) \mathrm{d}q', \quad \mathcal{Z} = \int_q \exp\left(-\beta V_i\left(q\right)\right) \mathrm{d}q' \tag{5.28}$$

Here $g\left(V_i\right)$ denotes a density function and accounts for the vibrational overlaps at the energy level V_i. As shown in Fig. 5.5, the main contribution to the overall lineshape function is near the crossing point of the involved PESs at the energy $V_i = V_j = V_{\mathrm{CP}}$. This allows to approximate the overlap density function with a Dirac peak at the crossing point in the classical limit

$$\Delta E_{i\alpha} < k_B T \ll E_{ij} \triangleq V_{\mathrm{CP}} - V_{i,\min}. \tag{5.29}$$

It is therefore assumed, that the transition occurs exactly at the crossing point. Within this approximation, the lineshape function becomes [4]

$$\begin{aligned} f_{ij} &\approx \frac{1}{\mathcal{Z}} \int_q \delta\left(V_j\left(q'\right) - V_i\left(q'\right)\right) \exp\left(-\beta V_i\left(q'\right)\right) \mathrm{d}q' = \\ &= \frac{1}{\mathcal{Z} |V_j'\left(q_{\mathrm{CP}}\right) - V_i'\left(q_{\mathrm{CP}}\right)|} \exp\left(-\beta V_{\mathrm{CP}}\right). \end{aligned} \tag{5.30}$$

Factoring out $\exp\left(-\beta V_{i,\min}\right)$ from the partition function $\mathcal{Z}$ finally results in

$$f_{ij} = \gamma_{ij} \exp\left(-\beta\left(V_{\mathrm{CP}} - V_{i,\min}\right)\right) = \gamma_{ij} \exp\left(-\beta E_{ij}\right). \tag{5.31}$$

Here γ_{ij} denotes a prefactor, which depends on the shape of the PESs. Similar to the thermal transitions discussed previously, NMP transition rates are determined by an energy barrier E_{ij} in the classical limit. In this case, the energy barrier is given by the difference between the crossing point energy V_{CP} and the minimum energy $V_{i,\min}$ in the initial state. Note that the prefactor γ_{ij} will be omitted, since the lineshape function is dominated by the exponential term in Eq. 5.31.

This approximation allows for a simple analytic model for NMP transitions and is therefore used throughout this work. Although the classical lineshape function neglects tunneling effects, it is in good agreement with its quantum mechanical counterpart Eq. 5.27 for oxide defects at room temperature and above [54].

5.4 NMP Transitions in Oxide Defects

Defects in the oxide layer of a MOSFET cannot be treated as an isolated system, since they capture (emit) charges from (to) the valence or conduction band of the device

Die approbierte gedruckte Originalversion dieser Diplomarbeit ist an der TU Wien Bibliothek verfügbar
The approved original version of this thesis is available in print at TU Wien Bibliothek.
TU WIEN Bibliothek Your knowledge hub

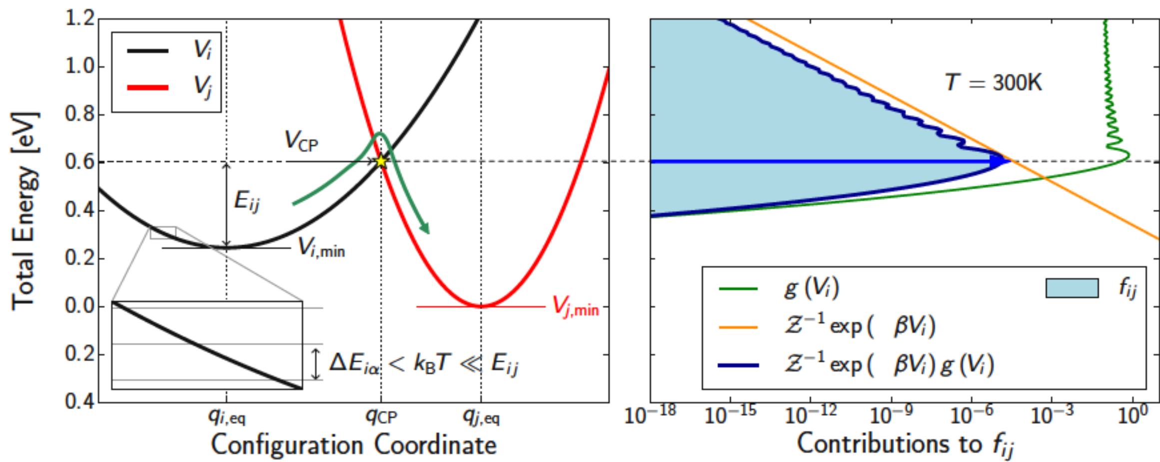

Figure 5.5: Classical limit of NMP transitions in oxide defects. **Left:** Schematic configuration diagram of a typical NMP transition in SiO_2. The spacing between the vibrational eigenenergies of the electronic states are very small compared to the barrier E_{ij} (see inset). **Right:** Contributions to the total LSF depending on V_i. The overlap density $g(V_i)$ rapidly decays below the crossing point energy V_{CP} because the corresponding wavefunctions are too far seperated to have a significant overlap. Weighted with the occupation probability of the canonical ensemble (orange line) this leads to a sharp peak at V_{CP}. The blue arrow represents the Dirac peak in the classical limit.

Die approbierte gedruckte Originalversion dieser Diplomarbeit ist an der TU Wien Bibliothek verfügbar
The approved original version of this thesis is available in print at TU Wien Bibliothek.
TU Bibliothek WIEN Your knowledge hub

substrate. Furthermore they interact with the electric field in the oxide, causing a bias dependence of the charge capture and emission times. In this section, NMP transition theory is adopted to describe the charge transitions responsible for BTI in a MOSFET. In the following derivations we consider a so-called hole trap, i.e a defect which primarily interacts with the valence band and can be either in a neutral (0) or a positive (+) charge state. Throughout this section the energy minimum of the positive defect PES is chosen to be

$$V_{+,\min} \triangleq 0\,. \tag{5.32}$$

Note that this is completely arbitrary and does not influence the physical results, since only energy differences are important. However, this reference is convenient to explain the interplay between an hole trap and the energy bands of the channel.

5.4.1 Charge Exchange with the Substrate Reservoir

The device substrate with its continous valence and conduction band acts as a charge reservoir for oxide defects. When the hole trap is in its neutral state, the total energy of the system can be expressed as

$$\widetilde{V}_0\,(q) \triangleq V_0\,(q) + V_{0,\mathrm{res}}\,, \tag{5.33}$$

where V_0 denotes the PES of the defect in its neutral state and $V_{0,\mathrm{res}}$ is the energy of all charge carriers in the substrate reservoir. The trap can switch to the positive charge state, by emitting an electron with energy E into the reservoir. The total energy is then given by

$$\widetilde{V}_+\,(q) \triangleq V_+\,(q) + V_{+,\mathrm{res}} \quad \text{with} \quad V_{+,\mathrm{res}} = V_{0,\mathrm{res}} + E\,. \tag{5.34}$$

Since the electron is injected into the substrate, its energy is increased by E. Here it is assumed, that the other carriers in the reservoir are not affected by this transition. Since NMP transitions only depend on energy differences but not total energies, $V_{0,\mathrm{res}}$ can be omitted, resulting in the effective defect PESs

$$\widetilde{V}_0\,(q) \triangleq V_0\,(q) \quad \text{and} \quad \widetilde{V}_+\,(q) \triangleq V_+\,(q) + E\,. \tag{5.35}$$

Therefore every reservoir state E is associated with a shifted positive PES as depicted in Fig. 5.6. To describe the energetic position of the neutral defect state relative to the energy bands, it is convenient to introduce the so-called trap level[2]

$$E_\mathrm{T} \triangleq V_{0,\min} - E_\mathrm{V}\,. \tag{5.36}$$

The transition rates then become dependent on the energy E of the involved reservoir state and the trap-level E_T:

$$k_{ij}(E, E_\mathrm{T}) = A_{ij}\,(E, E_\mathrm{T})\, f_{ij}\,(E, E_\mathrm{T}) \tag{5.37}$$

[2]For defects which interact mostly with the conduction band, $E_\mathrm{T} \triangleq E_\mathrm{C} - V_{0,\min}$ might be used instead.

Die approbierte gedruckte Originalversion dieser Diplomarbeit ist an der TU Wien Bibliothek verfügbar
The approved original version of this thesis is available in print at TU Wien Bibliothek.
TU Bibliothek WIEN Your knowledge hub

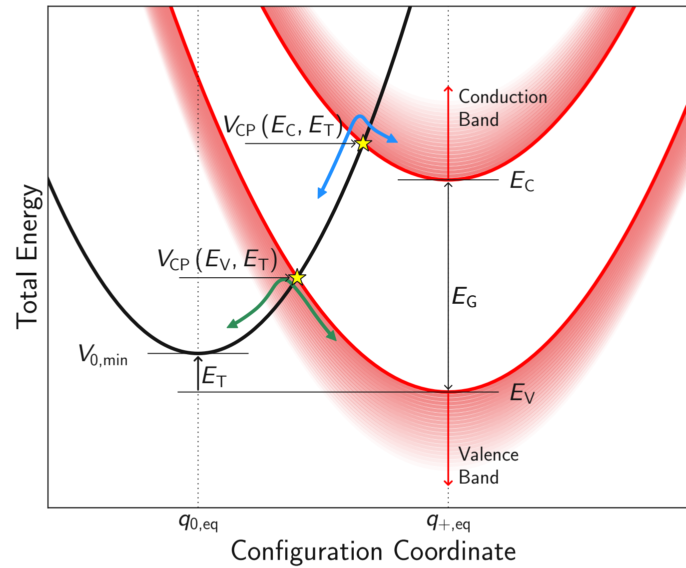

Figure 5.6: Defect PESs when interacting with the reservoirs in the channel. The positive PES (red) is shifted by the carrier energy E of the involved reservoir state. This leads to two bands of energy surfaces, since the defect can in principle interact with every state in the reservoir. The green arrows represent the hole exchange with the valence band, the blue arrows indicate the exchange of electrons with the conduction band. The relative position of the neutral defect state to one of the band edges (E_V, E_C) is called the thermodynamical trap level E_T. In this work hole traps in pMOS devices are investigated, therefore the reference is always E_V. [4]

Die approbierte gedruckte Originalversion dieser Diplomarbeit ist an der TU Wien Bibliothek verfügbar
The approved original version of this thesis is available in print at TU Wien Bibliothek.
TU Bibliothek WIEN Your knowledge hub

Summation over all reservoir states in the valence and conduction band then yield the total transition rates [34, 4]

$$k_{0+}^{\mathrm{V}}(E_{\mathrm{T}}) = \int_{-\infty}^{E_{\mathrm{V}}} D_p(E)\, f_p(E)\, A_{0+}(E, E_{\mathrm{T}})\, f_{0+}(E, E_{\mathrm{T}})\, \mathrm{d}E \tag{5.38a}$$

$$k_{+0}^{\mathrm{V}}(E_{\mathrm{T}}) = \int_{-\infty}^{E_{\mathrm{V}}} D_p(E)\, f_n(E)\, A_{+0}(E, E_{\mathrm{T}})\, f_{+0}(E, E_{\mathrm{T}})\, \mathrm{d}E \tag{5.38b}$$

$$k_{0+}^{\mathrm{C}}(E_{\mathrm{T}}) = \int_{E_{\mathrm{C}}}^{\infty} D_n(E)\, f_p(E)\, A_{0+}(E, E_{\mathrm{T}})\, f_{0+}(E, E_{\mathrm{T}})\, \mathrm{d}E \tag{5.38c}$$

$$k_{+0}^{\mathrm{C}}(E_{\mathrm{T}}) = \int_{E_{\mathrm{C}}}^{\infty} D_n(E)\, f_n(E)\, A_{+0}(E, E_{\mathrm{T}})\, f_{+0}(E, E_{\mathrm{T}})\, \mathrm{d}E\,. \tag{5.38d}$$

Here D_p and D_n denote the density of states in the valence and conduction band respectively. Since a transition $0 \Rightarrow +$ requires the target reservoir state to be empty, the integrands must be weighted with the hole occupation probability $f_p(E)$. Similarly the contributions to a transition $+ \Rightarrow 0$ are weighted with the electron occupation probability $f_n(E)$ since the initial reservoir state must be filled. The charge carriers are fermions, therefore their occupation probabilities are given by the Fermi-Dirac statistic

$$f_n(E) = \frac{1}{1 + \exp(\beta(E - E_F))} \tag{5.39a}$$

$$f_p(E) = \frac{1}{1 + \exp(\beta(E_F - E))} \tag{5.39b}$$

with the Fermi level E_F.

5.4.2 Band Edge Approximation

In a semiconductor the carriers are concentrated near the band edges E_V and E_C. In a first-order approximation it can therefore be assumed, that the matrix element A_{ij} and the lineshape function f_{ij} in Eq. 5.38 only depend on the band edges and can be factored out from the integral [137]. In the case of transitions to the valence band this yields

$$k_{0+}^{\mathrm{V}}(E_{\mathrm{T}}) = A_{0+}(E_{\mathrm{V}}, E_{\mathrm{T}})\, f_{0+}(E_{\mathrm{V}}, E_{\mathrm{T}}) \int_{-\infty}^{E_{\mathrm{V}}} D_p(E)\, f_p(E)\, \mathrm{d}E \tag{5.40a}$$

$$k_{+0}^{\mathrm{V}}(E_{\mathrm{T}}) = A_{+0}(E_{\mathrm{V}}, E_{\mathrm{T}})\, f_{+0}(E_{\mathrm{V}}, E_{\mathrm{T}}) \int_{-\infty}^{E_{\mathrm{V}}} D_p(E)\, f_n(E)\, \mathrm{d}E\,. \tag{5.40b}$$

Using the relation

$$f_n(E) = \exp(\beta(E - E_{\mathrm{F}}))\, f_p(E) \tag{5.41}$$

and the definition of the hole concentration

$$p = \int_{-\infty}^{E_{\mathrm{V}}} D_p(E)\, f_p(E) \tag{5.42}$$

Die approbierte gedruckte Originalversion dieser Diplomarbeit ist an der TU Wien Bibliothek verfügbar
The approved original version of this thesis is available in print at TU Wien Bibliothek.
TU WIEN Bibliothek Your knowledge hub

the rates to the valence band can be expressed as

$$k_{0+}^{\mathrm{V}}(E_{\mathrm{T}}) = pA_{0+}(E_{\mathrm{V}}, E_{\mathrm{T}})\, f_{0+}(E_{\mathrm{V}}, E_{\mathrm{T}}) \tag{5.43}$$

$$k_{+0}^{\mathrm{V}}(E_{\mathrm{T}}) = pA_{+0}(E_{\mathrm{V}}, E_{\mathrm{T}})\, f_{+0}(E_{\mathrm{V}}, E_{\mathrm{T}}) \exp\left(\beta\left(E_{\mathrm{V}} - E_{\mathrm{F}}\right)\right) . \tag{5.44}$$

Matrix Elements

In a crude approximation, the unknown matrix elements A_{ij} can be assumed to be of the form [10]

$$A_{0+}(E_{\mathrm{V}}, E_{\mathrm{T}}) = A_{+0}(E_{\mathrm{V}}, E_{\mathrm{T}}) = v_{\mathrm{th},p}\sigma_p\vartheta\, . \tag{5.45}$$

Here $v_{\mathrm{th},p} = \sqrt{8k_{\mathrm{B}}T/\left(\pi m_p^*\right)}$ denotes the thermal hole velocity. $\sigma_p = 3.0 \times 10^{-14}\mathrm{cm}^2$ is the hole capture cross section [138]. The WKB tunneling factor ϑ is given by [47]

$$\vartheta = \exp\left(-x_{\mathrm{t}}/x_0\right) , \tag{5.46}$$

where x_{t} is the distance of the defect to the interface and x_0 is an effective tunneling length.

Transition Rates

All these approximations together with the classical limit of the lineshape function finally yield the transition rates

$$\frac{1}{\tau_{\mathrm{c}}} = k_{0+}^{\mathrm{V}}(E_{\mathrm{T}}) = pv_{\mathrm{th},p}\sigma_p\vartheta \exp\left(-\beta E_{\mathrm{B,c}}\right) \tag{5.47a}$$

$$\frac{1}{\tau_{\mathrm{e}}} = k_{+0}^{\mathrm{V}}(E_{\mathrm{T}}) = pv_{\mathrm{th},p}\sigma_p\vartheta \exp\left(-\beta\left(E_{\mathrm{B,e}} - E_{\mathrm{F}}\right)\right) \tag{5.47b}$$

with the barriers

$$E_{\mathrm{B,c}} = V_{\mathrm{CP}}(E_{\mathrm{V}}, E_{\mathrm{T}}) - E_{\mathrm{T}} \tag{5.48a}$$

$$E_{\mathrm{B,e}} = V_{\mathrm{CP}}(E_{\mathrm{V}}, E_{\mathrm{T}}) \tag{5.48b}$$

Since all studies in this work are conducted for hole traps in pMOS transisors, the valence band edge was used as energy reference ($E_{\mathrm{V}} = 0$) to simplify the equations. Here $E_{\mathrm{B,c}}$ stands for the barrier to capture a hole from the valence band ($0 \Rightarrow +$). Similarly, $E_{\mathrm{B,e}}$ is the barrier for hole emission ($+ \Rightarrow 0$). This simple model links the results of the DFT calculations to the rate equations discussed earlier in Ch. 3. We will use this model in Ch. 7 to evaluate the influence of different PES approximations on transition times in a test device. Although not needed in this work, it should be mentioned, that similar equations can also be derived for electron traps. The full set of equations can be found in [34, 139, 137].

Die approbierte gedruckte Originalversion dieser Diplomarbeit ist an der TU Wien Bibliothek verfügbar
The approved original version of this thesis is available in print at TU Wien Bibliothek.
TU WIEN Bibliothek Your knowledge hub

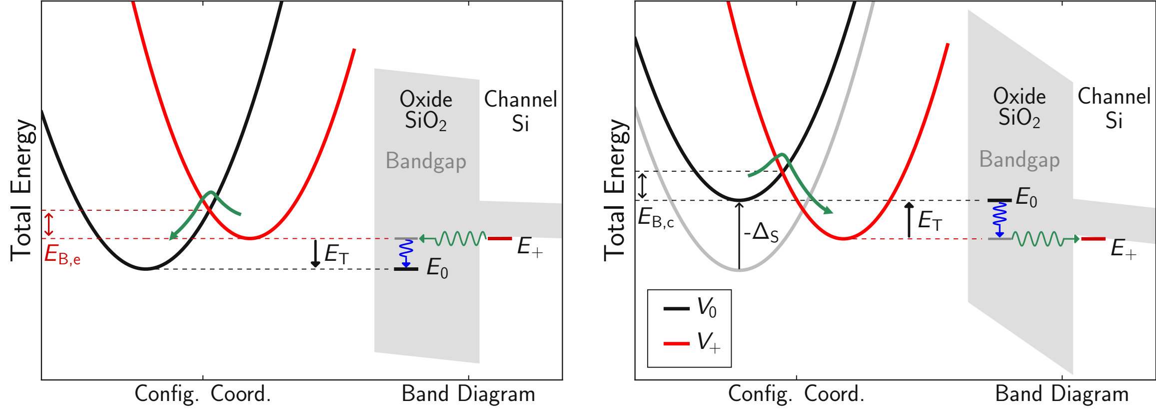

Figure 5.7: Impact of the oxide field on a hole trap in a pMOS. **Left:** When a low gate voltage is applied, the trap-level is below the Fermi-level and therefore the neutral state is thermodynamically more stable. The defect tends to emit its trapped hole. **Right:** Applying a large electric field shifts the trap-level above the Fermi-level. It becomes favourable to capture a hole. This is the typical situation under NBTI stress. [8]

5.4.3 Interaction with the Oxide Field

The energy of the electron in an neutral hole trap does not only depend on the defect itself, but also on the electric potential inside the oxide. It is assumed that an applied electric field does not interact with the defect, beside a shift of the energy position. Therefore possible interaction with dipole moments of the defect, which could alter the PESs, are neglected. In a first-order approach, the additional energy due to the oxide field F_{ox} is given by the simply expression [7]

$$\Delta_{\mathrm{S}} \triangleq Q x_{\mathrm{t}} F_{\mathrm{ox}} \tag{5.49}$$

Here Q is the charge of the electron. This potential shifts the defect trap-level according to

$$E_{\mathrm{T}} = E_{\mathrm{T},0} + \Delta_{\mathrm{S}}\,, \tag{5.50}$$

where $E_{\mathrm{T},0}$ denotes the trap-level in flat-band conditions. Note that within the used band edge approximation, the positive defect state is not affected by the field and remains fixed at the valence band edge. Fig. 5.7 shows the typical situations for NBTI during recovery (left) and stress (right). As can be seen, the electric field has a large impact on the transition barriers $E_{\mathrm{B,c}}$ and $E_{\mathrm{B,e}}$ and subsequently the time constants τ_{c} and τ_{e}. The ratio

$$\frac{\tau_{\mathrm{c}}}{\tau_{\mathrm{e}}} = \exp\left(-\beta\left(E_{\mathrm{T}} - E_{\mathrm{F}}\right)\right) \tag{5.51}$$

reveals, that a hole capture event is favourable, when the trap-level is above the Fermi-level.

Die approbierte gedruckte Originalversion dieser Diplomarbeit ist an der TU Wien Bibliothek verfügbar
The approved original version of this thesis is available in print at TU Wien Bibliothek.
TU Bibliothek WIEN Your knowledge hub

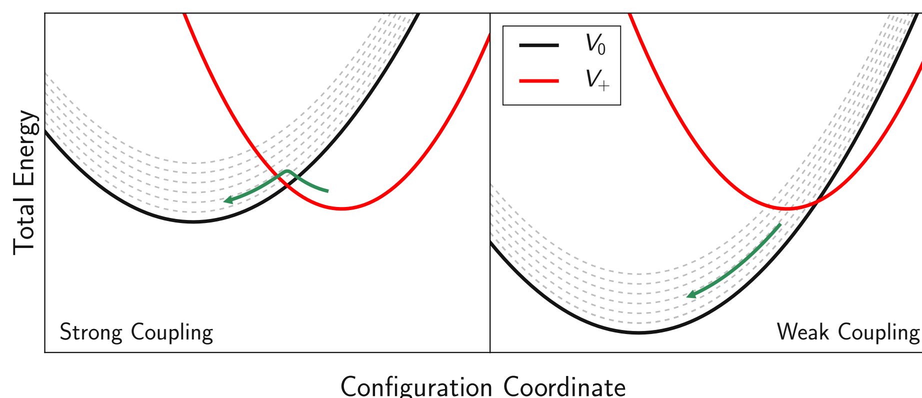

Figure 5.8: Influence of different electron-phonon coupling regimes on transition barriers according to [140]. **Left:** In the strong electron-phonon coupling regime there is a barrier in both directions. **Right:** In the weak-coupling regime one of the transitions is barrier-free due to excited states, which intersect the initial PES close at its minimum. [8]

5.4.4 Electron-Phonon Coupling Regimes

So far, in the classical limit of NMP theory the transition rate is determined by the energy barriers E_{ij} of the electronic ground states. However this does not necessarily hold true when considering excited states as well. Therefore one distinguishes between different electron-phonon coupling regimes, depending on the influence of the excited states on the transition rate. The concept of coupling regimes is usually applied under the assumption of parabolic PESs [141, 4]. Since this work also deals with anharmonic PES approximations, it is necessary to use a more general approach given in [140].

Strong Electron-Phonon Coupling

The strong electron-phonon coupling (SC) regime is defined by the conditions

$$V_i\left(q_{i,\mathrm{eq}}\right) < V_j\left(q_{i,\mathrm{eq}}\right) \tag{5.52a}$$
$$V_i\left(q_{j,\mathrm{eq}}\right) < V_j\left(q_{j,\mathrm{eq}}\right) \tag{5.52b}$$

In this case, as depicted in Fig. 5.8 (left), the lowest possible intersection point is determined by the ground state PESs. Therefore both transitions have a barrier and can be described with the previously developed NMP transition theory.

Weak Electron-Phonon Coupling

Weak electron-phonon coupling (WC) occurs, when excited states enable a lower transition barrier then the ground state. In Fig. 5.8 (right) this is shown for the transition $+ \Rightarrow 0$. Here an excited state of the neutral PES crosses the positive PES close to or at its minimum. This excited state therefore enables a nearly barrier-free transition. Due to the short life time of excited states, the following relaxation into the neutral ground

Die approbierte gedruckte Originalversion dieser Diplomarbeit ist an der TU Wien Bibliothek verfügbar
The approved original version of this thesis is available in print at TU Wien Bibliothek.
TU WIEN Bibliothek Your knowledge hub

state also happens with nearly no barrier.

It should be noted, that being in the SC or WC regimes is not an intrinsic defect property, since the relative positions of the PESs depends on the shift Δ_S and the energy levels of the reservoir state. In our settings, the hydrogen bridge and the hydroxyl-E′ center remain in the SC regime, whereas the oxygen vacancy is commonly close to or sometimes even in the WC regime.

5.5 Energy Alignment

As already mentioned, the defects treated in this work are in the oxide layer but exchange charges with the device substrate. Since only the oxide layer is simulated with DFT, the resulting energies have to be aligned accordingly in the band diagram of the device. This will be adressed briefly in the following.

To compare the energies of differently charged defect states, usually the formation energy with respect to the neutral, defect-free bulk structure is used [142]:

$$E_Q^{\mathrm{f}} \triangleq E_Q^{\mathrm{tot}} - E_{0,\mathrm{bulk}}^{\mathrm{tot}} - \sum_i n_i \mu_i + Q\left(E_{\mathrm{V}} + E_{\mathrm{F}}\right) . \tag{5.53}$$

Here, E_{tot}^{Q} denotes the total energy obtained with DFT for the defect state with charge Q. $E_{\mathrm{tot}}^{0,\mathrm{bulk}}$ is the total energy of the neutral defect-free structure. The atomic chemical potentials μ_i represent the required energy to remove/incorporate n_i atoms of kind i from/into the bulk structure in order to form the defect. Since all defects studied in this work have the same number of atoms in every charge state, these terms can be omitted. The last term accounts for the charge carrier energy as already discussed in Sec. 5.4.1. Note that E_{V} is the energy of the valence band and E_{F} is the Fermi-level with respect to E_{V}. Since we are using the band edge approximation described in Sec. 5.4.2 for hole traps in pMOS devices, charge exchange is only considered at the valence band edge (VBE), i.e. $E_{\mathrm{F}} = 0$.

In order to align the positive energy levels, the energy of the VBE E_{V} with respect to the DFT energies must be known. The VBE of the oxide layer can be estimated by the energy of the highest occupied Kohn-Sham orbital (HOMO) in the neutral defect-free structure:

$$E_{\mathrm{V}}^{\mathrm{SiO_2}} \approx E_{\mathrm{HOMO}}^{\mathrm{bulk}} \tag{5.54}$$

Furthermore it has to be considered, that the defect is in the oxide layer but charges are exchanged with the channel VBE. Therefore the band offset $E_{\mathrm{B,off}}$ between the Si and SiO_2 VBEs must be added as depicted in Fig. 5.9, leading to

$$E_{\mathrm{V}}^{\mathrm{Si}} = E_{\mathrm{V}}^{\mathrm{SiO_2}} + E_{\mathrm{B,off}} \approx E_{\mathrm{HOMO}}^{\mathrm{bulk}} + E_{\mathrm{B,off}} . \tag{5.55}$$

Die approbierte gedruckte Originalversion dieser Diplomarbeit ist an der TU Wien Bibliothek verfügbar
The approved original version of this thesis is available in print at TU Wien Bibliothek.
TU WIEN Bibliothek Your knowledge hub

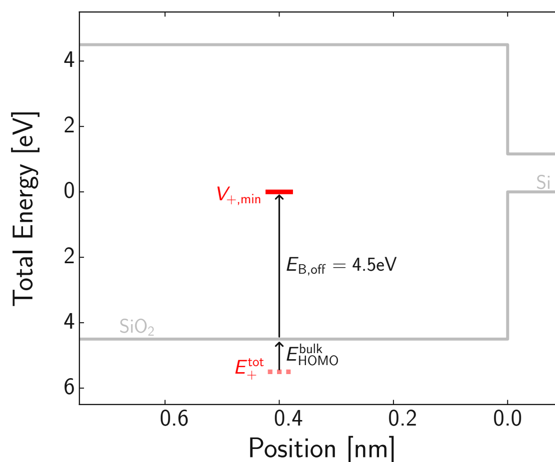

Figure 5.9: Energy alignment of the positive charge state in the device band diagram. The obtained total energies from DFT must be corrected by the HOMO energy to align them with the SiO_2 valence band. An additional band offset $E_{\mathrm{B,off}}$ must be considered due to the charge exchange with channel's valence band edge.

Throughout this work, a Si/SiO_2 band offset of $E_{\mathrm{B,off}} = 4.5$ eV is assumed. Including the shift Δ_{S}, the overall energies for the neutral and positive defect state in the band edge approximation then yield

$$V_0^{\mathrm{DFT}} \triangleq E_0^{\mathrm{tot}} + \Delta_{\mathrm{S}} \tag{5.56a}$$

$$V_+^{\mathrm{DFT}} \triangleq E_+^{\mathrm{tot}} + E_{\mathrm{V}}^{\mathrm{Si}} \,. \tag{5.56b}$$

These equations link the energies obtained with DFT to the energies relevant for the NMP model in order to calculate transition rates. This simple alignment scheme has been used previously to describe oxide defects with DFT [6, 8] and will also be used for the scope of this work.

It should be noted, that often an additional correction term Δv is introduced to compensate for the Coulomb self-interaction of charged defects due to the finite size of the simulation cell. This effect is neglected in this work, since Δv is usually smaller than 100meV [113, 142]

Die approbierte gedruckte Originalversion dieser Diplomarbeit ist an der TU Wien Bibliothek verfügbar
The approved original version of this thesis is available in print at TU Wien Bibliothek.
TU WIEN Bibliothek Your knowledge hub

Die approbierte gedruckte Originalversion dieser Diplomarbeit ist an der TU Wien Bibliothek verfügbar
The approved original version of this thesis is available in print at TU Wien Bibliothek.
TU WIEN Bibliothek Your knowledge hub

CHAPTER 6 PES Approximations

In the previous chapter a simple analytical NMP model was derived, to link the energy barriers obtained from DFT calculations to the experimentally accessable capture and emission time constants of charge transitions. However, the direct usage of physical PESs to calculate barriers and time constants is unfeasible due to the following reasons:

i) The PES of a system with N atoms is a $3N$-dimensional surface, resulting in an incredibly large configuration space even for smaller systems.

ii) No analytic expression for the PES is available, therefore $V_i(\boldsymbol{R})$ can only be evaluated numerically for a given set of nuclei positions $\boldsymbol{R}$.

iii) Using DFT to calculate a single point of the PES is already computationally highly demanding and can require several hours of computation time when running on a single core.

The main issue here is the high dimensionality of the PES. In order to perform transition calculations, the PESs are reduced to a one-dimensional curve $V_i(q)$ by choosing a certain reaction path $\boldsymbol{R}(q)$ between the neutral and positive charge state. Although this approach allows a straightforward treatment, the shape of the resulting PESs and subsequently the crossing point is strongly dependent on the chosen path. In the classical limit, NMP transition rates are dominated by the minimum energy path, which leads over the crossing point with the lowest possible energy, the so-called minimum energy crossing point (MECP). In this chapter, an efficient method to locate the MECP on the intersection surface of the two PESs is described. The barriers obtained with the MECP will be used later on as a reference to evaluate the accuracy of two simpler approximations, namely the direct path (DP) approximation and the harmonic (HA) approximation.

6.1 Simple Approximation Schemes

Before introducing the MECP search strategy, the HA and DP approximations will be discussed in more detail. Compared to the MECP search, these methods can be applied with little computational effort and provide a rough estimation of the transition barriers.

Die approbierte gedruckte Originalversion dieser Diplomarbeit ist an der TU Wien Bibliothek verfügbar
The approved original version of this thesis is available in print at TU Wien Bibliothek.
TU Bibliothek Your knowledge hub WIEN

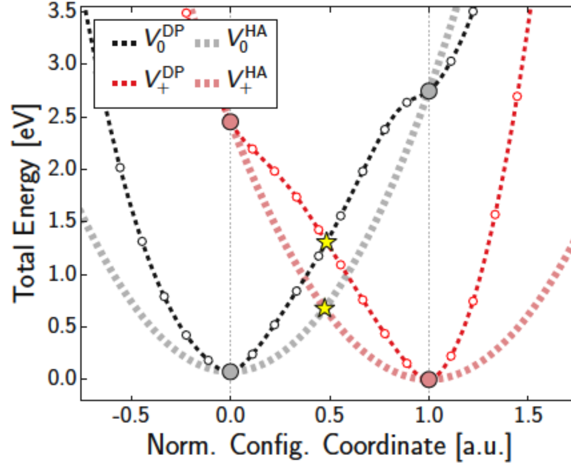

Figure 6.1: Comparison of the PESs resulting from direct path (DP) sampling and from the harmonic approximation (HA) in the case of a hydroxyl-E′ defect. The HA is constructed by fitting a parabola to the DFT energies marked by the filled circles. The empty circles on the DP energy profiles denote the sampled points along the direct path. [8]

6.1.1 Harmonic Approximation (HA)

Assuming that the crossing point is not far away from the equilibrium positions $\boldsymbol{R}_{0,\text{eq}}$ and $\boldsymbol{R}_{+,\text{eq}}$, it is reasonable to treat the defect states as harmonic oscillators. Therefore, the PESs are assumed to be parabolas. This approximation is very convienent, since it allows analytical expressions for the crossing point energy which can be efficiently used in a device simulator [4]. Usually the HA is obtained by simply fitting a parabola to the DFT energies at the minima positions $\boldsymbol{R}_{i,\text{eq}}$. This results in the one-dimensional PES representation [8, 143]

$$V_i^{\text{HA}}(q) \triangleq V_i^{\text{DFT}}[\boldsymbol{R}_{i,\text{eq}}] + \alpha_i (q - q_{i,\text{eq}})^2 \tag{6.1}$$

Here, V_i^{DFT} denotes the PES of state i obtained by DFT. α_i is a fitting parameter as depicted in Fig. 6.1. The HA is commonly used in the literature [12, 13, 14, 11, 8] due to its simplicity. It only requires two geometric optimizations to calculate $V_i^{\text{DFT}}[\boldsymbol{R}_{i,\text{eq}}]$ and two additional single-point DFT calculations to obtain $V_0^{\text{DFT}}[\boldsymbol{R}_{+,\text{eq}}]$ and $V_+^{\text{DFT}}[\boldsymbol{R}_{0,\text{eq}}]$. Therefore the HA is computationally very cheap. It was assumed that, this approximation is not accurate, since it is linked to the physical PES by only two points for each charge state [8].

6.1.2 Direct Path Sampling (DP)

A different approach for approximating the defect PESs is to sample the energies at multiple points along the direct path between the two minima configurations. This

Die approbierte gedruckte Originalversion dieser Diplomarbeit ist an der TU Wien Bibliothek verfügbar
The approved original version of this thesis is available in print at TU Wien Bibliothek.
TU Bibliothek WIEN Your knowledge hub

method leads to an energy profile expressed as [8, 143]

$$V_i^{\mathrm{DP}}(q) \triangleq V_i^{\mathrm{DFT}}\left[\boldsymbol{R}^{\mathrm{DP}}(q)\right] . \tag{6.2}$$

Here, $\boldsymbol{R}^{\mathrm{DP}}(q)$ represents the straight line connecting the minima $\boldsymbol{R}_{i,\mathrm{eq}}$ and is given by

$$\boldsymbol{R}^{\mathrm{DP}}(q) \triangleq \boldsymbol{R}_{0,\mathrm{eq}} + q\left(\boldsymbol{R}_{+,\mathrm{eq}} - \boldsymbol{R}_{0,\mathrm{eq}}\right) . \tag{6.3}$$

Note that the reaction coordinate q is normalized in the sense that $q = 0.0$ and $q = 1.0$ refer to the equilibrium positions. This normalized reaction coordinate (NRC) is also used later on to compare the different PES approximations in a single diagram. In this work the DP approximation is obtained by evaluating the energies with DFT for 30 uniformly spaced sampling points in the range $q \in [-1.0, 2.0]$ and a spline interpolation in between as depicted in Fig. 6.1. The DP approximation was used in previous works as a reference to compare different analytical PES approximations [144, 8]. However, in the next section, it will be demonstrated using the MECP method, that the DP is in general not suitable to give accurate results due to its tendency to considerably overestimate transition barriers.

6.2 Minimum Energy Path

Similar to the transition state theory discussed in Sec. 5.1, NMP transition rates in the classical limit depend exponentially on the reaction barrier. The minimum energy path (MEP) between the two states therefore dominates the overall rates. Contrary to TST however, the MEP does not solely lie on one surface but leads across the minimum energy crossing point (MECP) and lies on both surfaces. Therefore, in this case, the MEP cannot be constructed by a simple NEB calculation as discussed in Sec. 5.2. In this work, the search for the MEP along two seperate PESs is split into two seperate tasks:

i) First, a constraint optimization algorithm is used to locate a MECP between the initial and final state. It should be noted, that the found MECP is in general only a local solution, due to the use of gradient-based local optimization schemes.

ii) Second, the MECP is connected to the minimum configurations by an IT-NEB calculation. A CI-NEB is not applicable in this case, since one of the endpoints (the MECP) is not a local minimum.

The resulting MEP is depicted in Fig. 6.2 for analytical two-dimensional PESs. At first glance, the second step of the procedure seems to be unnecessary, since only the MECP determines the NMP barriers. However, it can not be ruled out that there is a point along the MEP with an energy higher than the MECP. In this case, a thermal barrier would have to be overcome first. Although this scenario did not occur in our studies, it was important to consider, since this would have altered the resulting transition rates significantly. The implemented MECP search strategy will be discussed in the following.

Die approbierte gedruckte Originalversion dieser Diplomarbeit ist an der TU Wien Bibliothek verfügbar
The approved original version of this thesis is available in print at TU Wien Bibliothek.
TU WIEN Bibliothek Your knowledge hub

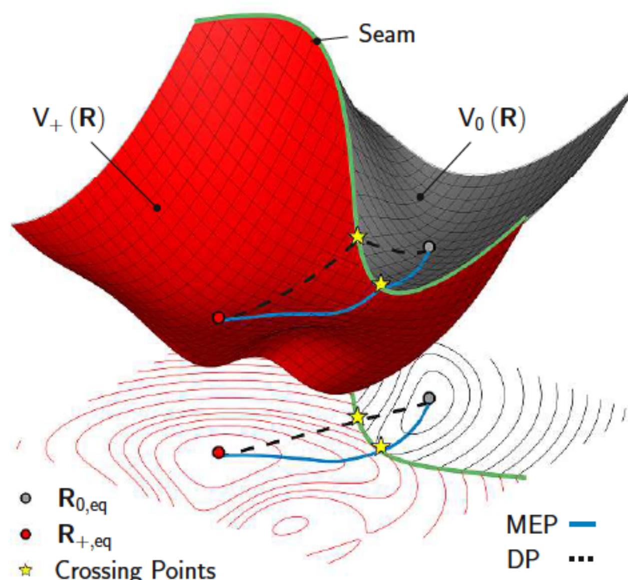

Figure 6.2: Different investigated transition paths on two schematic PESs. Sampling along the direct path in general leads to a significant overestimation of the barriers, compared to the minimum energy path (blue). The MEP connects the two PESs across the MECP and therefore gives a better estimation of the overall transition rates in the classical limit of NMP theory. [143]

6.2.1 MECP Optimization Problem

Along a certain reaction path, the resulting PESs in general only intersect at isolated points as shown in Fig. 6.1. The situation changes, when the whole $3N$-dimensional surfaces are considered. Here, the set of intersection points, the so-called seam, is a high-dimensional surface itself. Searching for the MECP is equivalent to minimizing the energy inside the seam and can be formulated as a constraint optimization problem:

$$\underset{\boldsymbol{R}\in\mathbb{R}^{3N}}{\text{minimize}} \quad F(\boldsymbol{R}) \triangleq V_0^{\mathrm{DFT}}[\boldsymbol{R}] + V_+^{\mathrm{DFT}}[\boldsymbol{R}] \tag{6.4a}$$

$$\text{subject to} \quad C(\boldsymbol{R}) \triangleq V_0^{\mathrm{DFT}}[\boldsymbol{R}] - V_+^{\mathrm{DFT}}[\boldsymbol{R}] \overset{!}{=} 0 \tag{6.4b}$$

The objective function $F(\boldsymbol{R})$ has to be minimized under the constraint $C(\boldsymbol{R}) \overset{!}{=} 0$ in order to obtain the MECP. Note that the same solution can also be obtained by using only $V_0^{\mathrm{DFT}}[\boldsymbol{R}]$ or $V_+^{\mathrm{DFT}}[\boldsymbol{R}]$ as objective functions. However, it was demonstrated, that the optimization scheme becomes numerically more stable when using the sum of both potential energies as objective function [145].

There are several nonlinear codes available to solve Eq. 6.4. A comparative study conducted in [146] showed that the sequential quadratic programming (SQP) method is the most stable and efficient algorithm to solve this kind of optimization problem for a moderate number of dimensions (dim $\leq$ 100). For that reason, SQP was used in this

Die approbierte gedruckte Originalversion dieser Diplomarbeit ist an der TU Wien Bibliothek verfügbar
The approved original version of this thesis is available in print at TU Wien Bibliothek.
TU WIEN Bibliothek Your knowledge hub

work to locate the MECP within the seam. Although the number of dimensions in the studied amorphous SiO_2 is much larger, during a typical charge transition only atoms in the vicinity of the defect site move considerably, whereas the bulk material is mostly unaffected. Therefore, the system has effectively fewer degrees of freedom and SQP can be used for the MECP search.

Sequential Quadratic Programming

The constraint optimization problem Eq. 6.4 can be solved iteratively. Starting from an initial guess $\boldsymbol{R}_0$, a series of vectors in the configuration space is constructed through

$$\boldsymbol{R}_{k+1} \triangleq \boldsymbol{R}_k + \alpha_k \boldsymbol{d}_k \,, \tag{6.5}$$

where $\boldsymbol{d}_k$ denotes the search direction and α_k is the step length in the current iteration. The main idea of SQP is to approximate the original nonlinear problem with an quadratic one in every step. The direction $\boldsymbol{d}_k$ is then given by the solution of the analytically solvable quadratic subproblem [147]

$$\underset{\boldsymbol{d}_k \in \mathbb{R}^{3N}}{\text{minimize}} \quad \frac{1}{2}\boldsymbol{d}_k^{\mathrm{T}} \boldsymbol{B}_k \boldsymbol{d}_k + \boldsymbol{d}_k^{\mathrm{T}} \left.\nabla F\right|_{\boldsymbol{R}_k} \tag{6.6a}$$

$$\text{subject to} \quad \boldsymbol{d}_k^{\mathrm{T}} \left.\nabla C\right|_{\boldsymbol{R}_k} + C\left(\boldsymbol{R}_k\right) \overset{!}{=} 0\,. \tag{6.6b}$$

Here, $\boldsymbol{B}_k$ denotes the Hesse matrix of the objective function F at the point $\boldsymbol{R}_k$. Note that the constraint is approximated to first order only, whereas the objective function is approximated to second order. The DFT calculations used to obtain F and C can only provide the energy $V_i^{\mathrm{DFT}}\left(\boldsymbol{R}_k\right)$ and the energy gradient $\nabla V_i^{\mathrm{DFT}}$ of the system. The Hesse matrix therefore has to be approximated by an iterative scheme like the already mentioned BFGS algorithm or the Powell scheme [148]. Further information about the implementation of SQP used in this work can be found in [149].

6.2.2 MECP Search Implementation

As already discussed in Sec. 4.6, CP2K was used for DFT calculations due to its performance benefits. However, CP2K does not provide an implemented routine to find the MECP on its own. Instead, a Python script was written to act as a link between the DFT code and an implementation of the SQP algorithm provided in the *SciPy* package [150, 151, 152]. Every function call issued by the SQP optimizer is forwarded to CP2K in order to calculate $F\left(\boldsymbol{R}_k\right)$ and $C\left(\boldsymbol{R}_k\right)$ as well as their gradients.

MECP Calculation for Varying Oxide Fields

As far as the harmonic approximation and the direct path sampling are concerned, the reaction path is always the straight line connecting the differently charged state minima. Therefore, the reaction path does not change when an electric field is present

Die approbierte gedruckte Originalversion dieser Diplomarbeit ist an der TU Wien Bibliothek verfügbar
The approved original version of this thesis is available in print at TU Wien Bibliothek.
TU WIEN Bibliothek Your knowledge hub

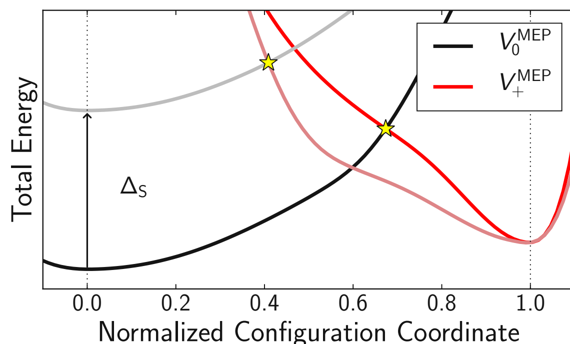

Figure 6.3: Impact of a shift Δ_S induced by an oxide field on the energy profiles along the MEP. A shift of the neutral PES causes the MECP to change its position. As a consequence, the MEP itself is dependent on the shift Δ_S, resulting in different PES shapes in the configuration coordinate diagram above. Note that the high-dimensional PES is still assumed to be just shifted but not altered in its shape, the visible PES deformation is only an artifact of the one-dimensional representation along the MEP.

in the oxide and the crossing points can be obtained by simply shifting the neutral PES by Δ_S as described in Sec. 5.4.3. However, this is not possible when calculating the MECP, since the minimum energy path itself depends on the shift Δ_S as depicted in Fig. 6.3. As a consequence, the MECP has to be calculated individually with DFT for every considered value of Δ_S. In this work, the MECP was calculated for the shift values

$$\Delta_\mathrm{S} = 0.0,\ \pm 0.125,\ \pm 0.25, \pm 0.5,\ \pm 1.0\,\mathrm{eV} \tag{6.7}$$

This range was chosen, since it includes the shift values typically reached in our measurements. The resulting capture and emission barriers $E_\mathrm{B}^{\mathrm{MEP}}\left(\Delta_\mathrm{S}\right)$ for values Δ_S between these datapoints are interpolated. As will be seen later in the results chapter, for example in Fig. 7.1, this approach is well justified.

Initial Guess

As already mentioned, SQP is a gradient based local optimization scheme, therefore a reasonable initial guess $\boldsymbol{R}_0$ must be provided to find the (local) MECP. This problem does not only concern the implemented MECP search routine, but also virtually all other optimization schemes used in computational chemistry, like geometry optimization or NEB. Typically, non-gradient based global optimization algorithms are not applicable due to the high-dimensional configuration space. For the purpose of this work, the initial guess was chosen to be the crossing point in the DP approximation:

$$\boldsymbol{R}_0 \triangleq \boldsymbol{R}_{\mathrm{CP}}^{\mathrm{DP}} \tag{6.8}$$

This choice is reasonable, since $\boldsymbol{R}_{\mathrm{CP}}^{\mathrm{DP}}$ is already a point inside the seam. With this approach, the MECP search is biased in favor of local solutions near the direct path.

Die approbierte gedruckte Originalversion dieser Diplomarbeit ist an der TU Wien Bibliothek verfügbar
The approved original version of this thesis is available in print at TU Wien Bibliothek.
TU WIEN Bibliothek Your knowledge hub

Convergence Criteria

Given that a whole ensemble of defects is studied in this work, the computational effort for a single defect must be kept to a minimum. In order to minimize the necessary optimization steps in the SQP algorithm, rather generous convergence criteria were applied. Throughout the statistical analysis given in the next section, the following criteria were used:

i) $|C(\boldsymbol{R}_k)| \leq 2.0 \times 10^{-3}$ eV

ii) $|F(\boldsymbol{R}_k) - F(\boldsymbol{R}_{k-1})| \leq 1.0 \times 10^{-3}$ eV

iii) $\|\boldsymbol{R}_k - \boldsymbol{R}_{k-1}\|_2 \leq \sqrt{3N} \times 1.0 \times 10^{-2}$ Å

iv) $\|\boldsymbol{R}_k - \boldsymbol{R}_{k-1}\|_{\max} \leq 2 \times 10^{-2}$ Å

These settings were derived by running a few tests with stricter criteria. The values were chosen so that the resulting energy of the MECP would lie within 10 meV of the results when using the strict criteria. In this case, the energy error is well below the thermal energy $k_\mathrm{B}T \approx 26$meV at room temperature and therefore insignificant. Using these settings, typically $20 - 30$ iterations are necessary to reach convergence.

Die approbierte gedruckte Originalversion dieser Diplomarbeit ist an der TU Wien Bibliothek verfügbar
The approved original version of this thesis is available in print at TU Wien Bibliothek.
TU WIEN Bibliothek Your knowledge hub

TU WIEN Bibliothek Your knowledge hub
Die approbierte gedruckte Originalversion dieser Diplomarbeit ist an der TU Wien Bibliothek verfügbar
The approved original version of this thesis is available in print at TU Wien Bibliothek.

CHAPTER 7

Results

In order to evaluate the accuracy of the harmonic approximation (HA) and the direct path sampling (DP), both methods are applied to multiple defects in amorphous SiO_2 structures and are compared to the results obtained using the minimum energy path (MEP). In this study, 11 HB defects, 27 H-E′ centers and 14 OVs (see Sec. 3.5) are investigated in order to provide statistical data. Note that in this study only the transitions $1 \Leftrightarrow 2'$ are considered. All calculations were carried out on a pMOS test device with an oxide thickness of $d_{\mathrm{ox}} = 9.5\mathrm{nm}$ and an assumed defect/interface distance of $x_{\mathrm{t}} = 1.0\mathrm{nm}$. Throughout this study, the band edge approximation Eq. 5.47 is used, to relate energy barriers to capture and emission time constants. The findings presented in this chapter will also be published in [143].

7.1 Representative Case Study

Fig. 7.1-7.3 show the different PES approximations and their influence on the transition barriers as well as the resulting capture and emission time constants for one representative of each defect type studied in this work. In those figures, the upper right diagrams depict the calculated PESs for all three approximation schemes as well as the corresponding crossing points under flat-band conditions ($\Delta_{\mathrm{S}} = 0.0\mathrm{eV}$). As depicted in the lower row, the resulting barrier heights $E_{\mathrm{B}}(\Delta_{\mathrm{S}})$ for hole capture and emission are very sensitive to the applied bias (represented by Δ_{S}). The corresponding capture and emission times vary by several orders of magnitude due to the exponential dependence on the barriers. The accuracy of the different approximations is quantified by a L^2 norm, which measures the deviation of the resulting time constants $\tau_{\mathrm{c}}, \tau_{\mathrm{e}}$ from the values $\tau_{\mathrm{c}}^{\mathrm{MEP}}, \tau_{\mathrm{e}}^{\mathrm{MEP}}$ obtained using the MEP method. Lower score values indicate a better agreement with the MEP results.

Depending on the applied bias Δ_{S}, both charge states of the hydrogen related defects HB and H-E′ can be thermodynamically stable. Therefore, these defects are electrically active and can cause BTI degradation. The boundary between the two regimes (preferably positively or preferably neutrally charged) is given by the intersection of the $\tau_{\mathrm{c}}(\Delta_{\mathrm{S}})$ and $\tau_{\mathrm{e}}(\Delta_{\mathrm{S}})$ curves. For bias conditions near this crossover region, capture and emission

TU WIEN Bibliothek Your knowledge hub
Die approbierte gedruckte Originalversion dieser Diplomarbeit ist an der TU Wien Bibliothek verfügbar
The approved original version of this thesis is available in print at TU Wien Bibliothek.

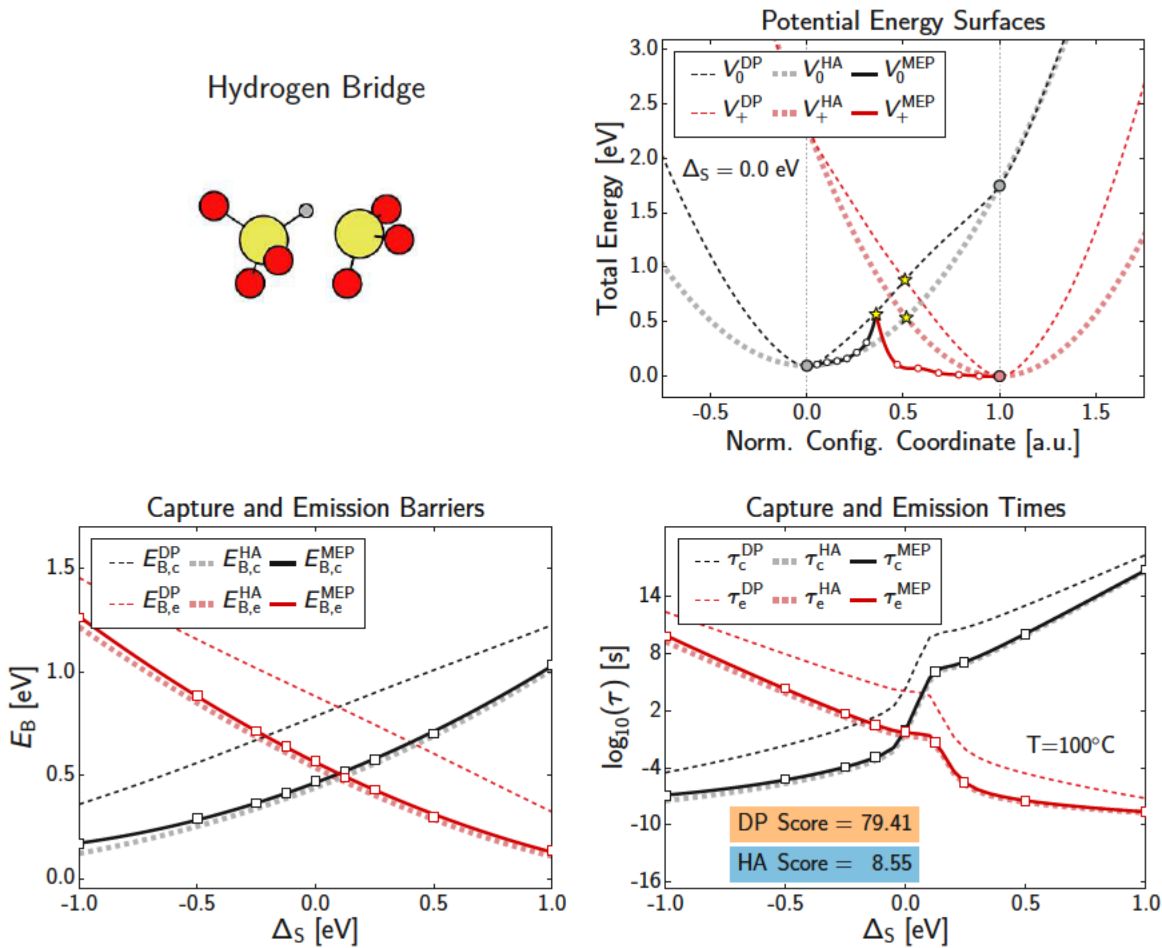

Figure 7.1: Comparison of the different PES approximations for a particular hydrogen bridge defect in amorphous SiO_2 **(upper right)**. Applying an electric field induces a relative shift Δ_S of the PESs, resulting in varying barrier heights for capture and emission **(lower left)**. Using the band edge approximation described in Sec. 5.4.2, the barriers can be converted into capture and emission time constants. **(lower right)**. Here, the square markers indicate the MEP values obtained for the shift values given in Eq. 6.7. A L^2 norm was used as a score function to quantify the accuracy of the harmonic approximation (HA) and the direct path sampling (DP) with respect to the minimum energy path (MEP). The HA matches the MEP barriers surprisingly well, whereas the DP overestimates the barriers significantly. [143]

Die approbierte gedruckte Originalversion dieser Diplomarbeit ist an der TU Wien Bibliothek verfügbar
The approved original version of this thesis is available in print at TU Wien Bibliothek.
TU WIEN Bibliothek Your knowledge hub

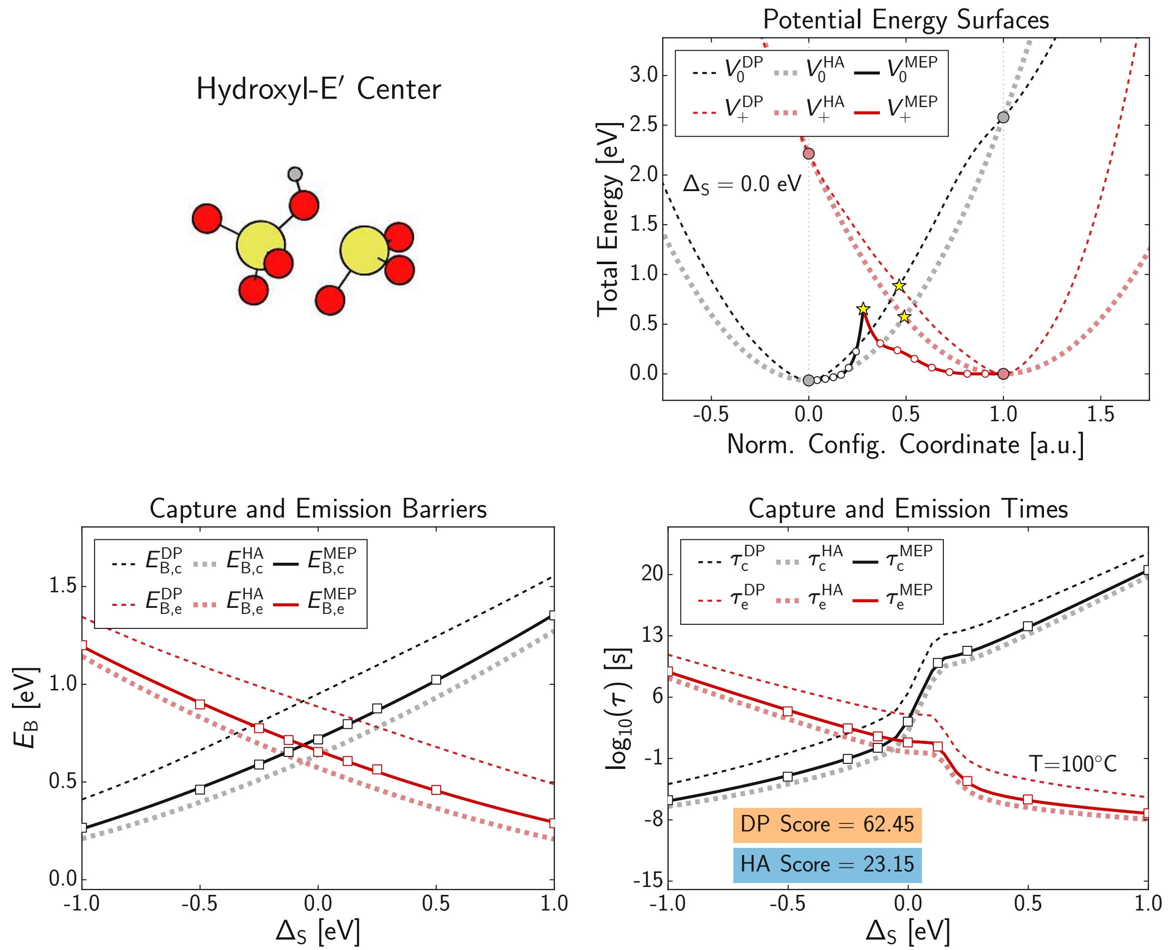

Figure 7.2: Same as in Fig. 7.1 but for an hydroxyl-E′ center. Again, the simple HA is more accurate than the DP. Note that the approximation error of the HA is larger for the H-E′ center than for the HB defect. This also holds true on a statistical level as will be presented in Sec. 7.2.1. The reason for the worse approximation is the more complex path in configuration space of the H-E′ center during a transition. [143]

Die approbierte gedruckte Originalversion dieser Diplomarbeit ist an der TU Wien Bibliothek verfügbar
The approved original version of this thesis is available in print at TU Wien Bibliothek.
TU WIEN Bibliothek Your knowledge hub

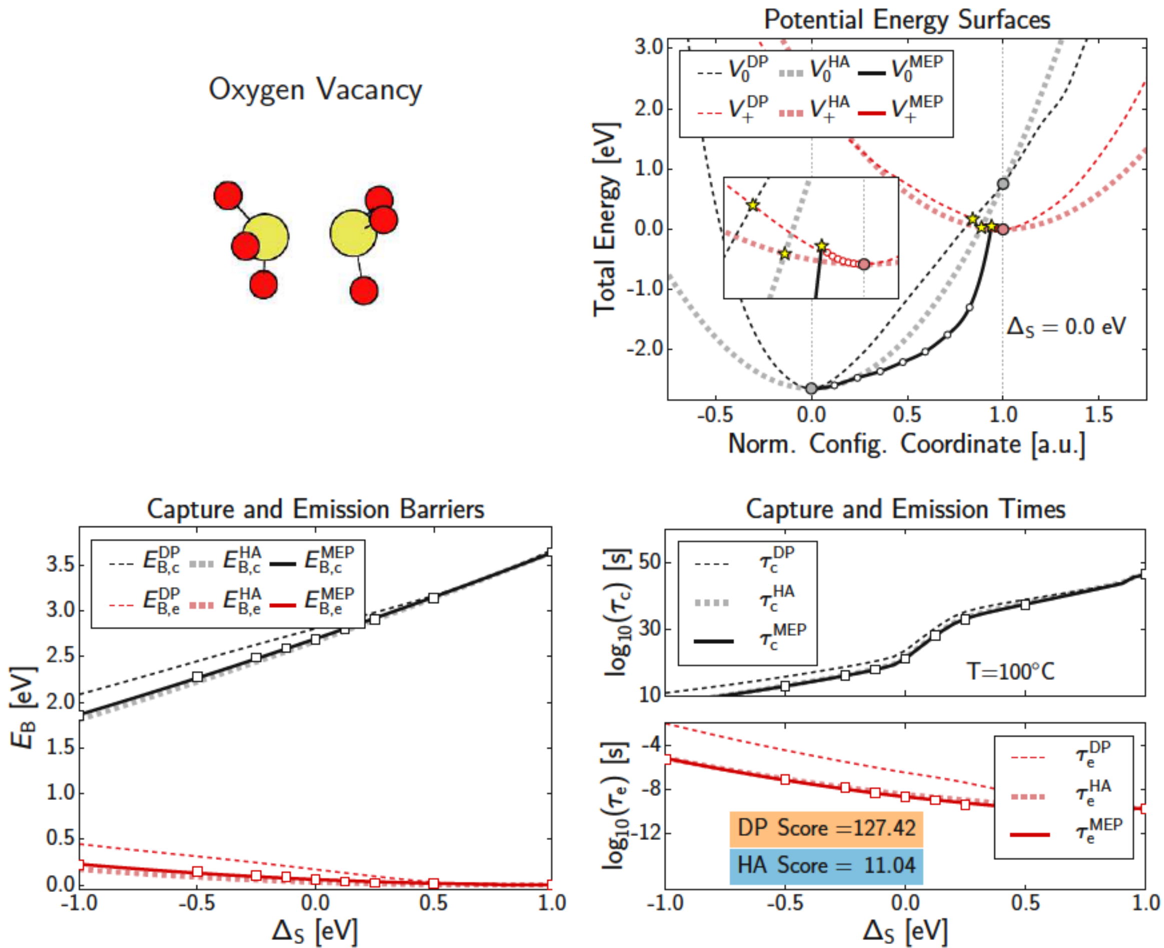

Figure 7.3: Same as in Fig. 7.1 but for an oxygen vacancy. The trap-level of the OV is far below the valence band edge of the channel. Therefore the OV remains neutral and is electrically inactive under typical operating conditions. Note that the OV is nearly in the weak coupling regime and therefore all three PES approximations give similar results. [143]

Die approbierte gedruckte Originalversion dieser Diplomarbeit ist an der TU Wien Bibliothek verfügbar
The approved original version of this thesis is available in print at TU Wien Bibliothek.
TU WIEN Bibliothek Your knowledge hub

time constants are very similar, leading to continous charging and discharging of the defect, which results in an observable RTN noise. On the other hand, the trap-level of the oxygen vacancy is far below the valence band edge, therefore the OV stays in the neutral state for nearly all relevant bias conditions. Hence the OV is electrically inactive and is a very unlikely defect candidate to explain the BTI phenomenon. Note that for the OV, the different PES approximations give very similar results, since this defect is close to the weak coupling regime (see Sec. 5.4.4) and the crossing point lies close to the minimum of the positive PES.

A general observation for all three defects is that the DP approximation always overestimates the transition barriers. This was expected, because the MECP in general does not lie on the direct path. The DP method leads to approximation errors of several orders of magnitude for τ_c and τ_e. Surprisingly, the simple harmonic approximation is in much better agreement with the MEP results, however, it seems to slightly underestimate the barrier heights. This finding also holds true on a statistical level, as will be shown in the following.

7.2 Statistical Evaluation in Amorphous SiO_2

In amorphous host materials defect parameters depend strongly on the local environment. This leads to significant variations of the defect energy levels and consequently to a wide distribution of possible transition times even within the same defect species. This spreading is depicted in Fig. 7.4 for the 27 H-E′ defects studied in this work. Note that this figure only shows the results of the MEP approach, but similar findings also hold for the other approximation schemes. The large variations make it evident, that studying single defects in amorphous SiO_2 is futile and reliable conclusions about the PES approximation accuracy can only be drawn from a larger data set. In the following, the statistical errors for the HA and DP approximation are examined. Note that only the capture time τ_c is considered here, since within the band edge approximation, the emission time τ_e can be calculated from τ_c using Eq. 5.51 and therefore contains no new information.

7.2.1 Transition Time Accuracy

The statistical deviations of τ_c between the different PES approximations can be presented conveniently by double-logarithmic correlation plots as depicted in Fig. 7.5. In these plots, the y-coordinates are the values of $\tau_c\,(\Delta_S)$ obtained by the DP and HA approximations, whereas the x-coordinates are the corresponding reference values resulting from the MEP approach. For a good PES approximation, the points would lie close to or at the diagonal in such correlation plots. To measure the approximation accuracy, the off-diagonality was quantified with a L^2 score function.

Die approbierte gedruckte Originalversion dieser Diplomarbeit ist an der TU Wien Bibliothek verfügbar
The approved original version of this thesis is available in print at TU Wien Bibliothek.
TU Bibliothek WIEN Your knowledge hub

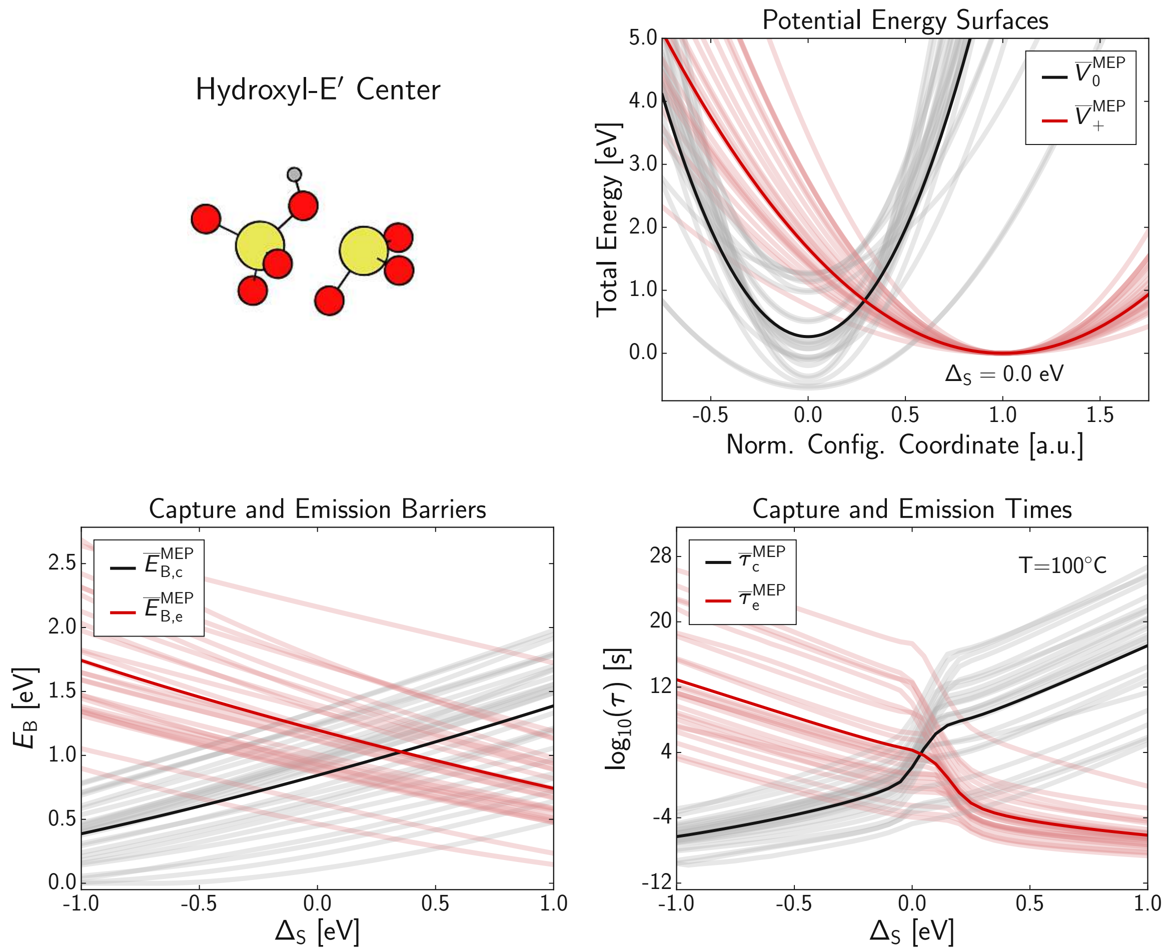

Figure 7.4: Same as Fig. 7.2, but for all H-E′ defects studied in this work. The wide spreading of defect characteristics is due to variations of the defect surroundings in amorphous SiO_2, leading to a broad distribution of barrier heights and transition times. The darker lines depict the ensemble averages of the considered parameters. [143]

Die approbierte gedruckte Originalversion dieser Diplomarbeit ist an der TU Wien Bibliothek verfügbar
The approved original version of this thesis is available in print at TU Wien Bibliothek.
TU WIEN Bibliothek Your knowledge hub

The DP approximation shows a pronounced off-diagonality for the HB and H-E′ center defects, indicating a significant overestimation of τ_c. The HA on the other hand, provides more accurate results but slightly underestimates τ_c in general. Furthermore it seems as if the HA approximation generally yields better results for the HB defects than for the H-E′ centers. In the case of the OV defect, the DP and HA approximation both are in excellent agreement with the MEP method. As already depicted in Fig. 7.3, the crossing points all lie very close to the positive minimum since the OVs are nearly in the WC regime.

All these findings show that the insights gained for individual defects in Fig. 7.1-7.3 are also valid on a statistical level.

7.2.2 Slope Accuracy

The logarithmic $\tau(\Delta_S)$ plots in Fig. 7.1-7.3 show that the slope

$$m \triangleq \frac{\mathrm{d}\ln(\tau)}{\mathrm{d}\Delta_S} \tag{7.1}$$

is nearly constant in the regime of strong oxide fields ($|\Delta_S| \gg 0.0$eV). This slope can be used to estimate the trap position x_t in experiments [153]. Therefore the impact of the PES approximations on the slope should also be considered. The correlation plots presented in Fig. 7.6 show the slopes m_c of the capture times $\tau_c(\Delta_S)$ for $\Delta_S \ll 0.0$ eV. As can be seen, the DP approximation tends to underestimate the slope, whereas the HA approximation yields much better results, further indicating its superiority over the DP approach.

7.2.3 Activation Energies

Experimentally, the temperature dependence of the transition times is used to estimate the activation energy E_A of the transition. Assuming a first-order rate limited process, the relation between the capture time τ_c and the capture activation energy $E_{A,c}$ is given by the Arrhenius law

$$\tau_c = A\exp(\beta E_{A,c}) \tag{7.2}$$

where A is a temperature-independent prefactor. In so-called Arrhenius plots the transition time is plotted against the inverse temperature $1/T$, resulting in a straight line for first-order processes. The slope of this lines determines the activation energy. Such Arrhenius plots are presented for each defect type in Fig. 7.7. Here, τ_c is evaluated for the temperatures $T = 50$, 100, 150, 200 °C and all three PES approximations. The activation energies are estimated by fitting a straight lines to these data points. Furthermore the average activation energies $\overline{E}_{A,c}$ for each defect type are given. Note that for the hydrogen related defects, a shift $\Delta_S = 0.3$eV was assumed, whereas a strong negative bias of $\Delta_S = -1.0$eV was used for the OV in order to obtain reasonable timescales for τ_c. The Arrhenius plots essentially reflect the already discussed findings concerning

Die approbierte gedruckte Originalversion dieser Diplomarbeit ist an der TU Wien Bibliothek verfügbar
The approved original version of this thesis is available in print at TU Wien Bibliothek.
TU WIEN Bibliothek Your knowledge hub

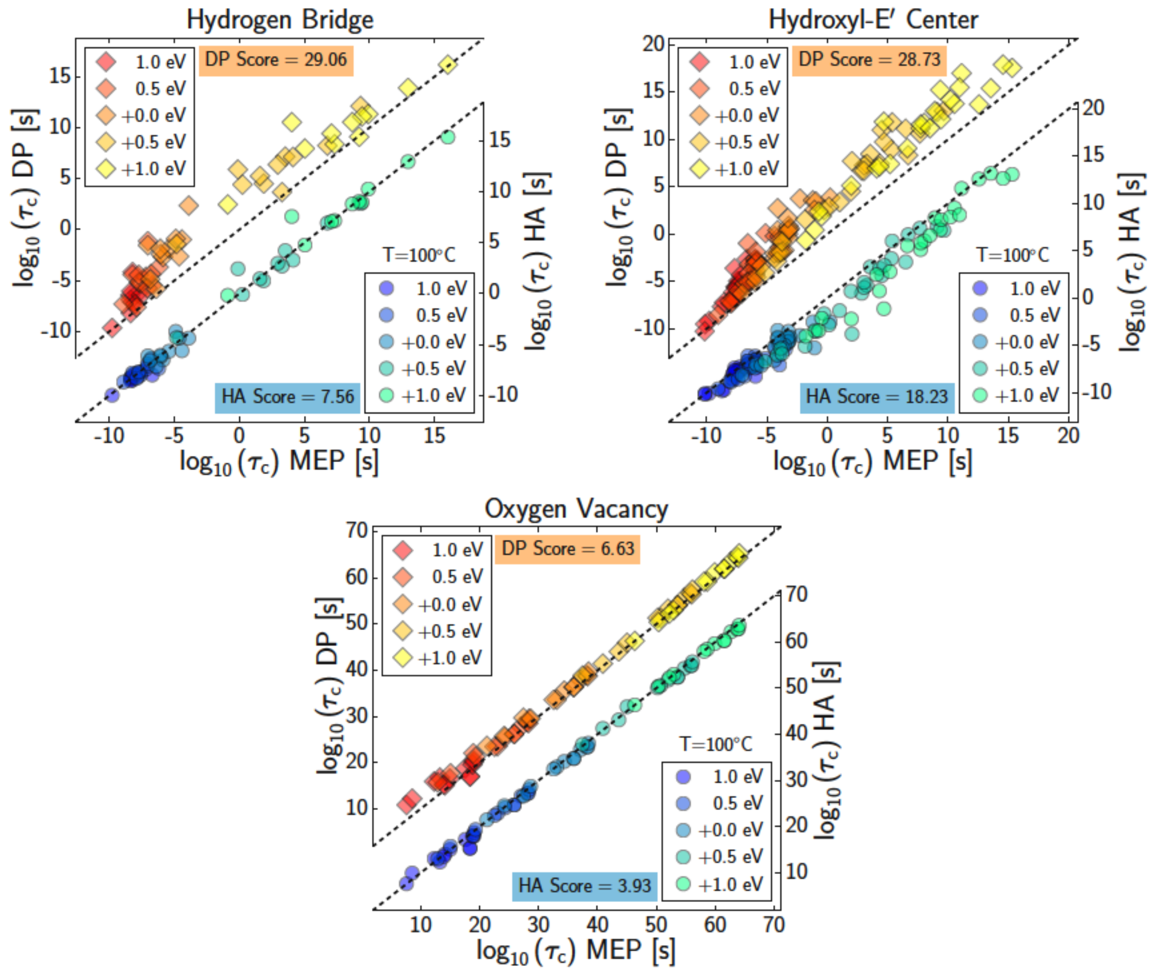

Figure 7.5: Double logarithmic correlation plots to depict the accuracy of the HA and DP approximation for predicting the values of τ_c at $T = 100°C$. In the upper half of each figure, the correlation between the values obtained with direct path sampling and the MEP reference is shown. Similarly, the lower half compares the results of the harmonic approximation with the MEP values. The off-diagonality is a measure for the approximation error and is quantified with a L^2 norm. [143]

Die approbierte gedruckte Originalversion dieser Diplomarbeit ist an der TU Wien Bibliothek verfügbar
The approved original version of this thesis is available in print at TU Wien Bibliothek.
TU Wien Bibliothek Your knowledge hub

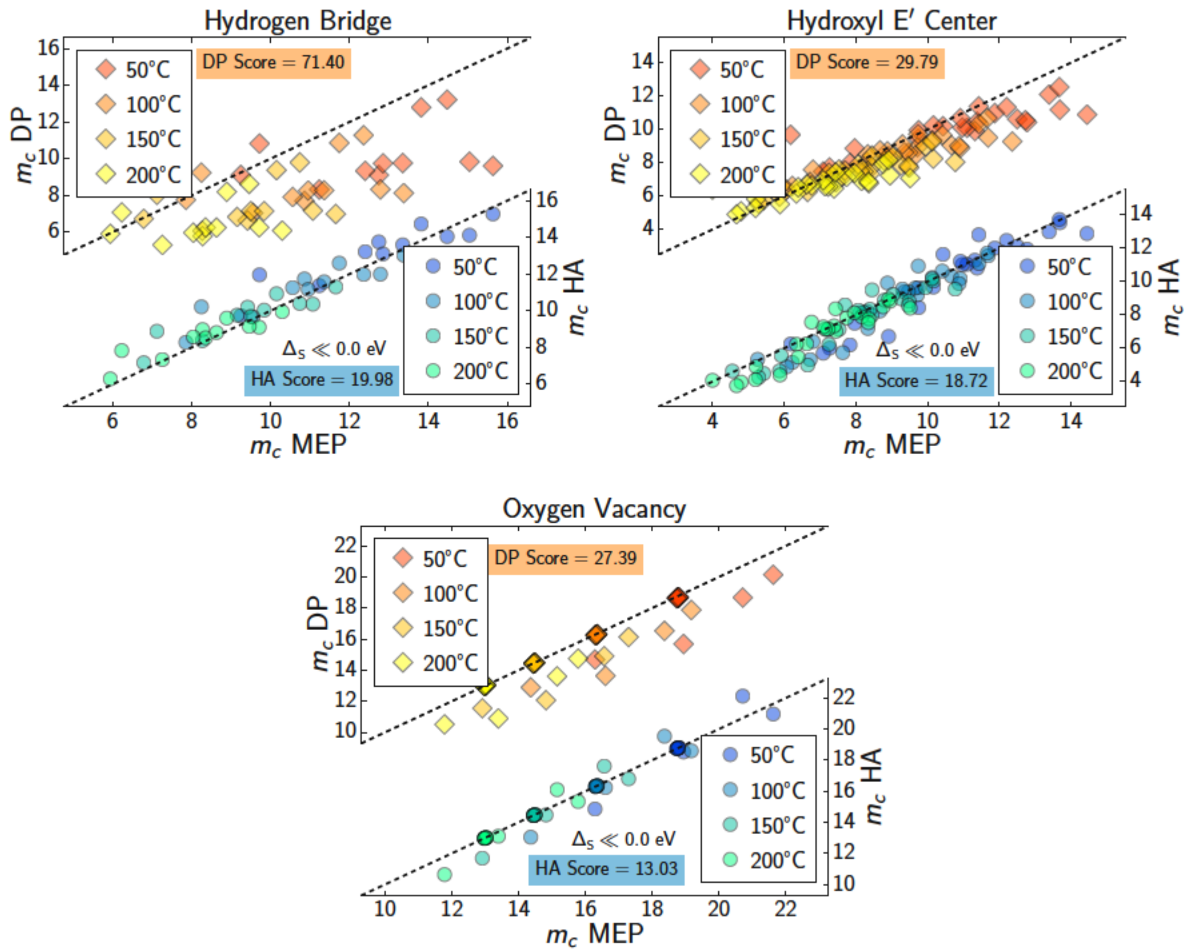

Figure 7.6: Correlation plots similar to Fig. 7.5 for the slope m_c, as defined in Eq. 7.1, at $\Delta_S \ll 0.0$ eV and different temperatures. Clearly the DP approximation underestimates the slopes, whereas the HA consistently gives good results with respect to the MEP values. [143]

Die approbierte gedruckte Originalversion dieser Diplomarbeit ist an der TU Wien Bibliothek verfügbar
The approved original version of this thesis is available in print at TU Wien Bibliothek.
TU Bibliothek Your knowledge hub WIEN

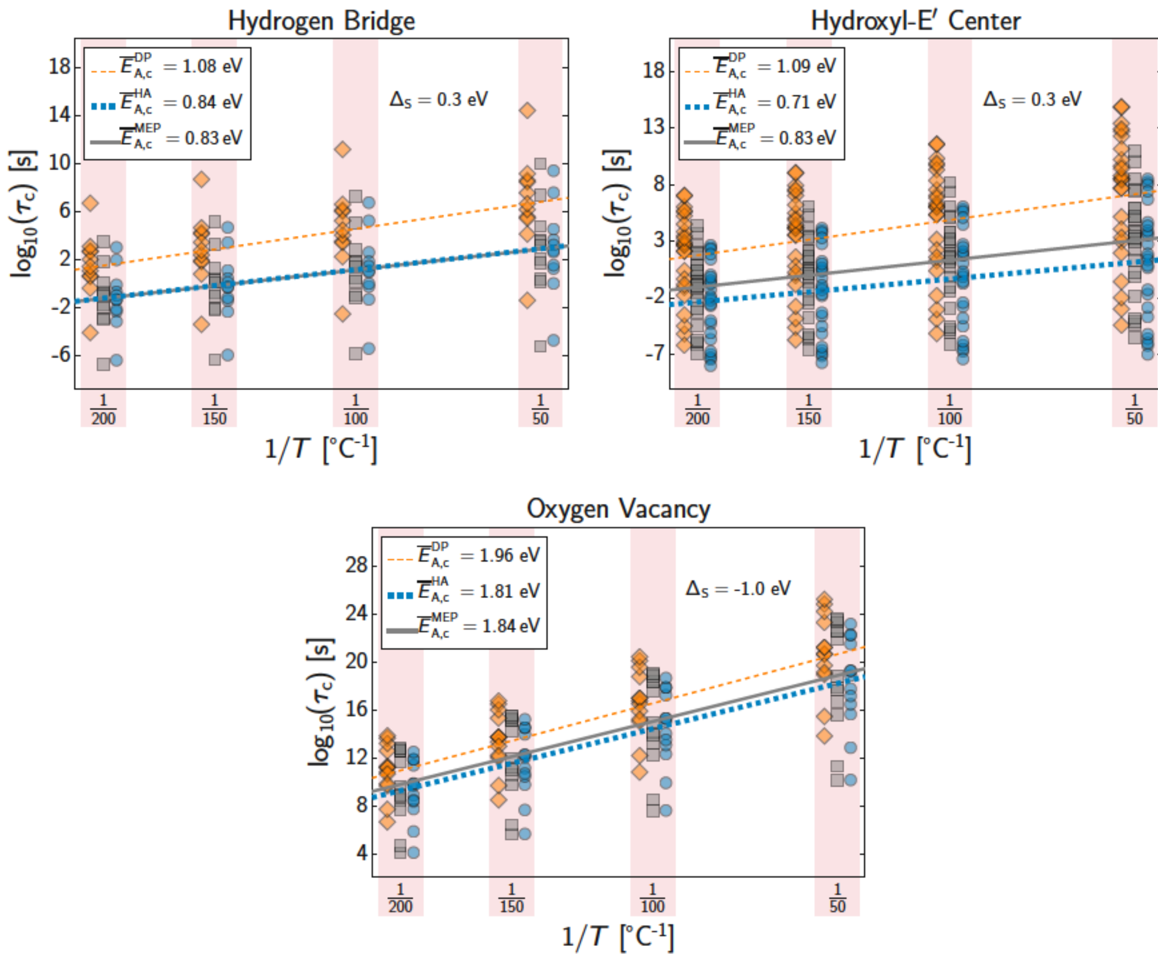

Figure 7.7: Arrhenius plots for the three investigated defect types showing the temperature dependence of τ_c. For the HB and H-E′ defects the capture times were evaluated at a shift $\Delta_S = 0.3$ eV, whereas $\Delta_S = -1.0$ eV, was used for the OV, since otherwise τ_c would reach enormous timescales. The lines are a least-squares fit to the data points, providing the slope to calculate an average $\overline{E}_{A,c}$ for every defect type. As already seen in the previous figures, the results for the OV do not depend strongly on the used approximation. For the other defect types, the harmonic approximation is again in much better agreement with the results obtained using the MEP than the direct path sampling. [143]

Die approbierte gedruckte Originalversion dieser Diplomarbeit ist an der TU Wien Bibliothek verfügbar
The approved original version of this thesis is available in print at TU Wien Bibliothek.
TU WIEN Bibliothek Your knowledge hub

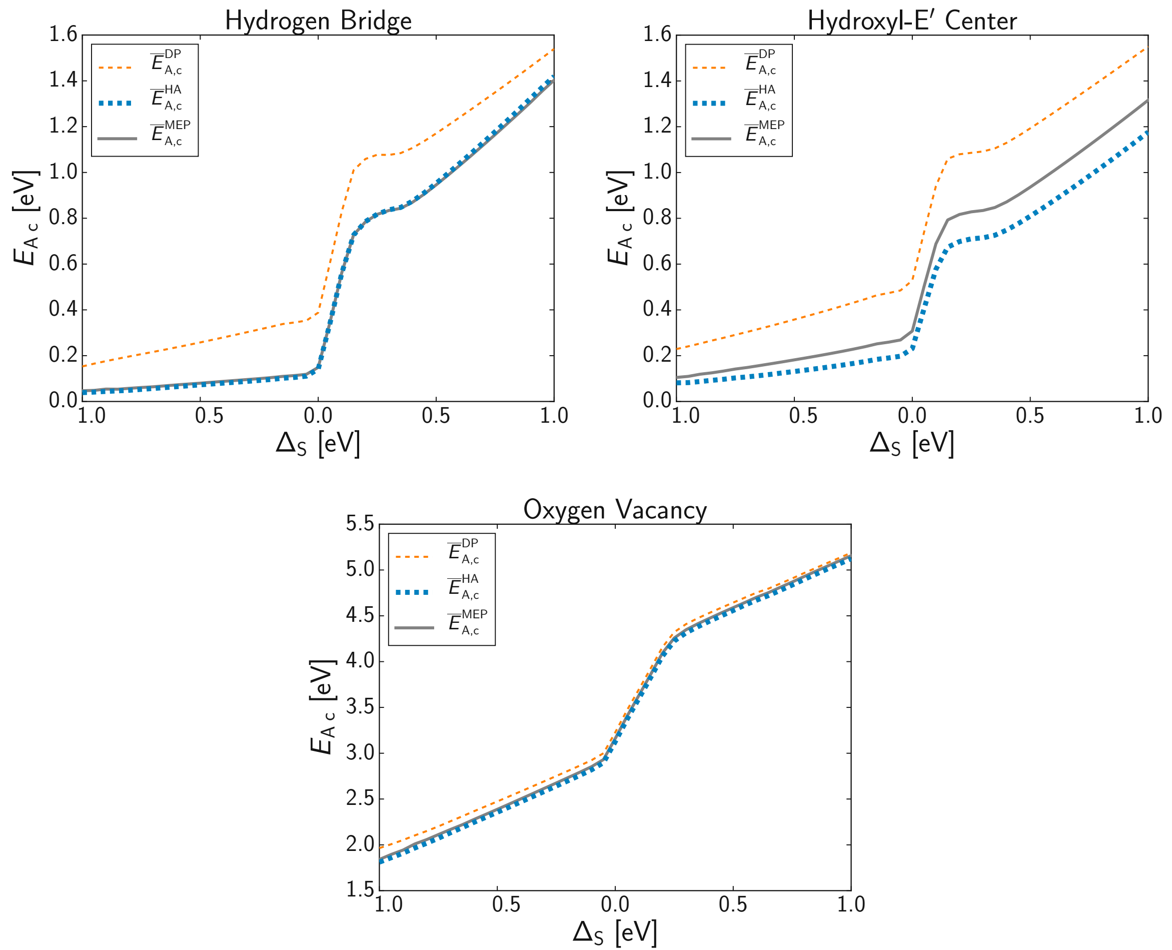

Figure 7.8: Dependence of the average capture activation energy $\overline{E}_{A,c}$ on the bias Δ_S for the different PES approximations. The harmonic approximation again provides much better results, especially for the HB defects. Contrary to the OV, the activation energies of the hydrogen related defects lie within the experimentally observed range of 0.6 to 1.4eV.

Die approbierte gedruckte Originalversion dieser Diplomarbeit ist an der TU Wien Bibliothek verfügbar
The approved original version of this thesis is available in print at TU Wien Bibliothek.
TU WIEN Bibliothek Your knowledge hub

the PES approximations. This is not surprising since the activation energies are simply derived from the theoretical capture times. However, the resulting theoretical activation energies can be compared to experimental values in order to identify defect types possibly responsible for BTI. Fig. 7.8 depicts the average activation energies $E_{A,c}(\Delta_S)$ as a function of the applied bias Δ_S. As can be seen, the harmonic approximation yields nearly the same results as the MEP for the HB and OV defects. In the case of the H-E′ center, the HA underestimates the activation energies. However, throughout the entire tested range $\Delta_S = -1.0$ to 1.0 eV, the harmonic approximation clearly performs much better than the direct path sampling. Note that the calculated average activation energies for the HB and H-E′ defects lie well within the experimental range of 0.6 to 1.4 eV (see Sec. 2.3) for a wide range of applied biases, making them likely candidates for causing BTI degradation. On the contrary, the activation energies for the OV defects are far too high to contribute to BTI at typical operating conditions.

7.2.4 Geometric Considerations

So far, the different PES approximations were compared without considering the total displacement of the atoms when switching the charge state. Here, the impact of the geometric distance between the neutral and positive minimum positions of the defect on the approximation error is briefly discussed. The geometric distance is simply defined by

$$d \triangleq \|\boldsymbol{R}_{0,\mathrm{eq}} - \boldsymbol{R}_{+,\mathrm{eq}}\|_2 \tag{7.3}$$

Like all other defect parameters, this distance also varies considerably within the same defect species due to the amorphous host material. Fig. 7.9 depicts the capture barriers $E_{B,c}$ of the HA and DP approximation (top) and the absolute approximation errors (bottom) as a function of the total displacement d. It is reasonable to expect an increase of the approximation error with larger d. This can be observed for the DP approximation, which shows a strong positive correlation with d for the HB and H-E′ defects. Surprisingly, the harmonic approximation does not show this tendency. Instead, the approximation error of the HA is statistically almost constant across the observed displacements. In the case of the OV, the three applied PES approximations give essentially the same results, as already seen in the previous section. Beside being near the WC regime, the OV also tends to have much smaller displacements between the minima than the hydrogen related defects, which naturally leads to smaller approximation errors.

7.3 Conclusions

Prior to the investigations presented in this work, the harmonic approximation was often used to model defect PESs within NMP transition theory. This approximation is very convenient since it allows simple analytical expressions for the resulting transition rates. Furthermore, for a given defect it can be constructed by only four DFT calculations and is therefore computationally rather cheap. It was originally assumed, that this simple

Die approbierte gedruckte Originalversion dieser Diplomarbeit ist an der TU Wien Bibliothek verfügbar
The approved original version of this thesis is available in print at TU Wien Bibliothek.
TU WIEN Bibliothek Your knowledge hub

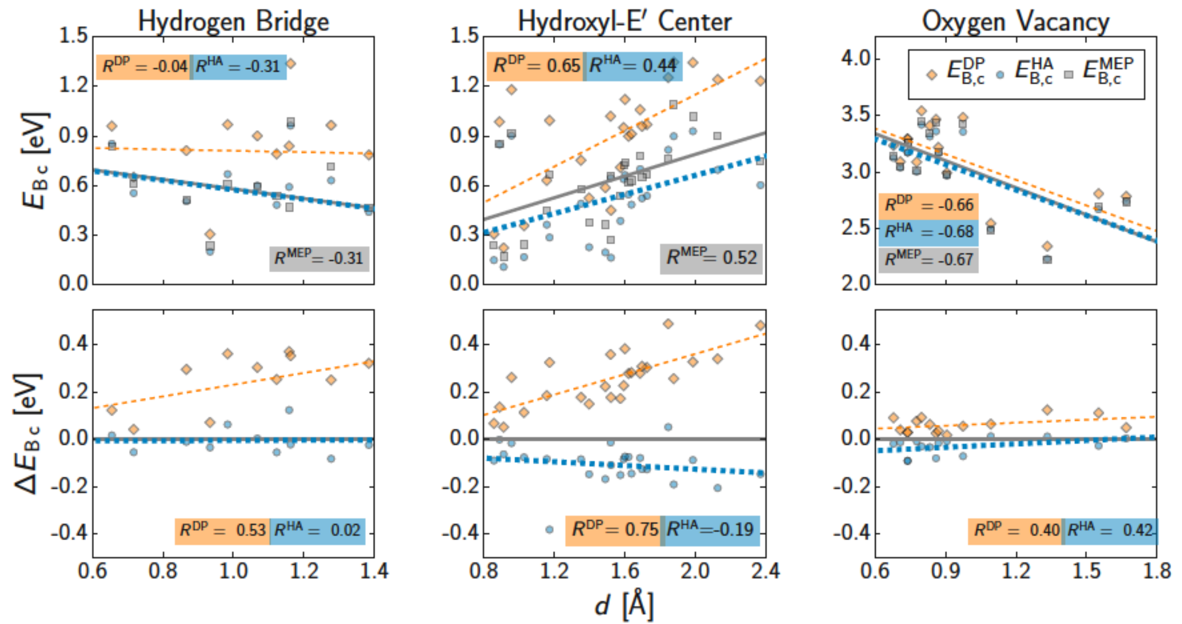

Figure 7.9: Capture barriers (**top**) and absolute approximation errors (**bottom**) as a function of the geometric distance d between the neutral and positive minimum positions for all three studied defect types at a shift $\Delta_S = 0.0$eV. The lines indicate linear least-square fits to the data points. Additionally, the respective correlation coefficients R are given. There is a strong positive correlation between the distance d and the error made with the DP approximation for the hydrogen-related defects. Surprisingly, the harmonic approximation seems to be nearly immune to variations in the displacement and consistently produces good results. Again, for the OV the difference between the approximation schemes is rather marginal. [143]

Die approbierte gedruckte Originalversion dieser Diplomarbeit ist an der TU Wien Bibliothek verfügbar
The approved original version of this thesis is available in print at TU Wien Bibliothek.
TU WIEN Bibliothek Your knowledge hub

approximation scheme is not very accurate due to the limited connection to the physical defect PESs. For that reason, the direct path sampling method was introduces in previous works as an attempt to get more accurate PESs by sampling multiple points along the direct reaction path. However, the study conducted in this work clearly shows that the HA generally is in much better agreement with the results of the novel MEP method than the DP approximation. It was demonstrated, that the DP approximation leads to significant overestimations of the transition barriers. Also the HA reproduces the τ-slope far better than the DP approximation. All the above findings indicate, that the harmonic approximation is in fact much more accurate than the direct path method. This justifies the wide use of this approximation for reliability calculations in device simulators and for the modelling of defects in general.

Of course, these findings only validate the use of the harmonic approximation for the studied defect types in SiO_2. However, the implemented MEP search routine can be used to reliably evaluate other approximation schemes for different material systems as well. Although the MEP method is considered to be the most accurate PES approximation, it can not be implemented in device simulators due to its high computational demands. Therefore it is not a replacement for traditional approximation schemes. However, it very well can provide a reference to evaluate the errors of simpler analytical PES approximations.

Die approbierte gedruckte Originalversion dieser Diplomarbeit ist an der TU Wien Bibliothek verfügbar
The approved original version of this thesis is available in print at TU Wien Bibliothek.
TU WIEN Bibliothek Your knowledge hub

CHAPTER 8 Summary and Outlook

Predicting BTI degradation in MOSFET devices requires simple analytical approximations for the involved defect PESs, which can be employed in device simulators. In this work an efficient method was implemented to test the quality of different PES approximation schemes. Within this approach the minimum energy path between differently charged defect states is calculated with a constraint optimization algorithm coupled to density functional theory. The minimum energy path (MEP) provides a reliable estimate of the reaction barriers of charge transitions to/from the defect. With this MEP approach, the accuracy of the widely used harmonic approximation and the recently proposed direct path sampling were tested for three different defect types, namely the hydrogen bridge, the hydroxyl-E′, and the oxygen vacancy, in amorphous SiO_2. It was demonstrated, that in general the harmonic approximation is in very good agreement with the MEP results, whereas the direct path sampling leads to significantly higher barriers and transition time constants.

Within the used models, the applied electric field in the oxide layer is assumed to only shift the energy levels of the defects relative to each other, resulting in bias dependent capture and emission times as observed in experiments. However, it should be investigated in future works, if the defects also interact with the oxide field through dipol moments, which would alter the shapes of the defect PESs and would consequently lead to an additional change in transition times.

In this work, defects were studied for ordinary MOSFETs with a SiO_2 oxide layer and a Si channel. However, the implemented algorithms can also be used to predict the defect behaviors for different gate dielectrics like SiON or HfO_2. Hence the MEP method presented in this work can help to enhance theoretical defect models in novel material combinations for MOSFETs in future investigations.

Die approbierte gedruckte Originalversion dieser Diplomarbeit ist an der TU Wien Bibliothek verfügbar
The approved original version of this thesis is available in print at TU Wien Bibliothek.
TU WIEN Bibliothek Your knowledge hub

Die approbierte gedruckte Originalversion dieser Diplomarbeit ist an der TU Wien Bibliothek verfügbar
The approved original version of this thesis is available in print at TU Wien Bibliothek.
TU WIEN Bibliothek Your knowledge hub

Bibliography

[1] K. S. Ralls, W. J. Skocpol, L. D. Jackel, R. E. Howard, L. A. Fetter, R. W. Epworth, and D. M. Tennant, "Discrete Resistance Switching in Submicrometer Silicon Inversion Layers: Individual interface traps and low-frequency (1/f?) noise," *Phys. Rev. Lett.*, vol. 52, pp. 228–231, Jan 1984.

[2] J. P. Campbell, L. C. Yu, K. P. Cheung, J. Qin, J. S. Suehle, A. Oates, and K. Sheng, "Large random telegraph noise in sub-threshold operation of nano-scale nMOSFETs," in *2009 IEEE International Conference on IC Design and Technology*, pp. 17–20, May 2009.

[3] T. Grasser, *Hot carrier degradation in semiconductor devices.* Cham: Springer, 2014.

[4] T. Grasser, *Bias temperature instability for devices and circuits.* New York: Springer, 2014.

[5] J. Franco, B. Kaczer, M. Toledano-Luque, P. J. Roussel, J. Mitard, L. . Ragnarsson, L. Witters, T. Chiarella, M. Togo, N. Horiguchi, G. Groeseneken, M. F. Bukhori, T. Grasser, and A. Asenov, "Impact of single charged gate oxide defects on the performance and scaling of nanoscaled FETs," in *2012 IEEE International Reliability Physics Symposium (IRPS)*, pp. 5A.4.1–5A.4.6, April 2012.

[6] W. Goes, *Hole Trapping and the Negative Bias Temperature Instability.* Ph.D Thesis, TU Wien, 2011.

[7] F. Schanovsky, *Atomistic Modeling in the Context of the Bias Temperature Instability.* Ph.D Thesis, TU Wien, 2013.

[8] Y. Wimmer, *Hydrogen Related Defects in Amorphous SiO_2 and the Negative Bias Temperature Instability.* Ph.D Thesis, TU Wien, 2017.

[9] A.-M. El-Sayed, M. B. Watkins, T. Grasser, V. V. Afanas'ev, and A. L. Shluger, "Hydrogen-induced rupture of strained SiO bonds in amorphous silicon dioxide," *Phys. Rev. Lett.*, vol. 114, p. 115503, Mar 2015.

[10] T. Grasser, K. Rott, H. Reisinger, M. Waltl, J. Franco, and B. Kaczer, "A unified perspective of RTN and BTI," in *2014 IEEE International Reliability Physics Symposium*, pp. 4A.5.1–4A.5.7, June 2014.

Die approbierte gedruckte Originalversion dieser Diplomarbeit ist an der TU Wien Bibliothek verfügbar
The approved original version of this thesis is available in print at TU Wien Bibliothek.
TU WIEN Bibliothek Your knowledge hub

[11] T. Grasser, "Stochastic charge trapping in oxides: From random telegraph noise to bias temperature instabilities," *Microelectronics Reliability*, vol. 52, no. 1, pp. 39 – 70, 2012. 2011 Reliability of Compound Semiconductors (ROCS) Workshop.

[12] C. H. Henry and D. V. Lang, "Nonradiative capture and recombination by multiphonon emission in GaAs and GaP," *Phys. Rev. B*, vol. 15, pp. 989–1016, Jan 1977.

[13] A. Nitzan, *Chemical dynamics in condensed phases : relaxation, transfer and reactions in condensed molecular systems*. Oxford New York: Oxford University Press, 2006.

[14] V. May, *Charge and energy transfer dynamics in molecular systems*. Weinheim Chichester: Wiley-VCH John Wiley distributor, 2011.

[15] K. L. Yip and W. B. Fowler, "Electronic structure of ${E_1}'$ centers in SiO_2," *Phys. Rev. B*, vol. 11, pp. 2327–2338, Mar 1975.

[16] E. P. O'Reilly and J. Robertson, "Theory of defects in vitreous silicon dioxide," *Phys. Rev. B*, vol. 27, pp. 3780–3795, Mar 1983.

[17] J. K. Rudra, W. B. Fowler, and F. J. Feigl, "Model for the E_2' center in alpha quartz," *Phys. Rev. Lett.*, vol. 55, pp. 2614–2617, Dec 1985.

[18] P. E. Bunson, M. D. Ventra, S. T. Pantelides, D. M. Fleetwood, and R. D. Schrimpf, "Hydrogen-related defects in irradiated SiO_2," *IEEE Transactions on Nuclear Science*, vol. 47, pp. 2289–2296, Dec 2000.

[19] P. E. Blöchl, "First-principles calculations of defects in oxygen-deficient silica exposed to hydrogen," *Phys. Rev. B*, vol. 62, pp. 6158–6179, Sep 2000.

[20] Y. Wimmer, A.-M. El-Sayed, W. Gös, T. Grasser, and A. L. Shluger, "Role of hydrogen in volatile behaviour of defects in SiO_2-based electronic devices," *Proceedings of the Royal Society of London A: Mathematical, Physical and Engineering Sciences*, vol. 472, no. 2190, 2016.

[21] F. Schanovsky, O. Baumgartner, W. Goes, and T. Grasser, "A detailed evaluation of model defects as candidates for the bias temperature instability," in *2013 International Conference on Simulation of Semiconductor Processes and Devices (SISPAD)*, pp. 1–4, Sept 2013.

[22] T. Grasser, W. Goes, Y. Wimmer, F. Schanovsky, G. Rzepa, M. Waltl, K. Rott, H. Reisinger, V. V. Afanas'ev, A. Stesmans, A. . El-Sayed, and A. L. Shluger, "On the microscopic structure of hole traps in pMOSFETs," in *2014 IEEE International Electron Devices Meeting*, pp. 21.1.1–21.1.4, Dec 2014.

[23] Y. Miura and Y. Matukura, "Investigation of silicon-silicon dioxide interface using MOS structure," *Japanese Journal of Applied Physics*, vol. 5, no. 2, p. 180, 1966.

Die approbierte gedruckte Originalversion dieser Diplomarbeit ist an der TU Wien Bibliothek verfügbar
The approved original version of this thesis is available in print at TU Wien Bibliothek.
TU WIEN Bibliothek Your knowledge hub

[24] C. Hu, "Gate oxide scaling limits and projection," in *International Electron Devices Meeting. Technical Digest*, pp. 319–322, Dec 1996.

[25] E. S. Machlin, *Materials science in microelectronics II*. Amsterdam Boston: Elsevier, 2006.

[26] D. K. Schroder, "Negative bias temperature instability: What do we understand?," *Microelectronics Reliability*, vol. 47, no. 6, pp. 841 – 852, 2007.

[27] M. Chudzik, B. Doris, R. Mo, J. Sleight, E. Cartier, C. Dewan, D. Park, H. Bu, W. Natzle, W. Yan, C. Ouyang, K. Henson, D. Boyd, S. Callegari, R. Carter, D. Casarotto, M. Gribelyuk, M. Hargrove, W. He, Y. Kim, B. Linder, N. Moumen, V. K. Paruchuri, J. Stathis, M. Steen, A. Vayshenker, X. Wang, S. Zafar, T. Ando, R. Iijima, M. Takayanagi, V. Narayanan, R. Wise, Y. Zhang, R. Divakaruni, M. Khare, and T. C. Chen, "High-performance high-k metal gates for 45nm CMOS and beyond with gate-first processing," in *2007 IEEE Symposium on VLSI Technology*, pp. 194–195, June 2007.

[28] G. Chen, M. F. Li, C. H. Ang, J. Z. Zheng, and D. L. Kwong, "Dynamic NBTI of p-MOS transistors and its impact on MOSFET scaling," in *Proc. Intl.Rel.Phys.Symp. (IRPS)*, pp. 196–203, 2003.

[29] L. Jin, M. Xu, and C. Tan, "An investigation on the permanent component of NBTI degradation in a 90nm CMOS technology," in *2006 8th International Conference on Solid-State and Integrated Circuit Technology Proceedings*, pp. 1147–1149, Oct 2006.

[30] V. Huard, "Two independent components modeling for negative bias temperature instability," in *2010 IEEE International Reliability Physics Symposium*, pp. 33–42, May 2010.

[31] A. A. Katsetos, "Negative bias temperature instability (NBTI) recovery with bake," *Microelectronics Reliability*, vol. 48, no. 10, pp. 1655 – 1659, 2008.

[32] T. Grasser, T. Aichinger, G. Pobegen, H. Reisinger, P.-J. Wagner, J. Franco, M. Nelhiebel, and B. Kaczer, "The permanent component of NBTI: Composition and annealing," in *Proc. Intl.Rel.Phys.Symp. (IRPS)*, pp. 6A.2.1 – 6A.2.9, 05 2011.

[33] T. Grasser, H. Reisinger, P. J. Wagner, F. Schanovsky, W. Goes, and B. Kaczer, "The time dependent defect spectroscopy (TDDS) for the characterization of the bias temperature instability," in *2010 IEEE International Reliability Physics Symposium*, pp. 16–25, May 2010.

[34] G. Rzepa, *Microscopic Modeling of NBTI in MOS Transistors*. Master Thesis, TU Wien, 2013.

TU WIEN Bibliothek Your knowledge hub
Die approbierte gedruckte Originalversion dieser Diplomarbeit ist an der TU Wien Bibliothek verfügbar
The approved original version of this thesis is available in print at TU Wien Bibliothek.

[35] B. Kaczer, V. Arkhipov, R. Degraeve, N. Collaert, G. Groeseneken, and M. Goodwin, “Disorder-controlled-kinetics model for negative bias temperature instability and its experimental verification,” in *2005 IEEE International Reliability Physics Symposium, 2005. Proceedings. 43rd Annual.*, pp. 381–387, April 2005.

[36] H. Reisinger, O. Blank, W. Heinrigs, A. Muhlhoff, W. Gustin, and C. Schlunder, “Analysis of NBTI degradation- and recovery-behavior based on ultra fast VT-measurements,” in *2006 IEEE International Reliability Physics Symposium Proceedings*, pp. 448–453, March 2006.

[37] T. Grasser, P. J. Wagner, P. Hehenberger, W. Gos, and B. Kaczer, “A rigorous study of measurement techniques for negative bias temperature instability,” in *2007 IEEE International Integrated Reliability Workshop Final Report*, pp. 6–11, Oct 2007.

[38] M. Denais, C. Parthasarathy, G. Ribes, Y. Rey-Tauriac, N. Revil, A. Bravaix, V. Huard, and F. Perrier, “On-the-fly characterization of NBTI in ultra-thin gate oxide pMOSFET’s,” in *IEDM Technical Digest. IEEE International Electron Devices Meeting, 2004.*, pp. 109–112, Dec 2004.

[39] Y. Yuzhelevski, M. Yuzhelevski, and G. Jung, “Random telegraph noise analysis in time domain,” *Review of Scientific Instruments*, vol. 71, no. 4, pp. 1681–1688, 2000.

[40] L. R. Rabiner, “A tutorial on hidden markov models and selected applications in speech recognition,” *Proceedings of the IEEE*, vol. 77, pp. 257–286, Feb 1989.

[41] H. Miki, N. Tega, M. Yamaoka, D. J. Frank, A. Bansal, M. Kobayashi, K. Cheng, C. P. D’Emic, Z. Ren, S. Wu, J. B. Yau, Y. Zhu, M. A. Guillorn, D. G. Park, W. Haensch, E. Leobandung, and K. Torii, “Statistical measurement of random telegraph noise and its impact in scaled-down high-k metal-gate MOSFETs,” in *2012 International Electron Devices Meeting*, pp. 19.1.1–19.1.4, Dec 2012.

[42] T. Grasser, H. Reisinger, P.-J. Wagner, and B. Kaczer, “Time-dependent defect spectroscopy for characterization of border traps in metal-oxide-semiconductor transistors,” *Phys. Rev. B*, vol. 82, p. 245318, Dec 2010.

[43] M. Kirton and M. Uren, “Noise in solid-state microstructures: A new perspective on individual defects, interface states and low-frequency (1/f) noise,” *Advances in Physics*, vol. 38, no. 4, pp. 367–468, 1989.

[44] T. Grasser, P. . Wagner, H. Reisinger, T. Aichinger, G. Pobegen, M. Nelhiebel, and B. Kaczer, “Analytic modeling of the bias temperature instability using capture/emission time maps,” in *2011 International Electron Devices Meeting*, pp. 27.4.1–27.4.4, Dec 2011.

Die approbierte gedruckte Originalversion dieser Diplomarbeit ist an der TU Wien Bibliothek verfügbar
The approved original version of this thesis is available in print at TU Wien Bibliothek.
TU WIEN Bibliothek Your knowledge hub

[45] K. O. Jeppson and C. M. Svensson, "Negative bias stress of MOS devices at high electric fields and degradation of MNOS devices," *Journal of Applied Physics*, vol. 48, no. 5, pp. 2004–2014, 1977.

[46] M. Houssa, M. Aoulaiche, S. De Gendt, G. Groeseneken, M. M. Heyns, and A. Stesmans, "Reaction-dispersive proton transport model for negative bias temperature instabilities," *Applied Physics Letters*, vol. 86, no. 9, p. 093506, 2005.

[47] T. Tewksbury, *Relaxation effects in MOS devices due to tunnel exchange with near-interface oxide traps.* Ph.D Thesis, Massachusetts Institute of Technology, 1992.

[48] I. Lundström and C. Svensson, "Tunneling to traps in insulators," *Journal of Applied Physics*, vol. 43, no. 12, pp. 5045–5047, 1972.

[49] F. P. Heiman and G. Warfield, "The effects of oxide traps on the MOS capacitance," *IEEE Transactions on Electron Devices*, vol. 12, pp. 167–178, April 1965.

[50] V. Huard, C. Parthasarathy, N. Rallet, C. Guerin, M. Mammase, D. Barge, and C. Ouvrard, "New characterization and modeling approach for NBTI degradation from transistor to product level," in *2007 IEEE International Electron Devices Meeting*, pp. 797–800, Dec 2007.

[51] R. N. Hall, "Electron-hole recombination in germanium," *Phys. Rev.*, vol. 87, pp. 387–387, Jul 1952.

[52] W. Shockley and W. T. Read, "Statistics of the recombinations of holes and electrons," *Phys. Rev.*, vol. 87, pp. 835–842, Sep 1952.

[53] A. McWorther, *1/f noise and related surface effects in germanium.* Sc.D Thesis, Massachusetts Institute of Technology, 1955.

[54] F. Schanovsky, O. Baumgartner, V. Sverdlov, and T. Grasser, "A multi scale modeling approach to non-radiative multi phonon transitions at oxide defects in MOS structures," *Journal of Computational Electronics*, vol. 11, pp. 218–224, Sep 2012.

[55] S. Guo, R. Wang, D. Mao, Y. Wang, and R. Huang, "Anomalous random telegraph noise in nanoscale transistors as direct evidence of two metastable states of oxide traps," *Scientific Reports*, vol. 7, 2017.

[56] D. Gillespie, *Markov processes : an introduction for physical scientists.* Boston: Academic Press, 1992.

[57] O. Ibe, *Markov processes for stochastic modeling.* London: Elsevier, 2013.

[58] J. Honerkamp, *Statistical physics : an advanced approach with applications.* Berlin New York: Springer, 2012.

Die approbierte gedruckte Originalversion dieser Diplomarbeit ist an der TU Wien Bibliothek verfügbar
The approved original version of this thesis is available in print at TU Wien Bibliothek.
TU WIEN Bibliothek Your knowledge hub

[59] V. I. Arnold, *Ordinary differential equations.* Berlin: New York Springer-Verlag, 1992.

[60] S. Arrhenius, "Über die Dissociationswärme und den Einfluss der Temperatur auf den Dissociationsgrad der Elektrolyte," *Zeitschrift für Physikalische Chemie*, vol. 4U(1), pp. 96–116, 1889.

[61] P. M. Lenahan, J. P. Campbell, A. T. Krishnan, and S. Krishnan, "A model for NBTI in nitrided oxide MOSFETs which does not involve hydrogen or diffusion," *IEEE Transactions on Device and Materials Reliability*, vol. 11, pp. 219–226, June 2011.

[62] T. Aichinger, S. Puchner, M. Nelhiebel, T. Grasser, and H. Hutter, "Impact of hydrogen on recoverable and permanent damage following negative bias temperature stress," in *2010 IEEE International Reliability Physics Symposium*, pp. 1063–1068, May 2010.

[63] T. Grasser, B. Kaczer, and W. Goes, "An energy-level perspective of bias temperature instability," in *2008 IEEE International Reliability Physics Symposium*, pp. 28–38, April 2008.

[64] A. T. Krishnan, S. Chakravarthi, P. Nicollian, V. Reddy, and S. Krishnan, "Negative bias temperature instability mechanism: The role of molecular hydrogen," *Applied Physics Letters*, vol. 88, no. 15, p. 153518, 2006.

[65] M. Alam and S. Mahapatra, "A comprehensive model of PMOS NBTI degradation," *Microelectronics Reliability*, vol. 45, no. 1, pp. 71 – 81, 2005.

[66] F. Schanovsky, W. Gös, and T. Grasser, "An advanced description of oxide traps in MOS transistors and its relation to DFT," *Journal of Computational Electronics*, vol. 9, pp. 135–140, Dec 2010.

[67] G. Czycholl, *Theoretische Festkorperphysik Band 1 Grundlagen: Phononen und Elektronen in Kristallen.* Berlin, Heidelberg: Springer Berlin Heidelberg, 2016.

[68] H. Shull and G. G. Hall, "Atomic units," *Nature*, vol. 184, pp. 1559–1560, Nov 1959.

[69] M. Born and R. Oppenheimer, "Zur Quantentheorie der Molekeln," *Annalen der Physik*, vol. 389, no. 20, pp. 457–484, 1927.

[70] M. Born and K. Huang, *Dynamical theory of crystal lattices.* Oxford New York: Oxford University Press, 1988.

[71] P. M. Morse, "Diatomic molecules according to the wave mechanics. II. vibrational levels," *Phys. Rev.*, vol. 34, pp. 57–64, Jul 1929.

Die approbierte gedruckte Originalversion dieser Diplomarbeit ist an der TU Wien Bibliothek verfügbar
The approved original version of this thesis is available in print at TU Wien Bibliothek.
TU WIEN Bibliothek Your knowledge hub

[72] S. Mohr, L. E. Ratcliff, L. Genovese, D. Caliste, P. Boulanger, S. Goedecker, and T. Deutsch, "Accurate and efficient linear scaling DFT calculations with universal applicability," *Phys. Chem. Chem. Phys.*, vol. 17, pp. 31360–31370, 2015.

[73] P. Hohenberg and W. Kohn, "Inhomogeneous electron gas," *Phys. Rev.*, vol. 136, pp. B864–B871, Nov 1964.

[74] P. W. Atkins, *Molecular quantum mechanics*. Oxford New York: Oxford University Press, 2011.

[75] W. Kohn and L. J. Sham, "Self-consistent equations including exchange and correlation effects," *Phys. Rev.*, vol. 140, pp. A1133–A1138.

[76] R. Weinstock, *Calculus of variations, with applications to physics and engineering*. New York: Dover Publications, 1974.

[77] R. Parr and W. Yang, *Density-Functional Theory of Atoms and Molecules*. Oxford: Oxford University Press, 2015.

[78] E. Engel and R. M. Dreizler, "Functionals and the functional derivative," in *Density Functional Theory. An Advanced Course*, ch. Appendices, pp. 403–531, Berlin Heidelberg: Springer, 2011.

[79] P. A. M. Dirac, "Note on exchange phenomena in the Thomas atom," *Mathematical Proceedings of the Cambridge Philosophical Society*, vol. 26, no. 3, p. 376385, 1930.

[80] D. M. Ceperley and B. J. Alder, "Ground state of the electron gas by a stochastic method," *Phys. Rev. Lett.*, vol. 45, pp. 566–569, Aug 1980.

[81] P. P. Rushton, *Towards a Non-Local Density Functional Description of Exchange and Correlation*. Ph.D Thesis, University of Durham, 2002.

[82] R. Dovesi, R. Orlando, C. Roetti, C. Pisani, and V. Saunders, "The periodic Hartree-Fock method and its implementation in the Crystal code," *physica status solidi (b)*, vol. 217, no. 1, pp. 63–88.

[83] D. C. Langreth and M. J. Mehl, "Beyond the local-density approximation in calculations of ground-state electronic properties," *Phys. Rev. B*, vol. 28, pp. 1809–1834, Aug 1983.

[84] A. D. Becke, "Density-Functional thermochemistry. I. The effect of the exchange-only gradient correction," *The Journal of Chemical Physics*, vol. 96, no. 3, pp. 2155–2160, 1992.

[85] J. P. Perdew, K. Burke, and M. Ernzerhof, "Generalized gradient approximation made simple," *Phys. Rev. Lett.*, vol. 77, pp. 3865–3868, Oct 1996.

Die approbierte gedruckte Originalversion dieser Diplomarbeit ist an der TU Wien Bibliothek verfügbar
The approved original version of this thesis is available in print at TU Wien Bibliothek.
TU WIEN Bibliothek Your knowledge hub

[86] J. P. Perdew, J. A. Chevary, S. H. Vosko, K. A. Jackson, M. R. Pederson, D. J. Singh, and C. Fiolhais, "Atoms, molecules, solids, and surfaces: Applications of the generalized gradient approximation for exchange and correlation," *Phys. Rev. B*, vol. 46, pp. 6671–6687, Sep 1992.

[87] F. Zahariev, S. S. Leang, and M. S. Gordon, "Functional derivatives of meta-generalized gradient approximation (meta-GGA) type exchange-correlation density functionals," *The Journal of Chemical Physics*, vol. 138, no. 24, p. 244108, 2013.

[88] J. P. Perdew and M. Levy, "Physical content of the exact Kohn-Sham orbital energies: Band gaps and derivative discontinuities," *Phys. Rev. Lett.*, vol. 51, pp. 1884–1887, Nov 1983.

[89] A. D. Becke, "A new mixing of Hartree-Fock and local density-functional theories," *The Journal of Chemical Physics*, vol. 98, no. 2, pp. 1372–1377, 1993.

[90] M. Guidon, J. Hutter, and J. VandeVondele, "Robust periodic Hartree-Fock exchange for large-scale simulations using gaussian basis sets," *Journal of Chemical Theory and Computation*, vol. 5, no. 11, pp. 3010–3021, 2009. PMID: 26609981.

[91] J. P. Perdew, M. Ernzerhof, and K. Burke, "Rationale for mixing exact exchange with density functional approximations," *The Journal of Chemical Physics*, vol. 105, no. 22, pp. 9982–9985, 1996.

[92] J. Heyd, G. E. Scuseria, and M. Ernzerhof, "Hybrid functionals based on a screened Coulomb potential," *The Journal of Chemical Physics*, vol. 118, no. 18, pp. 8207–8215, 2003.

[93] A. D. Becke, "Density Functional thermochemistry. III. The role of exact exchange," *The Journal of Chemical Physics*, vol. 98, no. 7, pp. 5648–5652, 1993.

[94] A. J. Garza and G. E. Scuseria, "Predicting band gaps with hybrid density functionals," vol. 7, 08 2016.

[95] F. Bloch, "Über die Quantenmechanik der Elektronen in Kristallgittern," *Zeitschrift für Physik*, vol. 52, pp. 555–600, Jul 1929.

[96] P. Schwerdtfeger, "The pseudopotential approximation in electronic structure theory," *ChemPhysChem*, vol. 12, no. 17, pp. 3143–3155, 2011.

[97] G. Lippert, J. Hutter, and M. Parrinello, "A hybrid gaussian and plane wave density functional scheme," *Molecular Physics*, vol. 92, no. 3, pp. 477–488, 1997.

[98] J. C. Slater, "Atomic shielding constants," *Phys. Rev.*, vol. 36, pp. 57–64, Jul 1930.

[99] R. C. Raffenetti, "General contraction of gaussian atomic orbitals: Core, valence, polarization, and diffuse basis sets; molecular integral evaluation," *The Journal of Chemical Physics*, vol. 58, no. 10, pp. 4452–4458, 1973.

Die approbierte gedruckte Originalversion dieser Diplomarbeit ist an der TU Wien Bibliothek verfügbar
The approved original version of this thesis is available in print at TU Wien Bibliothek.
TU WIEN Bibliothek Your knowledge hub

[100] J. Hutter, M. Iannuzzi, F. Schiffmann, and J. VandeVondele, "CP2K: atomistic simulations of condensed matter systems," *Wiley Interdisciplinary Reviews: Computational Molecular Science*, vol. 4, no. 1, pp. 15–25, 2013.

[101] G. Lippert, J. Hutter, and M. Parrinello, "The gaussian and augmented-plane-wave density functional method for ab initio molecular dynamics simulations," *Theoretical Chemistry Accounts*, vol. 103, pp. 124–140, Dec 1999.

[102] M. Guidon, J. Hutter, and J. VandeVondele, "Auxiliary density matrix methods for Hartree-Fock exchange calculations," *Journal of Chemical Theory and Computation*, vol. 6, no. 8, pp. 2348–2364, 2010. PMID: 26613491.

[103] P. Ordejón, E. Artacho, and J. M. Soler, "Self-consistent order-n density-functional calculations for very large systems," *Phys. Rev. B*, vol. 53, pp. R10441–R10444, Apr 1996.

[104] X. Chen, J.-M. Langlois, and W. A. Goddard, "Dual-space approach for density-functional calculations of two- and three-dimensional crystals using gaussian basis functions," *Phys. Rev. B*, vol. 52, pp. 2348–2361, Jul 1995.

[105] J. VandeVondele, M. Krack, F. Mohamed, M. Parrinello, T. Chassaing, and J. Hutter, "Quickstep: Fast and accurate density functional calculations using a mixed gaussian and plane waves approach," *Computer Physics Communications*, vol. 167, no. 2, pp. 103 – 128, 2005.

[106] J. VandeVondele and J. Hutter, "Gaussian basis sets for accurate calculations on molecular systems in gas and condensed phases," *The Journal of Chemical Physics*, vol. 127, no. 11, p. 114105, 2007.

[107] S. Goedecker, M. Teter, and J. Hutter, "Separable dual-space gaussian pseudopotentials," *Phys. Rev. B*, vol. 54, pp. 1703–1710, Jul 1996.

[108] A.-M. El-Sayed, M. B. Watkins, T. Grasser, V. V. Afanasev, and A. L. Shluger, "Hole trapping at hydrogenic defects in amorphous silicon dioxide," *Microelectronic Engineering*, vol. 147, pp. 141 – 144, 2015. Insulating Films on Semiconductors 2015.

[109] C. G. Broyden, "The convergence of a class of double-rank minimization algorithms 1. general considerations," *IMA Journal of Applied Mathematics*, vol. 6, no. 1, pp. 76–90, 1970.

[110] R. Fletcher, "A new approach to variable metric algorithms," *The Computer Journal*, vol. 13, no. 3, pp. 317–322, 1970.

[111] D. Goldfarb, "A family of variable-metric methods derived by variational means," *Mathematics of Computation*, vol. 24, no. 109, pp. 23–26, 1970.

Die approbierte gedruckte Originalversion dieser Diplomarbeit ist an der TU Wien Bibliothek verfügbar
The approved original version of this thesis is available in print at TU Wien Bibliothek.
TU WIEN Bibliothek Your knowledge hub

[112] D. F. Shanno, “Conditioning of quasi-newton methods for function minimization,” *Mathematics of Computation*, vol. 24, no. 111, pp. 647–656, 1970.

[113] A.-M. El-Sayed, *Atomistic Modelling of Charge Trapping Defects in Silicon Dioxide*. PhD thesis, University Collge London, 2015.

[114] A. C. T. van Duin, S. Dasgupta, F. Lorant, and W. A. Goddard, “ReaxFF: a reactive force field for hydrocarbons,” *The Journal of Physical Chemistry A*, vol. 105, no. 41, pp. 9396–9409, 2001.

[115] “Vienna scientific cluster.” http://vsc.ac.at/home/. Accessed: 2018-08-25.

[116] H. Eyring, “The activated complex in chemical reactions,” *The Journal of Chemical Physics*, vol. 3, no. 2, pp. 107–115, 1935.

[117] M. G. Evans and M. Polanyi, “Some applications of the transition state method to the calculation of reaction velocities, especially in solution,” *Trans. Faraday Soc.*, vol. 31, pp. 875–894, 1935.

[118] R. P. Bell, *The tunnel effect in chemistry*. London New York: Chapman and Hall, 1980.

[119] G. H. Vineyard, “Frequency factors and isotope effects in solid state rate processes,” *Journal of Physics and Chemistry of Solids*, vol. 3, no. 1, pp. 121 – 127, 1957.

[120] F. Roozeboom, *Advanced Gate Stack, Source/Drain, and Channel Engineering for Si-Based CMOS 2: New Materials, Processes and Equipment*. Electrochemical Society, 2006.

[121] K.-N. Tu and A. M. Gusak, *Kinetics in Nanoscale Materials*. Wiley, 2014.

[122] C. J. Cerjan and W. H. Miller, “On finding transition states,” *The Journal of Chemical Physics*, vol. 75, no. 6, pp. 2800–2806, 1981.

[123] D. T. Nguyen and D. A. Case, “On finding stationary states on large-molecule potential energy surfaces,” *The Journal of Physical Chemistry*, vol. 89, no. 19, pp. 4020–4026, 1985.

[124] H. Taylor and J. Simons, “Imposition of geometrical constraints on potential energy surface walking procedures,” *The Journal of Physical Chemistry*, vol. 89, no. 4, pp. 684–688, 1985.

[125] R. Elber and M. Karplus, “A method for determining reaction paths in large molecules: Application to myoglobin,” *Chemical Physics Letters*, vol. 139, no. 5, pp. 375 – 380, 1987.

Die approbierte gedruckte Originalversion dieser Diplomarbeit ist an der TU Wien Bibliothek verfügbar
The approved original version of this thesis is available in print at TU Wien Bibliothek.
TU WIEN Bibliothek Your knowledge hub

[126] H. Jónsson, G. Mills, and K. W. Jacobsen, "Nudged elastic band method for finding minimum energy paths of transitions," in *Classical and Quantum Dynamics in Condensed Phase Simulations*, pp. 385–404, World Scientific, 1998.

[127] G. Henkelman and H. Jónsson, "Improved tangent estimate in the nudged elastic band method for finding minimum energy paths and saddle points," *The Journal of Chemical Physics*, vol. 113, no. 22, pp. 9978–9985, 2000.

[128] G. Henkelman, B. P. Uberuaga, and H. Jónsson, "A climbing image nudged elastic band method for finding saddle points and minimum energy paths," *The Journal of Chemical Physics*, vol. 113, no. 22, pp. 9901–9904, 2000.

[129] K. Huang and A. Rhys, "Theory of light absorption and non-radiative transitions in F-centres," *Proceedings of the Royal Society of London A: Mathematical, Physical and Engineering Sciences*, vol. 204, no. 1078, pp. 406–423, 1950.

[130] P. A. M. Dirac, "The quantum theory of the emission and absorption of radiation," *Proceedings of the Royal Society of London A: Mathematical, Physical and Engineering Sciences*, vol. 114, no. 767, pp. 243–265, 1927.

[131] J. Orear, *Nuclear physics : a course given by Enrico Fermi at the University of Chicago*. Chicago: University of Chicago Press, 1974.

[132] J. Franck and E. G. Dymond, "Elementary processes of photochemical reactions," *Trans. Faraday Soc.*, vol. 21, pp. 536–542, 1926.

[133] E. Condon, "A theory of intensity distribution in band systems," *Phys. Rev.*, vol. 28, pp. 1182–1201, Dec 1926.

[134] M. Lax, "The Franck-Condon principle and its application to crystals," *The Journal of Chemical Physics*, vol. 20, no. 11, pp. 1752–1760, 1952.

[135] J. H. Zheng, H. S. Tan, and S. C. Ng, "Theory of non-radiative capture of carriers by multiphonon processes for deep centres in semiconductors," *Journal of Physics: Condensed Matter*, vol. 6, no. 9, p. 1695, 1994.

[136] W. Goes, Y. Wimmer, A.-M. El-Sayed, G. Rzepa, M. Jech, A. Shluger, and T. Grasser, "Identification of oxide defects in semiconductor devices: A systematic approach linking DFT to rate equations and experimental evidence," *Microelectronics Reliability*, vol. 87, pp. 286 – 320, 2018.

[137] B. Stampfer, *Trap Assisted Tunneling and Band Interaction using the Non-Radiative Multi Phonon Model*. Master Thesis, TU Wien, 2016.

[138] J. F. Conley, P. M. Lenahan, and W. F. McArthur, "Preliminary investigation of the kinetics of postoxidation rapid thermal anneal induced hole-trap-precursor formation in microelectronic SiO_2 films," *Applied Physics Letters*, vol. 73, no. 15, pp. 2188–2190, 1998.

Die approbierte gedruckte Originalversion dieser Diplomarbeit ist an der TU Wien Bibliothek verfügbar
The approved original version of this thesis is available in print at TU Wien Bibliothek.
TU WIEN Bibliothek Your knowledge hub

[139] T. Knobloch, *Characterization and Physical Modeling of Degradation in* MoS_2 *Transistors*. Master Thesis, TU Wien, 2016.

[140] W. Goes, M. Toledano-Luque, O. Baumgartner, M. Bina, F. Schanovsky, B. Kaczer, and T. Grasser, "Understanding correlated drain and gate current fluctuations," in *Proceedings of the 20th IEEE International Symposium on the Physical and Failure Analysis of Integrated Circuits (IPFA)*, pp. 51–56, July 2013.

[141] W. B. Fowler, J. K. Rudra, M. E. Zvanut, and F. J. Feigl, "Hysteresis and Franck-Condon relaxation in insulator-semiconductor tunneling," *Phys. Rev. B*, vol. 41, pp. 8313–8317, Apr 1990.

[142] H.-P. Komsa, T. T. Rantala, and A. Pasquarello, "Finite-size supercell correction schemes for charged defect calculations," *Phys. Rev. B*, vol. 86, p. 045112, Jul 2012.

[143] Y. Wimmer, D. Waldhoer, W. Goes, A.-M. El-Sayed, A. L. Shluger, and T. Grasser, "On the impact of potential energy surface approximations on nonradiative multiphonon charge transitions," *Physical Review B (manuscript in preparation)*, 2018.

[144] Y. Wimmer, W. Goes, A.-M. El-Sayed, A. L. Shluger, and T. Grasser, "On the validity of the harmonic potential energy surface approximation for nonradiative multiphonon charge transitions in oxide defects," in *Book of Abstracts 18th International Workshop on Computational Electronics (IWCE)*, 2015.

[145] T. Chachiyo and J. H. Rodriguez, "A direct method for locating minimum-energy crossing points (MECPs) in spin-forbidden transitions and nonadiabatic reactions," *The Journal of Chemical Physics*, vol. 123, no. 9, p. 094711, 2005.

[146] K. Schittkowski, C. Zillober, and R. Zotemantel, "Numerical comparison of nonlinear programming algorithms for structural optimization," *Structural optimization*, vol. 7, pp. 1–19, Feb 1994.

[147] R. Wilson, *A Simplicial Algorithm for Concave Programming*. Ph.D Thesis, Harvard University, 1963.

[148] M. J. D. Powell, "On the convergence of the variable metric algorithm," *IMA Journal of Applied Mathematics*, vol. 7, no. 1, pp. 21–36, 1971.

[149] D. Kraft, *A software package for sequential quadratic programming*. Report, DLR German Aerospace Center Institute for Flight Mechanics, Köln, Germany, 1988.

[150] T. E. Oliphant, "Python for scientific computing," *Computing in Science Engineering*, vol. 9, pp. 10–20, May 2007.

[151] K. J. Millman and M. Aivazis, "Python for scientists and engineers," *Computing in Science Engineering*, vol. 13, pp. 9–12, March 2011.

Die approbierte gedruckte Originalversion dieser Diplomarbeit ist an der TU Wien Bibliothek verfügbar
The approved original version of this thesis is available in print at TU Wien Bibliothek.
TU WIEN Bibliothek Your knowledge hub

[152] E. Jones, T. Oliphant, P. Peterson, *et al.*, “SciPy: Open source scientific tools for Python,” 2001–. [Online; accessed September 20 , 2018, v1.0.0].

[153] A. Grill, B. Stampfer, M. Waltl, K. Im, J. . Lee, C. Ostermaier, H. Ceric, and T. Grasser, “Characterization and modeling of single defects in GaN/AlGaN FIN-MIS-HEMTs,” in *2017 IEEE International Reliability Physics Symposium (IRPS)*, pp. 3B–5.1–3B–5.5, April 2017.

Die approbierte gedruckte Originalversion dieser Diplomarbeit ist an der TU Wien Bibliothek verfügbar
The approved original version of this thesis is available in print at TU Wien Bibliothek.
TU WIEN Bibliothek Your knowledge hub

Die approbierte gedruckte Originalversion dieser Diplomarbeit ist an der TU Wien Bibliothek verfügbar
The approved original version of this thesis is available in print at TU Wien Bibliothek.
TU WIEN Bibliothek Your knowledge hub

Hiermit erkläre ich, dass die vorliegende Arbeit gemäß dem Code of Conduct - Regeln zur Sicherung guter wissenschaftlicher Praxis (in der aktuellen Fassung des jeweiligen Mitteilungsblattes der TU Wien), insbesondere ohne unzulässige Hilfe Dritter und ohne Benutzung anderer als der angegebenen Hilfsmittel, angefertigt wurde. Die aus anderen Quellen direkt oder indirekt übernommenen Daten und Konzepte sind unter Angabe der Quelle gekennzeichnet.

Die Arbeit wurde bisher weder im In- noch im Ausland in gleicher oder in ähnlicher Form in anderen Prüfungsverfahren vorgelegt.

Wien, Oktober 2018

Dominic Waldhör

Die approbierte gedruckte Originalversion dieser Diplomarbeit ist an der TU Wien Bibliothek verfügbar
The approved original version of this thesis is available in print at TU Wien Bibliothek.
TU WIEN Bibliothek Your knowledge hub